The Dissertation Committee for Jingang Li Certifies that this is the approved version of the following Dissertation:

Optothermal Approaches to Architected Functional Nanomaterials and Nanostructures

Committee:

Yuebing Zheng, Supervisor

Deji Akinwande

Donglei (Emma) Fan

Brian A. Korgel

Optothermal Approaches to Architected Functional Nanomaterials and Nanostructures

by

Jingang Li

Dissertation

Presented to the Faculty of the Graduate School of

The University of Texas at Austin

in Partial Fulfillment

of the Requirements

for the Degree of

Doctor of Philosophy

The University of Texas at Austin

December 2021

Dedication

To my parents and life mentors.

Acknowledgments

I would like first to thank my supervisor, Prof. Yuebing Zheng, for his relentless support, guidance, encouragement, and mentorship during my doctoral study. I truly appreciate him for providing an open and creative research environment. In addition, he often motivated me to aim high and be ambitious to solve the biggest challenge in the field. I always benefit from his invaluable instructions in research and am inspired by his superior leadership in the independent career.

I would like to thank Prof. Deji Akinwande, Prof. Donglei (Emma) Fan, and Prof. Brian A. Korgel for serving in my committee and providing invaluable collaboration to my research projects. I greatly appreciated their insightful suggestions and helpful discussions. I would also like to thank other collaborators, Prof. Andrea Alù, Prof. Yuanyue Liu, Prof. Michael F. Becker, Dr. Eric H. Hill, and Prof. Zhenglong Zhang, for their tremendous support to my research.

I would like to thank the senior members from Zheng group, Dr. Linhan Lin, Dr. Mingsong Wang, and Dr. Xiaolei Peng, for their guidance on our collaborating projects. I would like to thank Pavana Siddhartha Kollipara, Dr. Yaoran Liu, Dr. Wei Li, Dr. Zilong Wu, Dr. Kan Yao, Dr. Bharath Bangalore Rajeeva, Zhihan Chen, Hongru Ding, Jie Fang, Dr. Taizhi Jiang, Dr. Jianhe Guo, etc., for their support to my research projects. I would also like to thank other collaborators, Dr. Guangwei Hu, Dr. Huanan Li, Yichao Feng, etc., for their contributions to this dissertation. It has been enjoyable to work with them.

I would also like to thank all the professors, teachers, and friends in my undergraduate for supporting my Ph.D. application years ago. In the end, I would like to thank my family for their unconditional support and love. Without them, none of this would be possible.

Abstract

Optothermal Approaches to Architected Functional Nanomaterials and Nanostructures

Jingang Li, PhD

The University of Texas at Austin, 2021

Supervisor: Yuebing Zheng

The manipulation and engineering of nanomaterials are the core techniques in modern nanotechnology and have been extensively investigated over the past decades. Many optical techniques were developed to manipulate, assemble, and pattern nanomaterials, which have inspired numerous progress in various fields, such as microrobotics, bottom-up nanofabrication, nanomedicine, and microelectronics. With the entropically favorable photon-to-phonon conversion and tailorable opto-thermo-matter coupling, various thermal forces in the light-controlled temperature field can be harnessed to achieve the precise control of nanomaterials at a high spatial and temporal resolution.

This Dissertation focuses on optothermal approaches for optical manipulation and structuring of functional nanomaterials and nanostructures on solid substrates for the development of on-chip devices. First, thermophoresis of colloidal species is exploited to optically trap various nanoparticles and biological objects. The assembly and printing of colloidal matter on the substrate from the suspension are demonstrated with the assistance of optothermally controlled depletion forces. Next, by optothermally modulating the nanomaterial-substrate interactions, versatile manipulation and assembly of nanomaterials

on solid substrates can be achieved. Precise manipulation of nanomaterials, orbital rotation of nanomotors, and reconfigurable assembly of functional nanostructures on the solid substrate are demonstrated. Last, opto-thermoplasmonic nanolithography is developed for on-demand patterning of a variety of two-dimensional materials through plasmon-enhanced thermal oxidation and sublimation. It is anticipated that the studies presented here provide an ideal platform for studying colloidal science, materials science, and nanophotonics, and the optothermally architected nanomaterials and nanostructures are expected to stimulate more advances in a broad range of fields.

Table of Contents

List of Tables

List of Figures

Chapter 1: Introduction*

1.1 Introduction to nanofabrication techniques

Nanofabrication is the core technique in modern nanotechnology to effectively manufacture various functional devices with a wide range of applications. For example, large-scale, commercial implementation of micro- and nano-lithography techniques has resulted in continual miniaturization of integrated microelectronic chips for data processing and storage. Besides information technology, nanofabrication has also stimulated research in energy (solar cells, batteries, supercapacitors),[1-3] biology (biosensors and proteins patterning),[4, 5] and nanomedicine (drug delivery).[6] In addition, the ability to fabricate devices at the nanoscale has made possible revolutionary devices that rely on nanoscale physical principles (e.g., quantum size effects) such as quantum cascade lasers and single-electron transistors.[7, 8]

Currently, most nanofabrication processes are accomplished via photolithography, which involves the pattern transfer from a photomask to a resistive film by light exposure due to its simplicity and high throughput. However, its feature size is limited by the wavelength of light exposure due to the optical diffraction limit.[9] The development of extreme ultraviolet lithography and X-ray lithography can realize a small feature size down to sub-30 nm. Nevertheless, reliable mask fabrication and light sources for such short wavelength lithography remain challenging.[10] Various techniques were developed to avoid the diffraction limit and achieve higher resolution. Electron beam lithography employs a

---

* This chapter is partially reproduced from following published review papers:
J. Li, Y. Zheng, Optothermally Assembled Nanostructures. *Acc. Mater. Res.* **2021,** *2*, 352-363.
J. Li, E. H. Hill, L. Lin, Y. Zheng, Optical Nanoprinting of Colloidal Particles and Functional Structures. *ACS Nano* **2019,** *13*, 3783-3795.
J. Li, L. Lin, Y. Inoue, Y. Zheng. Opto-Thermophoretic Tweezers and Assembly. *J. Micro Nano-Manuf.* **2018**, *6*, 040801.
Z. Chen[#], **J. Li**[#], Y. Zheng. Heat-Mediated Optical Manipulation. *Chem. Rev.* **2021** ([#]equal contribution)
J. Li conducted the literature search and wrote these review paper as the first author or the co-first author.

focused electron beam to achieve direct etching of the substrate, which can provide a resolution down to a few nanometers.[11] However, this process is time-consuming and costly, preventing wider applications in large-scale manufacturing. Soft lithography and nanoimprint lithography can transfer patterns from a stamp with nanoscale structures onto a solid substrate to achieve fast and high-resolution (sub-10 nm) fabrication.[12, 13] However, the resolution is limited by the feature size of the stamp, which is usually fabricated via other costly methods such as electron-beam lithography. In addition, they appear to be more susceptible to the deformation of the stamp and the density of defects.

In addition to those top-down approaches, researchers have also exploited bottom-up assembly to fabricate different nanostructures. Self-assembly provides a low-cost way to autonomously build colloidal particles into large-scale patterns.[14] The self-assembled colloidal pattern can further be employed as a mask to fabricate large-scale periodic nanostructures, which is known as colloidal lithography.[15] By combining top-down fabrication and self-assembly approaches, template-assisted self-assembly has been developed to create various functional structures with an accurate design.[16, 17] Direct writing is another common bottom-up approach, such as inkjet printing and dip-pen nanolithography. Inkjet printing is a maskless and highly efficient method, which involves the controlled ejection of "ink" onto the substrate through a nozzle.[18] Dip-pen nanolithography applies an atomic force microscope tip "pen" coated with molecule-based "ink" to write on a target substrate.[19]

1.2 OPTICAL NANOPRINTING TECHNIQUES

Recently, optical nanoprinting has emerged as an alternative strategy to construct superstructures using individual colloidal particles as building blocks.[20-22] Optical

nanoprinting paves the path for fabrication of multifunctional nanostructures for various nanotechnological applications, such as optical metamaterials,[23, 24] and photonic devices.[25, 26] In this section, the state-of-the-art optical nanoprinting techniques achieved by different physical mechanisms are briefly reviewed (Figure 1.1).

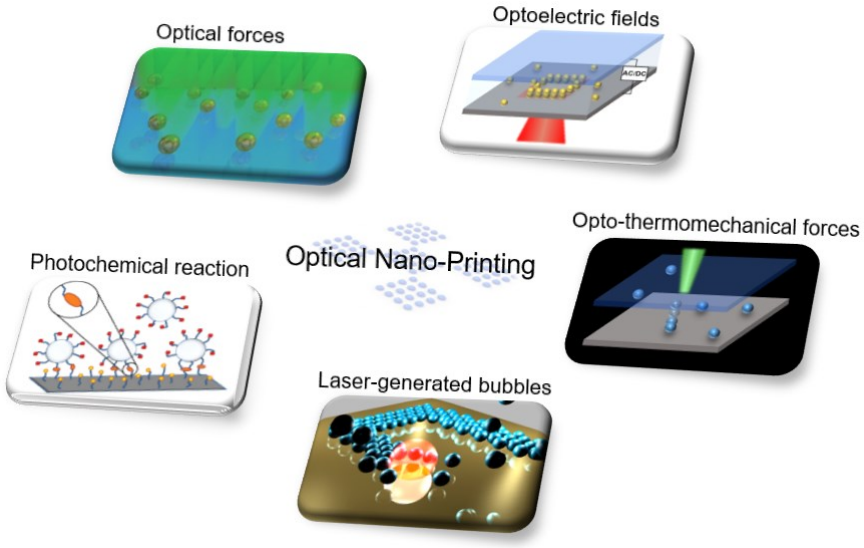

Figure 1.1: Schematic illustration of optical nanoprinting techniques with different physical mechanisms.

First, optical forces are widely exploited for the manipulation and printing of colloidal nanoparticles. Feldmann and coworkers reported direct optical printing of single gold nanoparticles (AuNPs) with a resonant laser.[20] When the incoming laser is of a similar wavelength as the localized surface plasmon resonances of the AuNPs, the enhanced interaction between AuNPs and light gives rise to plasmon-enhanced optical forces. AuNPs illuminated by the laser are drawn toward the beam center by the radial force and pushed down toward the substrate by the axial force. Laser printing happens when the optical

forces surpass the electrostatic repulsion between charged particles and substrate to enable the immobilization of AuNPs on the substrate by van der Waals interactions. By optimizing the wavelength and the optical power of the laser, single 100 nm AuNPs could be precisely printed on the target position with an accuracy of 50 nm. Arbitrary patterns can be formed by printing nanoparticles one by one, and the printed NPs can resist repeated cleaning and rinsing due to strong van der Waals forces. Additionally, the high transient power density of femtosecond laser can also enable direct optical printing of colloidal nanoparticles. For instance, Sun and coworkers reported a femtosecond laser direct writing method for the controlled assembly of metal nanostructures[27] quantum dots.[28] The use of optical forces offers a simple solution to directly print nanoparticles that strongly interact with light.

In addition to optical forces, hybrid forces in a light-controlled external field have been harnessed for the printing of nanoparticles. Light illumination on a photosensitive substrate generates electron-hole pairs and increases the conductivity in the illuminated area to create "virtual electrodes" that locally concentrate the electric field. The resulting non-uniform electric field exerts a dielectrophoretic force on particles through the interaction of the induced dipole moments in particles and the surrounding media. Wu and coworkers developed an optoelectronic platform for dynamic light-actuated printing of nanoparticles.[29] An optical pattern is projected onto a photosensitive hydrogenated amorphous silicon layer to create a non-uniform electric field under an alternate current (AC) bias. Under this non-uniform electric field, the light-actuated electroosmotic flow and electrothermal flow contribute to the long-range collection of particles, and the dielectrophoretic forces lead to the short-range attraction and immobilization of nanoparticles at the illuminated area. The combination of these electrokinetic forces provides a versatile tool for low-power and high-throughput printing of large-area patterns. Furthermore, the linewidth and density of immobilized structures can be controlled by

tuning the AC voltage source parameters (e.g., peak-to-peak voltage and frequency), light source parameters (e.g., optical intensity and beam size), and operational parameters (e.g., exposure time and scanning speed).

Opto-thermomechanical printing exploits the coupling between photothermal effects and mechanical forces to control the motion of nanoparticles. One strategy is called laser-induced transfer, which involves local melting of the donor film and ejection of melted droplets towards the receiver substrate.[30] Another example is to release nanoparticles from a donor substrate externally. For instance, Zhao and coworkers reported the releasing and placing of AuNPs based on the laser-induced thermal expansion of soft substrates.[31]

In another optical printing technique, optothermal microbubbles are generated by laser heating and exploited for the patterning of colloidal particles, which is termed bubble printing.[32] Particles are driven toward the microbubble via Marangoni convection induced by the stress tension gradient at the bubble surface and immobilized on the substrate by van der Waals interactions. The microbubble diameter and the size of the printed colloidal assemblies can be precisely controlled by tuning the optical power density, which enables bubble-pen lithography to print particles with a wide range of sizes. By steering the laser beam and controlling the on/off state of the laser, bubble printing can realize both continuous writing of particle assemblies and one-by-one patterning of single particles into arbitrary patterns.

Last, photochemical printing of colloidal particles is achieved by applying light-controlled chemical reactions to anchor or immobilize surface-functionalized nanoparticles. Recently, Fischer and coworkers reported in situ immobilization of dynamic assemblies of colloidal particles by UV-triggered click-chemistry.[33] The underlying click reaction is the “thiol-yne” alkyne hydrothiolation, which is an organic reaction between a

thiol and an alkyne to form a covalent bond. This reaction is fast, efficient, general to arbitrary particles, and can work in the presence of external optical and magnetic fields. Functionalized particles can be permanently captured onto functionalized glass surfaces with just a few seconds of UV irradiation. In combination with optical tweezers used to trap particles at desired locations and in arbitrary configurations, this photoclick strategy can be applied for the fast and dynamic fabrication of colloidal microstructures.

1.3 OPTOTHERMAL PHENOMENA FOR MANIPULATION AND ASSEMBLY OF NANOMATERIALS

The entropically favorable photon-to-phonon conversion and tailorable thermal management can facilitate the creation and dynamical control of the desired temperature field with low optical intensity and simple setups. By exploiting the various thermal forces and motions in the light-controlled temperature field (Figure 1.2), versatile manipulation and assembly of various objects with diverse materials, shapes, and sizes (ranging from nanoscale to macroscale) can be achieved in different environmental media.

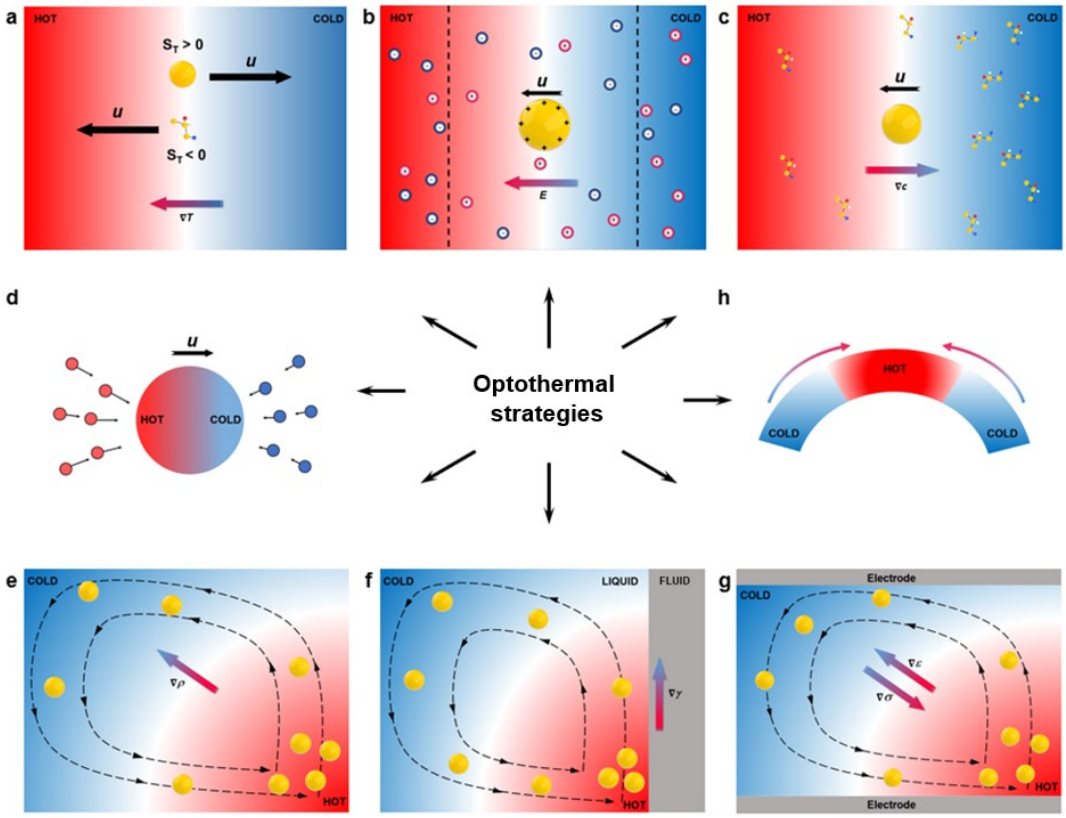

Figure 1.2: Schematics of the overview of optothermal phenomena for the manipulation of nanomaterials. (a) Thermophoresis. (b) Thermoelectricity. (c) Heat-mediated diffusiophoresis. (d) Photophoresis. (e) Natural convection. (f) Heat-mediated Marangoni convection. (g) Electrothermoplasmonic flow. (h) Optothermal shape deformation.

Under a temperature gradient field, colloidal species experience thermally directed migration along the temperature gradient, which is known as thermophoresis or thermal diffusion (Figure 1.2a).[34-36] In general, the drift velocity $\boldsymbol{u}$ for a particle is given by

$$\boldsymbol{u} = -D_T \nabla T \tag{1}$$

where D_T is the thermophoretic mobility and ∇T is the temperature gradient. For a diluted suspension, the mass flow J is expressed as $J = -D\nabla c - cD_T\nabla T$, where D is the

Brownian diffusion coefficient, and c is the particle concentration. At the steady state ($J = 0$), ∇c is given by[37]

$$\nabla c = -c\frac{D_T}{D}\nabla T = -cS_T\nabla T \quad (2)$$

where $S_T = D_T/D$ is the Soret coefficient. Since different colloidal species have Brownian diffusion coefficients D with differences up to several orders of magnitudes, the Soret coefficient S_T provides a more general description of thermophoretic migration. When $S_T > 0$, suspended particles are thermophobic and move from the hot to the cold region; otherwise, particles are thermophilic and transport from the cold to the hot region with $S_T < 0$. In general, most colloidal particles are thermophobic under ambient conditions.[35] The magnitude of S_T also indicates the scale of the particle concentration gradient in a temperature field.

Thermophoretic migration can be regulated by adding additional ions into colloidal particle suspensions[38] through the establishment of thermoelectric fields.[39, 40] In brief, depending on their Soret coefficients,[41] different ions migrate at different velocities and directions under a temperature gradient via thermophoresis, leading to a spatial separation of ion species with opposite charges. Consequently, when the ionic redistribution reaches a steady state in a closed system, a thermoelectric field E_T is established, which is also termed Seebeck effect (Figure 1.2b):[42]

$$E_T = S\nabla T = \frac{k_B T\nabla T}{e}\frac{\sum_i Z_i n_i S_{Ti}}{\sum_i Z_i^2 n_i} \quad (5)$$

where S is the Seebeck coefficient, T is the environmental temperature, i indicates the ionic species, k_B is the Boltzmann constant, e is the elementary charge, and Z_i, n_i, and S_{Ti} represent the charge number ($Z_i = \pm 1$ for positive and negative monovalent ions), the concentration, and the Soret coefficient of i species, respectively.

Besides thermophoresis-induced particle migration, the presence of a temperature gradient field can also result in the generation of other non-uniform gradients, leading to the directed motion of colloids. For instance, diffusiophoresis shows the transport of colloidal particles under a concentration gradient of solute (Figure 1.2c), which is induced by the slip velocity at the particle-liquid interface.[43] Depletion attraction is a typical type of diffusiophoretic force generated from the concentration gradient of suspended small molecules in the colloid-molecule mixture. When the particle has a different temperature (ΔT) or thermal accommodation coefficient ($\Delta\alpha$) at the surface, photophoretic migration can be induced via the momentum transfer between the particle and the surrounding molecules (Figure 1.2d).[44, 45]

In addition, the temperature gradient field can lead to the formation of different optothermal flows. Specifically, the local heating in the solution can cause a density gradient of the fluid or a surface tension gradient at the fluid-fluid interface, which induces a natural convection flow (Figure 1.2e) [46] and a Marangoni convection flow (Figure 1.2f), respectively.[47] Under an external electric field, the localized heating of fluid creates the local gradients in fluid's permittivity ($\nabla\varepsilon$) and electrical conductivity ($\nabla\sigma$), which lead to the generation of an electrothermoplasmonic flow (Figure 1.2g).[48] These optothermal flows can facilitate the rapid transport and delivery of colloidal particles for efficient optical manipulation and assembly.[49] Optical heating can also lead to optothermal shape deformation via volume expansion, phase transition, molecular sorption/desorption, and surface acoustic wave (Figure 1.2h).[50-52] Optothermal effects can further result in localized laser ablation for on-demand sculpturing nanomaterials.

The research works covered in this dissertation are primarily based on these optothermal phenomena, which will be discussed in detail in the following chapters. Specifically, thermophoresis, thermoelectricity, diffusiophoresis (depeletion), and

optothermal shape deformation are involved. By controlling the thermophoretic migration of colloids and ion species in solution, trapping and assembly of diverse colloidal particles can be achieved. The novel laser cooling strategy can also be applied for the general thermophoretic trapping of particles and molecules (see **Chapter 2**). The manipulation and assembly of colloidal nanostructures can be extended from the solution phase to the solid phase through the thermal engineering of particle-substrate interactions. Reconfigurable assembly of functional nanostructures on a solid substrate is demonstrated (see **Chapter 3**). Last, optothermal nanolithography of two-dimensional (2D) materials is developed by harnessing the plasmon-enhanced optothermal ablation (see **Chapter 4**).

Chapter 2: Opto-Thermophoretic Manipulation and Assembly in the Solution

2.1 OPTO-THERMOPHORETIC ASSEMBLY†

Under a light-generated temperature field, thermophoresis is a generalized force on particles, cells, or molecules and drives them to cold or hot regions. Thus, the particles are either repelled away or attracted to the laser beam depending on their Soret coefficients. In nature, most colloidal species show a thermophobic behavior and move to the cold region under a thermal gradient.[53] To achieve opto-thermophoretic trapping of single objects by optical heating, Cichos and co-workers developed a strategy to dynamically heat closed plasmonic nanostructures (e.g., gold nanohole structure). In this way, a localized temperature field is generated with the gold region at the center to trap individual objects inside the plasmonic nanostructure via thermophoresis.[54] By integrating a feedback control on the heating laser, Cichos and co-workers further extend the trapping capabilities to precisely control the trapping position in the closed nanostructure and enable the trapping of single molecules, such as λ-DNA molecules.[55]

The dynamic temperature field shows the possibility of manipulating particles or macromolecules with well-defined temperature gradients. However, the trapping is limited to an ultrathin water film (< 1 μm) and lacks the capability for dynamic manipulation of particles. Lin et al. proposed the opto-thermophoretic tweezers based on entropic responses and permittivity gradients at the particle-solvent interface under an optically generated thermal gradient.[56] The temperature gradient is generated by laser heating of a thermoplasmonic substrate composed of quasi-continuous gold nanoparticles.[32, 57, 58] Stable

† This chapter is reproduced from following published manuscript:
X. Peng[#], **J. Li[#]**, L. Lin[#], Y. Liu, Y. Zheng. Opto-Thermophoretic Manipulation and Construction of Colloidal Superstructures in Photocurable Hydrogels. *ACS Appl. Nano Mater.* **2018**, *1*, 3998-4004.
J. Li is the co-first author of this paper.

trapping and dynamic manipulation of polystyrene (PS) beads with different sizes have been demonstrated. Besides colloidal particles, manipulation of biological cells and vesicles with entropy-driven thermophoretic tweezers has been realized.[59, 60]

In addition, opto-thermoelectricity is exploited to enable a more general opto-thermophoretic trapping and assembly. A cationic surfactant, cetyltrimethylammonium chloride (CTAC), is added into the solution to enable opto-thermoelectric tweezing.[61] In brief, CTAC surfactant can coat the colloidal particle surface and form a molecular double layer, making the particle with positive charge. Simultaneously, CTAC molecules self-assemble into positive micellar ions above the critical micelle concentration (0.13-0.16 mM). When a laser beam is directed to heat a thermoplasmonic substrate, a temperature gradient is generated. Both the positive CTAC micelles and negative Cl^- migrate from the hot to the cold region by thermophoresis, drifting away from the laser spot. Since S_T (micelle) > S_T (Cl^-), CTAC micelles move further than Cl^- ions. The spatial separation of positive CTAC micelles and negative Cl^- ions generated a thermoelectric field pointing towards the laser beam, driving the positively charged particle to be trapped by the laser beam. Opto-thermophoretic tweezers display the potential to trap wide ranges of colloidal particles and biological cells with a significantly reduced optical intensity compared with optical tweezers.

Lin et al. further demonstrated the opto-thermophoretic assembly of colloidal particles into arbitrary configurations[62]. In addition to enabling the opto-thermophoretic trapping and manipulation of colloidal particles, CTAC micelles act as depletants that are driven outside the interparticle gap of two particles, generating a depletion attraction force to bind the colloidal assembly. After the laser is turned off, the assembly can be maintained. Diverse colloidal superstructures composed of colloidal particles with various materials, sizes, and shapes can be precisely built using opto-thermophoretic assembly.

Despite the versatility in the assembly of colloidal matter, the assembled structures cannot be maintained after the removal of the solution due to the capillary collapse. To overcome this limitation, we developed opto-thermophoretic trapping and assembly of colloidal nanostructures in photocurable hydrogels.[63] With post-photopolymerization of the hydrogels, we achieve the all-optical fabrication of diverse colloidal superstructures. This general concept is shown in Figure 2.1. Colloidal particles are suspended in a mixture of CTAC and a photocurable hydrogel. The hydrogel consists of 10% poly(ethylene glycol) diacrylate (PEGD) 3400 polymers as the cross-linking reagent and 0.05% Irgacure 2959 as the photoinitiator. The sample is sandwiched between a thermoplasmonic substrate and a glass cover slide. A temperature gradient is created by irradiating a laser beam onto the thermoplasmonic substrate consisting of a high density of Au nanoparticles, where the excitation of surface plasmons leads to high light-to-heat conversion efficiency. The difference in Soret coefficients between positive CTAC micelles and negative Cl^- counterions causes spatial ionic separation. Thus, a localized thermoelectric field is built to trap the positive particle (Figure 2.1a). Once the particle is trapped and delivered to a target location, ultraviolet (UV) light is applied to trigger the cross-linking reaction among dispersed PEGD chains and lock the particle onto the substrate, leading to the immobilization of the particle (Figure 2.1b). A real-time process of trapping and immobilization of a 1 μm PS bead is shown in Figure 2.1c.

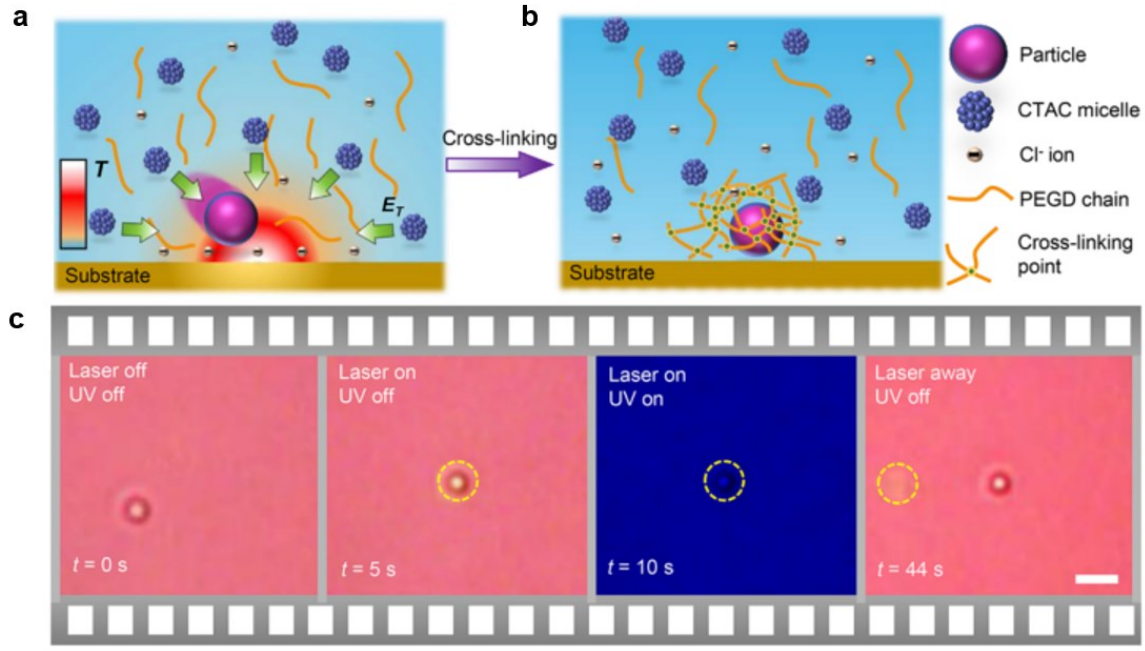

Figure 2.1: Opto-thermophoretic trapping and patterning of a colloidal particle in a hydrogel solution. (a) Schematic showing the trapping of a colloidal particle in a thermoelectric field. (b) Schematic showing the immobilization and patterning of the trapped colloidal particle through UV cross-linking. (c) Sequential optical images showing the trapping and patterning of a 1 μm PS sphere in a hydrogel solution. Scale bar: 2 μm.

We have also achieved the parallel trapping and patterning of arrays of 1 μm PS beads. For instance, by splitting a single laser beam into multiple laser beams using a digital micromirror device, we successfully trapped and patterned 4 PS beads into a rhombus pattern (Figure 2.2a) and 6 PS beads into a 2 x 3 array (Figure 2.2b). This capability of parallel manipulation can significantly enhance the manipulation efficiency and throughput of this approach for large-scale optical fabrication.

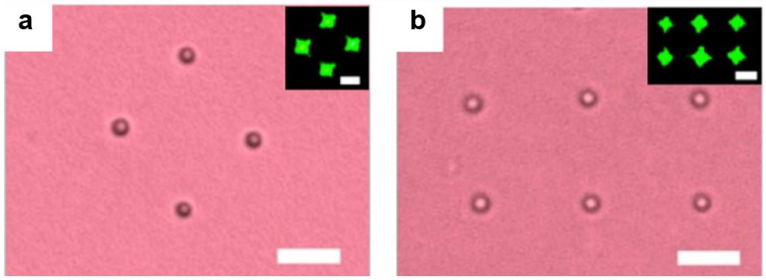

Figure 2.2: Parallel trapping and patterning of 1 μm PS spheres into (a) a rhombus and (b) a 2 x 3 array in a hydrogel solution with 20 mM CTAC. The inset images show the corresponding trapping beams created with a digital micromirror device. Scale bars in (a) and (b): 5 μm. Scale bars in the insets: 2 μm.

To show the capability of this approach, we built diverse colloidal superstructures with colloidal particles of various sizes, dimensions, and compositions. The interparticle depletion attraction interaction acts as the primary "bonding" force to assemble the superstructures in hydrogels, which are further immobilized via photopolymerization. Figure 2.3a-c shows 2D close-packed colloidal superstructures of 1, 2, and 5 μm PS spheres, respectively. It is worth noting that the as-built superstructures remained intact even after the samples were rinsed and dried. The scanning electron micrograph (SEM) in Figure 2.3c shows the superstructure on the substrate after removing the solution and rinsing the substrate. Figure 2.3d shows a one-dimensional (1D) chain of 2 μm PS spheres. Figure 2.3e shows a 2D Saturn-ring structure consisting of a 5 μm PS sphere surrounded by eight 2 μm PS spheres. By further incorporating optical scattering force into the opto-thermophoretic system, we achieve out-of-plane manipulations to build three-dimensional (3D) superstructures. As an example, we show a 3D tetrahedron superstructure with four 2 μm PS spheres (Figure 2.3f). To demonstrate the capability of building hybrid colloidal superstructures with particles of different compositions and sizes, we managed to arrange 5 μm PS spheres and 2 μm silica particles

into two types of configurations (Figure 2.3g,h). Figure 2.3i,j shows that three PS spheres with different sizes are arranged into left-handed or right-handed chiral configurations.

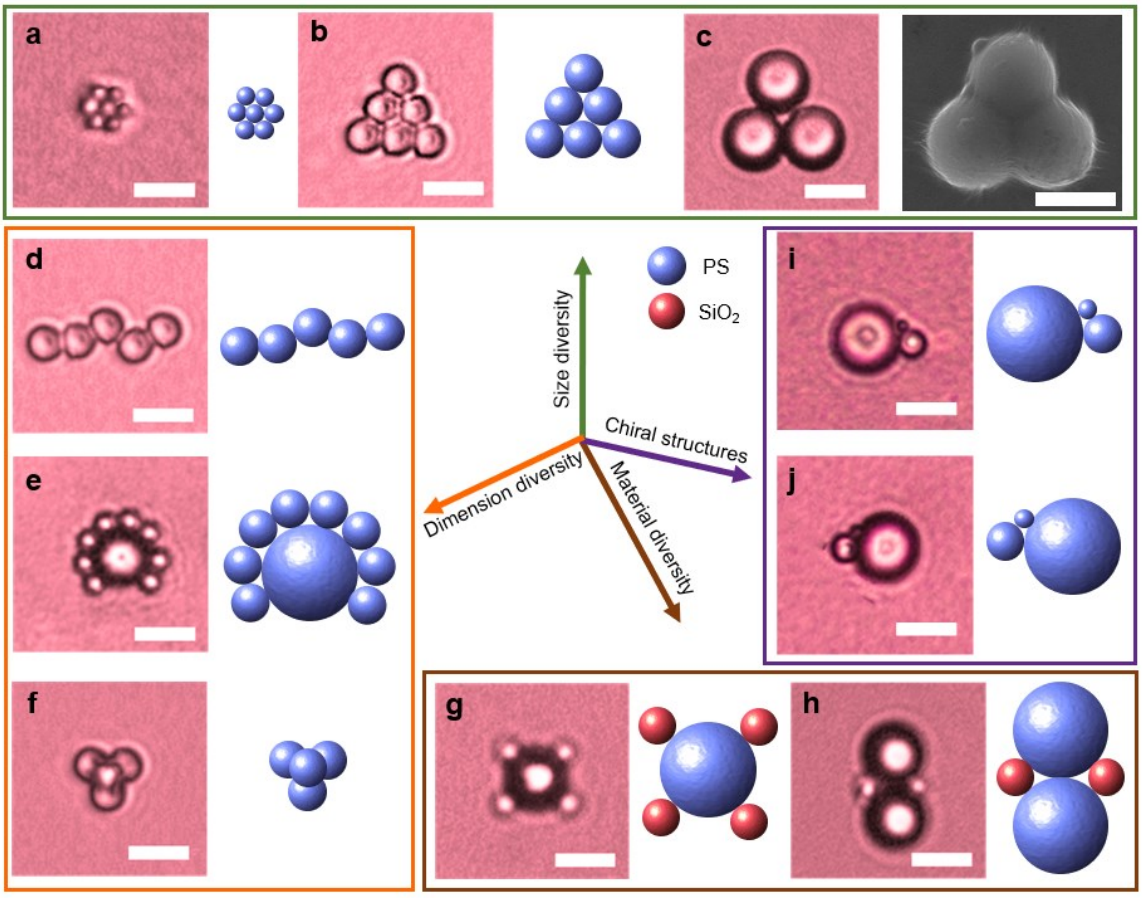

Figure 2.3: Opto-thermophoretic assembly and patterning of various colloidal superstructures in hydrogel solutions. Assembly of (a) 1, (b) 2, and (c) 5 μm PS spheres into 2D close-packed superstructures. The inset in (c) shows the SEM image of the corresponding superstructure after cross-linking of the hydrogel. (d) 1D assembly of 2 μm PS spheres. (e) 2D hybrid assembly of a Saturn-ring superstructure with one 5 μm PS sphere and eight 2 μm PS spheres. (f) 3D assembly of a close-packed tetrahedron superstructure with four 2 μm PS spheres. (g) 2D hybrid assembly of one 5 μm PS sphere surrounded with four 2 μm silica spheres. (h) 2D hybrid assembly of two 5 μm PS spheres and two 2 μm silica spheres. (i, j) 2D hybrid assembly of a 1, 2, and 5 μm PS sphere into two close-packed superstructures with opposite chirality. All Scale bars are 5 μm.

In summary, by exploiting micelle-mediated opto-thermoelectric fields for colloidal manipulation in hydrogels and UV-induced photopolymerization of the hydrogels, we have developed an opto-thermophoretic patterning technique for versatile assembly of colloidal particles on solid substrates. The thermophoresis of the CTAC micelles, particle-substrate and particle-particle depletion, and the micelle-polymer bonding contribute to the opto-thermophoretic trapping. Using colloidal particles in a wide range of sizes and compositions as the building blocks, we demonstrate the assembly of complex colloidal superstructures with diverse configurations. By integrating the in situ spectroscopic analysis into the opto-thermophoretic system, we can study the responses of colloidal superstructures to light fields. With its versatile, low-power, and noninvasive operation, the opto-thermophoretic patterning strategy will find applications in studies of light-matter interactions and nanofabrication of colloidal devices.

2.2 OPTO-REFRIGERATIVE TWEEZERS‡

The opto-thermophoretic manipulation and assembly are versatile in the trapping and assembly of colloids and cells. However, the potential optical heating may still cause thermal damages to fragile nanomaterials, cells, and biomolecules. In this section, a new type of light-based tweezers, termed opto-refrigerative tweezers, is developed to trap particles and molecules at the laser-generated cold spot by exploiting solid-state optical refrigeration and thermophoresis.

Optical tweezers were extensively applied to trap and manipulate colloidal particles and biological objects.[64-66] The invention of optical tweezers has stimulated striking

‡ This chapter is reproduced from following published manuscript:
J. Li, Z. Chen, Y. Liu, P. S. Kollipara, Y. Feng, Z. Zhang, Y. Zheng. Opto-Refrigerative Tweezers. *Sci. Adv.* **2021**, *7*, eabh1101.
J. Li is the first author of this paper.

advances in nanotechnology,[67, 68] physics,[69-72] and biological science.[73, 74] Despite this far-reaching progress, the diffraction limit makes it challenging to trap and manipulate nanoscale objects using optical tweezers.[75] Thus, a tightly focused laser beam with high optical intensity is usually required, which may cause photodamages and photothermal degradation to nanoparticles and biological samples.[76-78] A variety of strategies and techniques were proposed to overcome these limitations. Near-field optical nanotweezers exploit strong plasmon-enhanced optical forces to accurately trap nanoparticles and molecules at metallic nanoantennas[48, 79] or plasmonic nanoapertures[80, 81] with reduced optical power. However, the localized near-field enhancement may lead to strong plasmonic heating and limit the capability for dynamic manipulation. Alternatively, indirect optomechanical coupling under a light-controlled electric field or temperature field has been harnessed to manipulate particles and cells with low optical intensity and increased flexibility. Optoelectronic tweezers use light to create virtual electrodes and a nonuniform electric field to trap particles with dielectrophoretic forces.[82, 83] Opto-thermoelectric tweezers were developed to manipulate various colloidal particles under a laser-controlled thermoelectric field.[61] With a rational design of the optothermal substrate, precise opto-thermoelectric manipulation of nanoparticles was demonstrated with an ultralow optical power (~0.08 mW μm^{-2}).[84] However, the potential photothermal damages still exist, which may hinder their implementation in the research that involves fragile nanomaterials and thermosensitive biological specimens. Lately, Ndukaife and co-workers reported opto-thermo-electrohydrodynamic tweezers to trap and manipulate sub-10 nm objects away from the laser beam to avoid photo-toxicity and thermal stress.[85]

Herein, we develop opto-refrigerative tweezers (ORT) to dynamically manipulate objects at a laser-generated cold spot enabled by optical refrigeration and thermophoresis synergy.[86] Localized laser cooling in liquid media was realized with ytterbium-doped

nanocrystals and a 1,020 nm laser.[87, 88] Ytterbium-doped yttrium lithium fluoride (Yb:YLF) crystals with a bipyramidal morphology (Figure 2.4a) and a Scheelite structure (Figure 2.4b) were synthesized via a facile hydrothermal method. Optical refrigeration of Yb:YLF crystals is realized by anti-Stokes fluorescence in the crystals.[89-91] Briefly, the excitation at 1,020 nm is matched with the E4-E5 transition in Yb^{3+} and results in photon emission at shorter wavelengths, which leads to the internal cooling of the nanocrystals (Figure 2.4c).

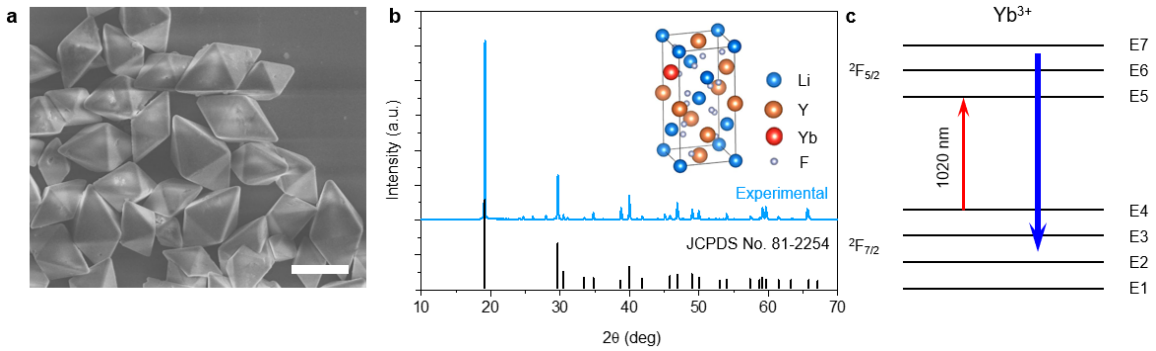

Figure 2.4: (a) SEM image of the synthesized Yb:YLF crystals. Scale bar: 10 μm. (b) Powder X-ray diffraction pattern of the synthesized Yb:YLF crystals. Inset: schematic of the crystal structure. A Scheelite structure was identified, which is consistent with the record X-ray diffraction pattern. (c) Mechanism of laser cooling via anti-Stokes fluorescence. The scheme shows the energy level diagram of the Yb^{3+} ion, in which the $F_{5/2}$ ground state and the $F_{7/2}$ excited state are split into a manifold of non-degenerate states. The arrows show the excitation at 1,020 nm and the anti-Stokes fluorescence at shorter wavelengths, which lead to the internal cooling of the crystal.

The general concept and working principle of ORT are shown in Figure 2.5. The localized laser cooling of the substrate generates a nonuniform temperature gradient field in the solution, in which colloidal particles and molecules can be trapped at the low-temperature region (i.e., the laser spot) via thermophoresis (Figure 2.5a). A quasi-continuous Yb:YLF layer was prepared as the substrate for the laser refrigeration and opto-

refrigerative trapping experiments. Figure 2.5b shows the temperature distribution at the substrate-liquid interface under laser cooling in situ measured by a thermal camera. A localized decrease of ~7.5 K in temperature was instantly observed at the laser beam center with an irradiation intensity of 25.8 mW μm^{-2}. The simulated out-of-plane temperature distribution also revealed a confined colder region at the laser spot (Figure 2.5c), indicating a temperature gradient pointing outward from the laser beam was built in a 3D way. The corresponding temperature gradient mapping is shown in Figure 2.5d, where a high gradient of > 1×10^7 K m^{-1} was obtained at the periphery of the laser beam center.

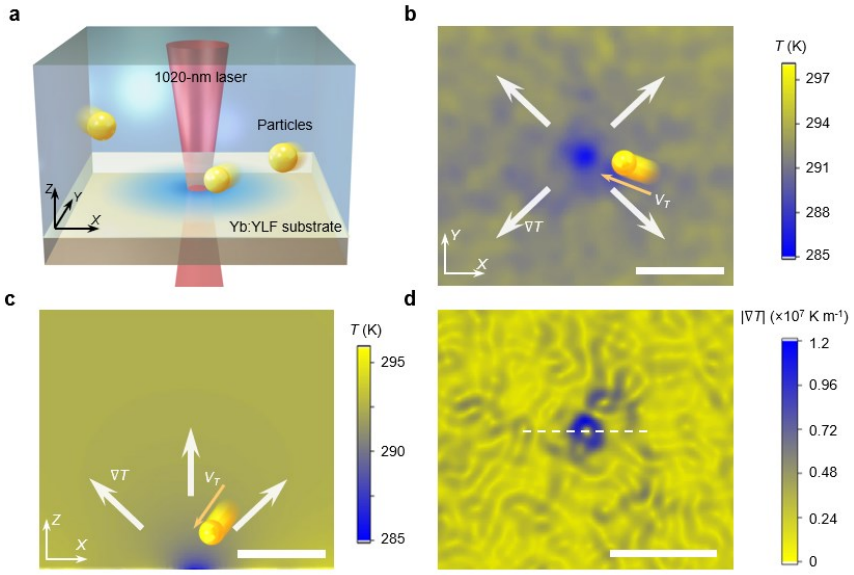

Figure 2.5: Working principle of ORT. (a) Schematic of localized laser cooling of Yb:YLF substrate and the thermophoretic trapping of particles at the cold spot. (b) Measured in-plane temperature distribution at the solution-substrate interface under laser cooling with an intensity of 25.8 mW μm^{-2}. (c) Simulated out-of-plane temperature distribution based on the temperature profile crossing the laser beam center in (b). In (b) and (c), a temperature gradient pointing outward from the cold spot is built. (d) In-plane temperature gradient mapping corresponding to (b). Scale bars: 10 μm.

The optical refrigeration of Yb:YLF crystals was further confirmed by measuring the upconversion emission from Yb/Er co-doped YLF nanocrystals. Under excitation with a 1,020 nm laser, strong green photoluminescence from Er^{3+} ions can be observed (Figure 2.6a). The photoluminescence spectra of a Yb^{3+}/Er^{3+}co-doped YLF nanocrystal under different excitation power are shown in Figure 2.6b. The green emission consists of two distinct bands of the $^2H_{11/2} \rightarrow {}^4I_{15/2}$ (centered at 525 nm) and $^2S_{3/2} \rightarrow {}^4I_{15/2}$ (centered at 545 nm) transitions of the Er^{3+} ion. The populations of these two excited states are in a thermal equilibrium governed by the Boltzmann factor[92], $\frac{I_2}{I_1} = Cexp(-\frac{\Delta E}{k_B T})$, where I_2 and I_1 are the integrated intensities from 515 to 535 nm and from 535 to 570 nm, respectively, *C* is a constant related to the properties of host materials, ΔE is the energy gap separating the two excited states, and k_B is the Boltzmann constant. The intensity ratio of the green fluorescence bands of the Er^{3+} ions are temperature-sensitive, which can be used to deduce the temperature changes of the nanocrystals. The above equation can be further rewritten into $-\frac{1}{T} = \frac{k_B}{\Delta E} ln \frac{I_2}{I_1} + C_1$. We calculated the integrated intensities of I_2 and I_1bands and plotted the relationship between $ln(I_2/I_1)$ and laser powers in Figure 2.6c. According to the above equation, a negative slope implies the cooling of Yb/Er:YLF in solution along with the increasing laser power.

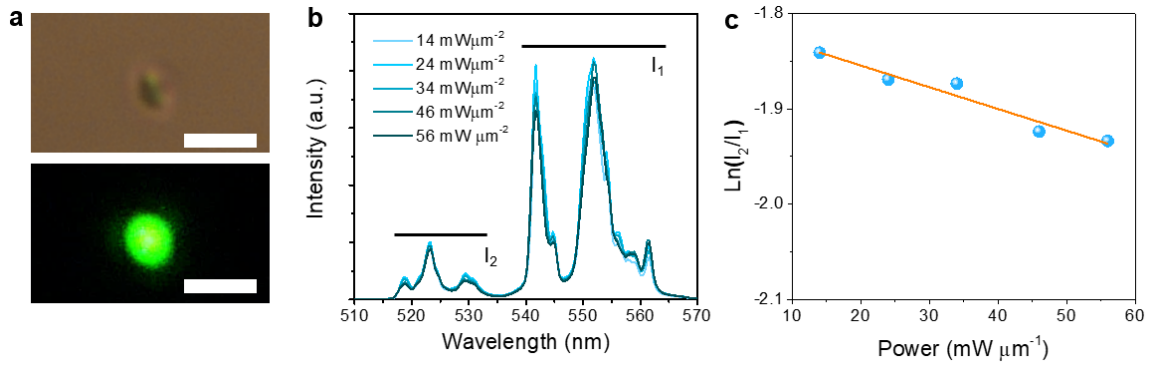

Figure 2.6: Laser cooling of Yb/Er co-doped crystals. (a) Optical images of a 10% $Yb^{3+}$and 2% Er^{3+}co-doped YLF nanocrystal under excitation with a 1,020 nm laser. Strong green photoluminescence from Er^{3+} ions can be observed. Scale bars: 2 μm. (b) Photoluminescence spectra of a Yb^{3+}/Er^{3+}co-doped YLF nanocrystal under different excitation power. (c) Natural logarithm of I_2/I_1 showing a linear decrease with laser irradiance.

The power-dependent laser cooling of the Yb:YLF substrate is shown in Figure 2.7a. With an increasing incident intensity from 20 to 41 mW μm^{-2}, a temperature decrease of ~ 6 to 10 K was observed, and the temperature gradient increased from 0.6 to 1.4 × 10^7 K m^{-1}. Under such a strong temperature gradient field ∇T, colloidal particles or molecules experience a thermodiffusive drift velocity (v_T)[53]

$$v_T = -DS_T\nabla T \quad (6)$$

where D is the diffusion coefficient, and S_T is the Soret coefficient. In general, most particles and molecules exhibit a thermophobic behavior with a positive S_T Which will migrate towards the colder region in a temperature gradient.[54, 55] In our case, thermophoresis drives particles and molecules to the laser-generated cold spot and traps them at the laser beam center. The effective thermophoretic trapping force in a solution can be written as[93]

$$F_T = \gamma v_T = -k_B T S_T \nabla T \quad (7)$$

where γ is the friction coefficient and related to the Boltzmann constant k_B by Stokes-Einstein relation $\gamma D = k_B T$. For a typical Soret coefficient of ~ 2-5 K^{-1} for colloidal nanoparticles,[54, 94] a maximum trapping force of ~200 fN and a trapping potential of ~45 $k_B T$ was obtained (Figure 2.7b), indicating that stable trapping of nanoparticles can be achieved.

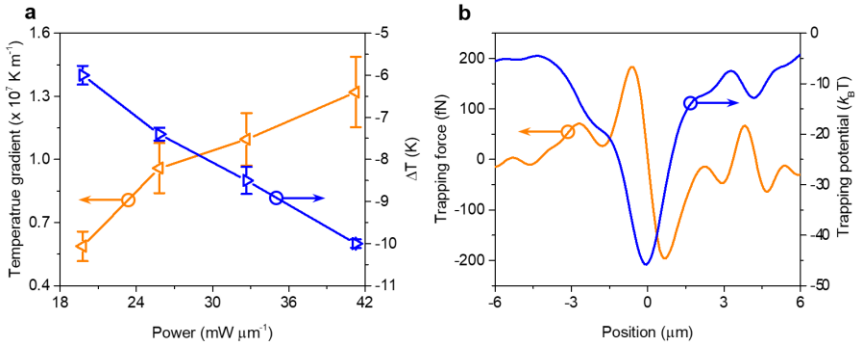

Figure 2.7: (a) Power-dependent laser cooling. The average temperature drops at the laser beam center and the peripheric temperature gradient values were plotted. (f) The effective thermophoretic trapping force and the trapping potential along the white dashed line in Figure 2.5d. A Soret coefficient of 4 K^{-1} was used. The position of the laser beam center was set to be 0.

We used 200 nm fluorescent polystyrene PS nanoparticles to demonstrate the capability of ORT for single particle trapping and manipulation. Figure 2.8a shows the attraction, trapping, and subsequent release of a PS nanoparticle. Compared with optical tweezers and plasmonic tweezers, trapping in a temperature gradient field has the advantage of a long working range to effectively trap nanoparticles located at a distance of more than 10 μm away from the laser beam center. Figure 2.8b shows that the trapped particle can be dynamically transported to any location on the Yb:YLF substrate. It should be noted that optical force is much smaller than thermophoretic force in our trapping experiments. In addition, when the laser was moved away from the Yb:YLF substrate to

the glass, the trapped nanoparticle was immediately released, indicating that thermophoretic force provided by optical refrigeration is the main driving force in ORT.

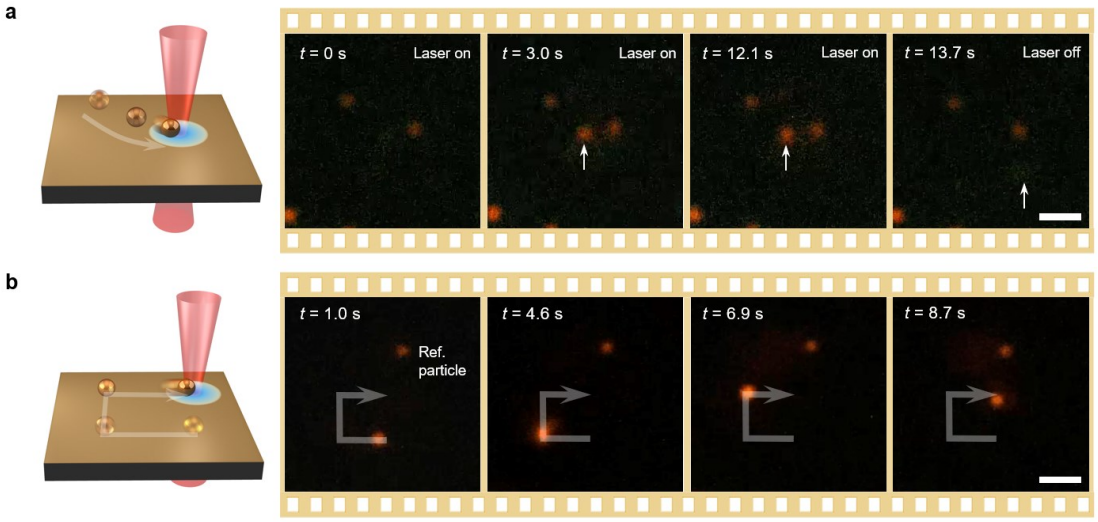

Figure 2.8: Trapping and manipulating single nanoparticles with ORT. (a) Trapping and releasing a 200 nm PS nanoparticle. (b) Dynamic manipulation of a 200 nm PS nanoparticle. The white arrows in (a) and (b) indicate the position and the trajectory of the target particle, respectively. Laser intensity: ~25 mW μm^{-2}. Scale bars: 5 μm.

To assess the trapping stability of ORT, we measured the trapping stiffness by tracking the trajectories of a trapped 200 nm PS nanoparticle. Figure 2.9a shows a typical position distribution of the nanoparticle trapped by ORT with a laser intensity of 20 mW μm^{-2}. With the increase of optical intensity, the nanoparticle became more confined to the laser beam center. We further fitted the histograms of the particle displacement (Figure 2.9b) with a Gaussian function to measure the variance σ and extracted the trapping stiffness $\kappa = \frac{2k_B T}{\sigma^2}$.[95] A high trapping stiffness of 0.5 to 4 pN μm^{-1} was obtained, corresponding to a laser intensity of 20 to 41 mW μm^{-2}, which is consistent with the values calculated from temperature mapping (Figure 2.9c). Our trapping stiffness is comparable

with near-field trapping on plasmonic nanodimers for a single 200 nm PS nanoparticle, while our optical intensity is one order of magnitude lower.[75] We note that the theoretical trapping stiffness based on the temperature gradient profiles is slightly smaller than the experimental results extracted from the particle tracking; this discrepancy is probably caused by the limited spatial resolution in the temperature measurement.

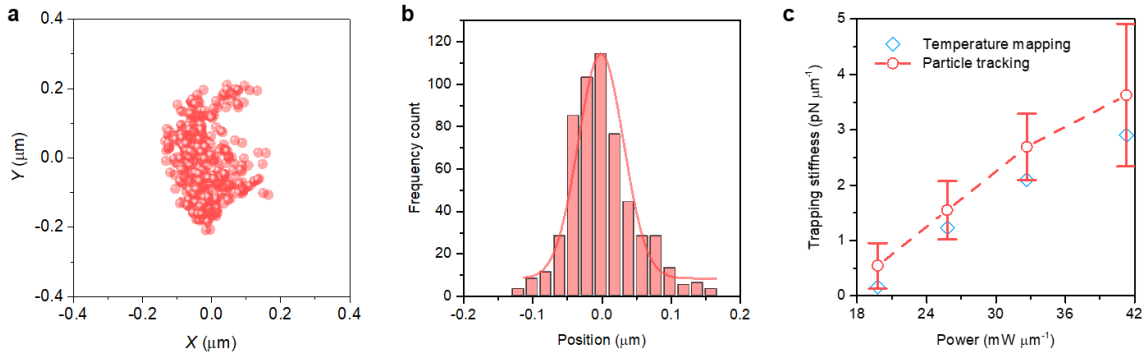

Figure 2.9: (a) A typical position distribution of a 200 nm PS nanoparticle trapped by ORT with an optical intensity of 20 mW μm^{-2}. (d) The corresponding histogram of particle displacement (*x*-direction). (c) Power-dependent trapping stiffness of a 200 nm PS nanoparticle trapped by ORT. Both experimental trapping stiffness from particle tracking and theoretical trapping stiffness from temperature mapping are plotted.

Besides providing a general platform to trap nanoparticles and molecules with thermophobic nature based on thermophoresis, ORT stands out for research in colloidal sciences and biology due to the capability to trap and manipulate objects with low damages. Compared to optical tweezers, ORT relies on a temperature gradient field to trap the target objects. A weakly focused laser beam (NA = 0.5-0.7) with lower intensity was used to remarkably reduce the photon-induced damages. Meanwhile, the intrinsic feature of trapping objects in the cold region avoids the common photothermal heating and the resultant thermal degradation in other optical tweezing platforms. As a demonstration, we

compared the quenching of 200 nm fluorescent PS nanoparticles trapped by ORT and optical tweezers (Figure 2.10a). The PS particle exhibited a dramatic drop in the fluorescence intensity for conventional optical tweezers, while the PS particle trapped by ORT only showed a slight decrease (Figure 2.10b). The fluorescence intensity decreased to ~ 65 % for optical tweezers and remained at > 90 % for ORT (Figure 2.10c). This enhanced stability of trapped objects is attributed to the suppression of both photobleaching and thermal bleaching in ORT.[96]

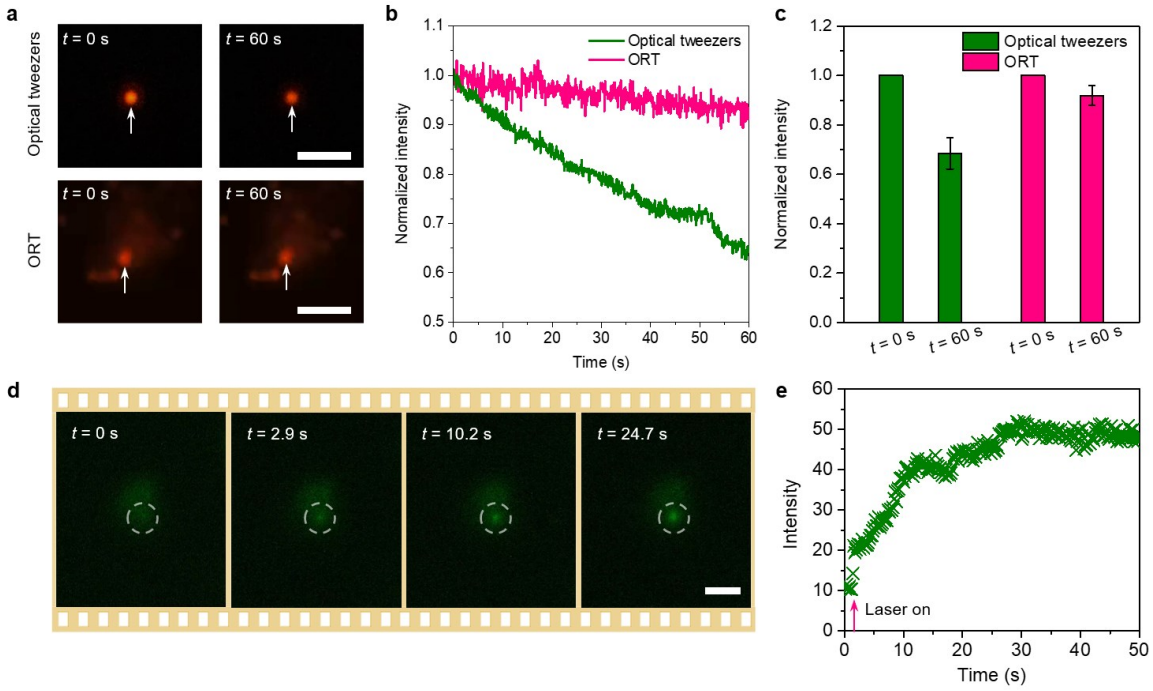

Figure 2.10: Noninvasive trapping of nanoparticles and biomolecules with ORT. (a) Optical images of a single 200-nm PS nanoparticle before and after being trapped by optical tweezers (top) and ORT (bottom) for 1 min. (b) Time-resolved fluorescence intensity of the PS particle trapped by optical tweezers and ORT. (c) Normalized fluorescence intensity changes after the PS particle was trapped for 1 min. (d) Successive optical images showing the trapping and concentration of FITC-conjugated protein A/G. (e) Time resolve intensity at the laser spot during the concentration of FITC-conjugated protein A/G. Scale bars: 5 μm.

In addition to dye-doped nanoparticles, most biomolecules are sensitive to environmental temperature. For example, many proteins and RNA molecules are subject to thermal degradation at high or even ambient temperature[97, 98]. Therefore, ORT offers the new possibility to trap these biomolecules and simultaneously cool down their environmental temperature (ΔT > 10 K), which significantly enhances the stability of thermosensitive molecules. A proof-of-concept demonstration is presented in Figure 2.10d, where FITC-conjugated protein A/G was trapped and concentrated at the laser-generated cold spot via ORT. This noninvasive optical concentration of biomolecules is promising in studying molecular interactions for disease diagnosis and drug development.[99, 100]

In summary, we developed ORT through the innovative coordination of optical refrigeration and thermophoresis. For the first time, it presents a new type of optical tweezing tool that enables the trapping of objects in the low-temperature region to avoid photothermal damages. Since it is based on a temperature gradient field, ORT allows the long-range trapping with a low-intensity and weakly focused laser beam, which can reduce the photon degradation of target objects.

The common thermophobic nature and positive Soret coefficients make ORT a general manipulation tool for nanoparticles and molecules of a broad range of compositions. However, it should be noted that negative Soret coefficients can be observed in certain circumstances where ORT is not applicable. For instance, the presence of surfactants in the solution can alter the thermophoretic response of colloidal particles.[101] Currently, the substrate, i.e., Yb:YLF nanoparticle layer, is prepared by a simple drop-cast method. Alternative approaches such as doctor blade coating[102] can be applied to improve the surface uniformity of the substrate. In addition, the large width of trapping potential may lead to the trapping of multiple particles when the particle concentration is high. One possible way to ensure the capability to trap single objects is to design a narrow trapping

potential that is comparable to the size of the target particle by using a single Yb:YLF nanocrystal as the cooling substrate.

As a newly developed technique, ORT still has several limitations, and future efforts can be made to further enhance its strengths. With the capability of stable trapping, dynamic manipulation, and non-invasive operation, ORT will serve as a powerful nanotool to open new opportunities for many fields, including materials science, physical chemistry, and biological science.

Chapter 3: Optothermal Manipulation and Assembly on the Solid Substrate

3.1 OPTOTHERMALLY-GATED PHOTON NUDGING§

Constructing colloidal particles into functional nanostructures, materials, and devices is a promising yet challenging direction. Many optical techniques have been developed to trap, manipulate, assemble, and print colloidal particles from aqueous solutions into desired configurations on solid substrates. However, these techniques operated in liquid environments generally suffer from pattern collapses, Brownian motion, and challenges that come with reconfigurable assembly. In this section, an all-optical technique, termed optothermally-gated photon nudging, is developed for the versatile manipulation and dynamic patterning of a variety of colloidal particles on a solid substrate at nanoscale accuracy.

The state-of-the-art chemical synthesis techniques permit the production of colloidal particles with precisely tunable sizes and shapes, tailorable compositions, and unique properties.[103-107] To build these colloidal particles into functional devices, the particles need to be assembled into the desired nanostructures and transported from an aqueous solution onto a solid substrate. A number of optical techniques, including optical tweezers, have been invented to trap, manipulate, and assemble colloidal particles in fluidic environments at single-particle resolution.[22, 64, 79, 83, 108] However, the desired immobilization of the optically assembled colloidal structures onto solid substrates is not trivial. Along this line, various optical printing methods have been developed to pattern

§ This chapter is reproduced from following published manuscript:
J. Li, Y. Liu, L. Lin, M. Wang, T. Jiang, J. Guo, H. Ding, P. S. Kollipara, Y. Inoue, D. Fan, B. A. Korgel, Y. Zheng. Optical Nanomanipulation on Solid Substrates via Optothermally-gated Photon Nudging. *Nat. Commun.* **2019**, *10*, 5672. J. Li is the first author of this paper.

colloidal particles onto substrates (see Section 1.2),[109] such as optoelectric printing,[29] plasmon-enhanced laser printing,[20] photochemical printing,[33] optothermal printing,[36] and bubble printing.[32] Despite their ability to pattern colloidal particles into various configurations, one major drawback for printing particles in liquid environments is that the strong capillary force can change the positions of particles and cause the pattern collapse.[110, 111] Additionally, Brownian motion of nanoparticles in the colloidal suspension can interrupt the manipulation process and limit the printing precision.[112, 113] Van der Waals interactions are strong enough to be exploited to firmly bond particles on the substrate;[20] however, reconfigurable patterning is impossible in this case, which prevents the on-demand construction of active nanoarchitectures.

An alternative strategy to overcome these limitations is to dynamically manipulate nanoparticles on a solid substrate. An atomic force microscope (AFM) can manipulate nanosized particles on a flat substrate with nanometre accuracy.[114-117] Unfortunately, AFM manipulation relies on physically pushing the particle with a sharp AFM tip, which often causes undesired tip and particle deformation as well as particle adhesion to the tip. In comparison to the solid-liquid interfaces, the van der Waals friction at the solid-solid interfaces is much stronger, which makes the manipulation of particles on solid substrates a considerable challenge.[118, 119] Thus, the key to the effective manipulation of particles on a solid substrate lies in the modulation of interfacial interactions to reduce the friction forces.

Herein, we report a solid-phase optical nanomanipulator, which provides a non-invasive and contactless strategy to achieve versatile nanomanipulation of colloidal particles and nanowires on a solid substrate through interfacial engineering. Briefly, a thin surfactant layer is introduced between the particles and the glass substrate, acting as an optothermal gate to modify particle-substrate interfacial interactions. With the optical

heating of the particles, the friction of the particle and surfactant is dramatically reduced due to the phase transition of the surfactant layer, which allows the manipulation of particles with optical scattering forces.[120, 121] We term our technique optothermally-gated photon nudging (OPN). OPN is capable of dynamic manipulation and reconfigurable patterning of colloidal particles with a wide range of materials, sizes, and shapes on solid substrates. In combination with in situ dark-field optical imaging and spectroscopy (Figure 3.1a), we can visualize the manipulation process for real-time feedback and measure the properties of the particles and their interactions in assemblies.

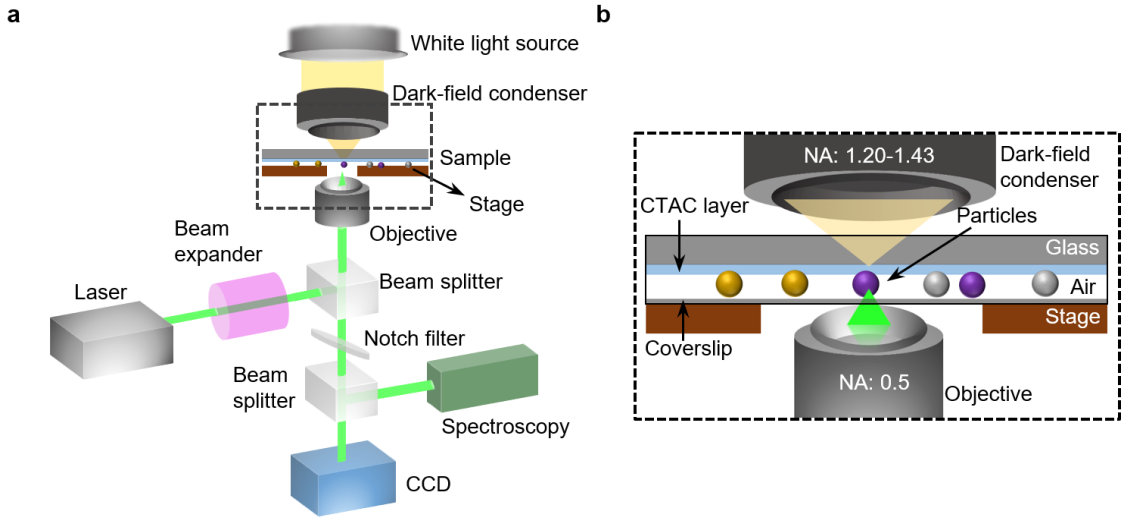

Figure 3.1: Schematic illustration of energy confinement in the polymer network of hydrogels. (a) Diffused heat around penetrated solar absorbers in the molecular mesh of the polymer network. (b) Concentrated heat around solar absorbing NPs surrounded by the polymer network.

A thin layer of CTAC solid layer is deposited between the glass substrate and the randomly-dispersed colloidal particles to enable OPN (Figure 3.1b). It should be noted that the CTAC can be substituted with any other surfactant or polymer with similar photothermal responses, such as poly(methyl methacrylate). The general concept of OPN

is illustrated in Figure 3.2a. The deposited CTAC acts as an optothermal gate to modulate the particle-substrate interface and allow for the manipulation of particles, which is pivotal for OPN. Without optical heating, CTAC forms a thin solid film,[122] and particles adhere onto the film with van der Waals forces (Figure 3.2b). To release the bond between the film and the particle, we directed a laser beam onto the particle, whose optothermal effects generate an abundance of heat. The maximum temperature reached over 600 K when a 200 nm AuNP was irradiated by a 532 nm laser beam at an optical power of 1 mW (Figure 3.2d). In addition, the temperature of the CTAC layer under the AuNP exceeded ~450 K, which is larger than the first-order phase transition temperature of CTAC at 350-370 K.[122] Under such high temperatures, CTAC surrounding the particle undergoes a localized order-disorder transition and turns into a "quasi-liquid" phase (Figure 3.2c), where the nonpolar layers are melted while the ionic layers remain practically intact.[122, 123] This disordered structure significantly eliminates the van der Waals friction between the particle and CTAC layer, opening the optothermal gate for free particle motion. With the optothermal gate open, particles can be nudged and guided smoothly by the laser beam with optical scattering forces (Figure 3.2e). Through steering the laser beam or translating the substrate with a motorized stage, particles can be manipulated to any target position. We first present the use of OPN to manipulate AuNPs as a proof-of-concept demonstration. AuNPs were tracked with in situ dark-field optical imaging due to their strong light scattering properties. Figure 3.2f shows the real-time manipulation of a 300 nm AuNP using a 532 nm laser. The power intensity we used was 0.2-2 mW/μm^2, which is 1-2 orders of magnitude lower than the typical power intensity in optical tweezers (10-100 mW/μm^2). The AuNP was delivered in-plane over a distance of ~8 μm in 35 s.

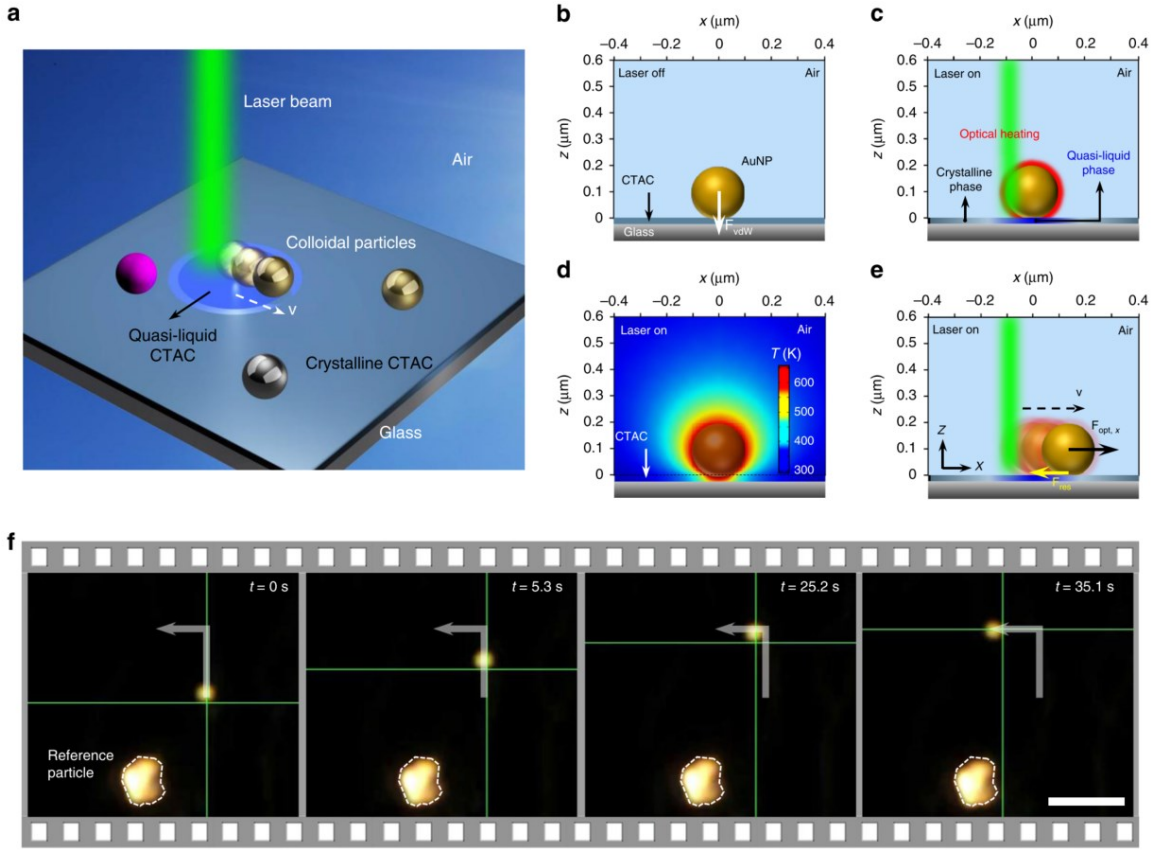

Figure 3.2: General concept of OPN. (a) Schematic illustration of OPN on a solid substrate. (b) A 200 nm AuNP placed on and bonded with the CTAC layer by van der Waals force F_{vdW} without optical heating. (c) The optical heating under laser illumination induces a localized phase transition in the surrounding CTAC layer. CTAC turns into a quasi-liquid phase and releases the bond with AuNP. (d) The simulated temperature distribution around a 200 nm AuNP. Incident power: 1 mW; laser beam size: 0.8 μm. (e) AuNP moves against the laser beam with an in-plane optical force $F_{opt,\,x}$ and a resistant force F_{res}. In (a-e), the schematic configuration is flipped upside down for better visualization. (f) Sequential dark-field optical images showing real-time manipulation of a 300 nm AuNP. The green crosshair indicates the position of the laser beam. The white arrow depicts the path. Scale bar: 5 μm.

Apart from AuNPs, we also demonstrated the nanomanipulation of other materials using OPN, such as silver nanoparticles (AgNPs) and silicon nanoparticles (SiNPs).

Particles with a wide range of diameters from 40 nm to several micrometers can be manipulated with an average speed of 0.2-2 μm/s. It should be noted that the speed of the OPN manipulation was limited by the manual operation in this scenario. With automatic digital operation and feedback controls, the manipulation speed could be further improved. Interestingly, the CTAC layer remains functional as a vital component of OPN after the particle translation, which allows the particle to be steered back to its original position along the same path.

Next, we discuss the underlying physical mechanisms and analyze the forces involved in the OPN platform in detail. First, we designed and conducted a series of control experiments to understand the role of optical heating and scattering force. To decouple the optical heating and scattering, we applied a thermoplasmonic substrate as the heat source[124]. In addition, we selected PS and titanium dioxide (TiO_2) nanoparticles for the control experiments. Both PS and TiO_2 nanoparticles show negligible optical absorption. In addition, PS nanoparticles show weak scattering at the laser wavelength (532 nm), while TiO2 nanoparticles have a much larger scattering efficiency (Figure 3.3)[125, 126].

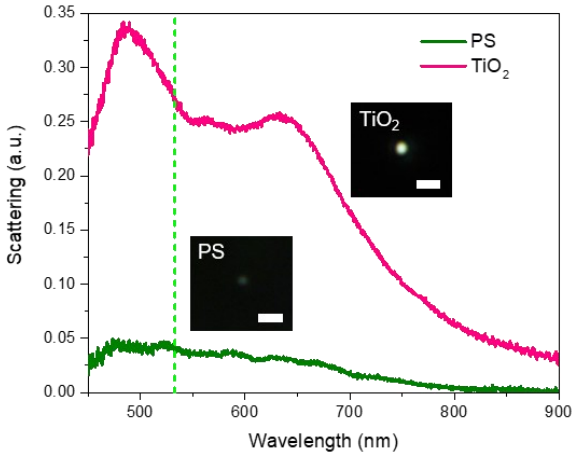

Figure 3.3: Scattering spectra of TiO_2 nanoparticle (pink) and PS (olive) measured at the same incident light intensity. The insets show the corresponding dark-field images, scale bars: 2 μm. The green dashed line indicates the wavelength of the laser (532 nm). Apparently, PS nanoparticles show weak scattering at the laser wavelength, while TiO_2 nanoparticles have a much larger scattering efficiency.

The results of control experiments revealed that OPN simultaneously exploits optical heating to open the optothermal gate and radiation-pressure forces to drive the particles (Table 1). Moreover, the option to introduce an external heat source to trigger the manipulation of particles makes OPN a generalized platform for a wide range of materials that interact strongly with light, such as metal (e.g., aluminum)[127], semiconductor (e.g., germanium and gallium arsenide)[128, 129], and inorganic perovskite (e.g., barium titanate)[130]. We further conducted experiments to exclude the thermal expansion and electrostatic forces as the primary driving forces in OPN.

No.	Particle	Substrate	CTAC?	Optical heating	Optical scattering	OPN works or not?
1	Au/Ag/Si	Glass	No	Strong	Strong	No
2	Au/Ag/Si	Glass	Yes	Strong	Strong	**Yes**
3	PS	Glass	Yes	Weak	Weak	No
4	PS	AuNIs	Yes	Strong	Weak	No
5	TiO_2	Glass	Yes	Weak	Strong	No
6	TiO_2	AuNIs	Yes	Strong	Strong	**Yes**

Table 1: Summary of the control experiments to investigate the role of optical heating and scattering forces in OPN.

Next, we quantitatively analyzed the OPN manipulation by measuring the velocities of 200 nm and 300 nm AuNPs under a directed laser with a fast CCD (Figure 3.4a). The measured particle velocity results from the balance between the optical driving force and the resistant force by surfactant. For example, the measured data for a 300 nm AuNP at an optical power of 1.40 mW is shown in Figure 3.4b. When the laser was on, the AuNP immediately gained speed and moved against the laser beam. Since the laser beam was focused slightly offset from the particle center along the *X*-axis, the AuNP had a much larger shift in *X*-direction than that in the *Y*-direction, which is consistent with our photon nudging hypothesis. As we raised the laser power, the AuNPs increased their speeds and shifted farther from their original positions. For both 200 nm and 300 nm AuNPs, the measured maximum velocities increased when the optical power was raised from 0.27 to 1.40 mW (Figure 3.4c). This relationship is reasonable, considering that the optical force scales linearly with the laser power, which further confirms the optical force is the primary driving force in OPN.

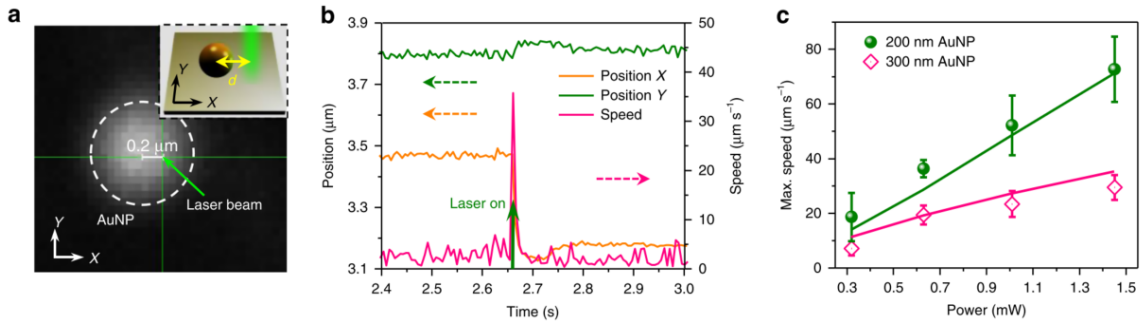

Figure 3.4: Characterization of the OPN manipulation process. (a) Optical image and (inset) the schematic illustration showing the measurement of particle velocities. The distance between the center of the laser beam and the center of the particle was set to 200 nm for all measurements. (b) The measured *X* position, *Y* position, and speed *v* of a 300 nm AuNP under the laser irradiation of 1.40 mW as a function of time *t*. The solid green arrow at *t* = ~2.7 s indicates the instant when the laser is turned on. (c) The measured maximum speed of 200 nm and 300 nm AuNPs as a function of incident power. The solid lines show the corresponding modeled data.

Furthermore, we adopted a simplified physical model to understand the nanomanipulation process. Since the particles were manipulated in the *X*-*Y* plane, only the in-plane optical and resistant forces needed to be considered. We applied the finite-difference time-domain (FDTD) method to calculate the optical scattering forces in the *X*-direction with varying distances between AuNPs and the laser beam. It should be noted that for both *X*- and *Y*- polarization, the laser beam will always repel the AuNP, which allows OPN to maneuver particles in all directions without the need to control the laser polarization. In our case, the particles are partially immersed into the CTAC film, for which the resistant force can be evaluated according to[131]:

$$\boldsymbol{F}_{res} = 6\pi\eta R f_d \boldsymbol{v} \tag{8}$$

where η is the viscosity of CTAC in its "quasi-liquid" phase, R is the particle radius, $\boldsymbol{v}$ is the velocity of the particle, and f_d is a dimensionless drag coefficient which is dependent on the viscosity of the fluids[132]. The trajectory of the AuNP can be modeled with:

$$m\ddot{\boldsymbol{x}} = \boldsymbol{F}_{res}(\boldsymbol{v}) + \boldsymbol{F}_{opt}(\boldsymbol{x}) \tag{9}$$

where m is the mass of the particle, $\boldsymbol{x}$ is the position of the particle, and $\boldsymbol{F}_{opt}(\boldsymbol{x})$ is the total optical forces calculated by the FDTD. We applied MATLAB to numerically solve the motion of particles in OPN with the same time step as the fast CCD. The calculated maximum velocity values for 200 nm and 300 nm AuNPs under different laser powers are shown in Figure 3.4c. The results match very well with our measurements, which further confirms our proposed mechanisms.

We further characterize the manipulation efficiency by analyzing the video recordings of the particle movement. During the manipulation process, the trajectories of the particles and the laser beam almost overlap (Figure 3.5b), which shows that the particles can be efficiently manipulated along the laser direction. To quantify the manipulation efficiency, we examined the difference between the laser movement vector $\boldsymbol{E}_{\mathrm{l}}$ and the particle movement vector $\boldsymbol{E}_{\mathrm{p}}$, as sketched in Figure 3.5a. The accuracy of the particle movement can be characterized by the dot product of unit vectors of $\boldsymbol{E}_{\mathrm{l}}$ and $\boldsymbol{E}_{\mathrm{p}}$. We define a manipulation efficiency Q as the average $\cos\theta$ over a full manipulation trajectory:

$$Q = <\cos\theta> = <\frac{\boldsymbol{E}_{\mathrm{l}} \cdot \boldsymbol{E}_{\mathrm{p}}}{|\boldsymbol{E}_{\mathrm{l}}||\boldsymbol{E}_{\mathrm{p}}|}> \tag{10}$$

where θ is the angle between $\boldsymbol{E}_{\mathrm{l}}$ and $\boldsymbol{E}_{\mathrm{p}}$. The calculated Q ranges from ~0.6-0.8 for the recorded videos, indicating high-efficient manipulation of all kinds of colloidal particles.

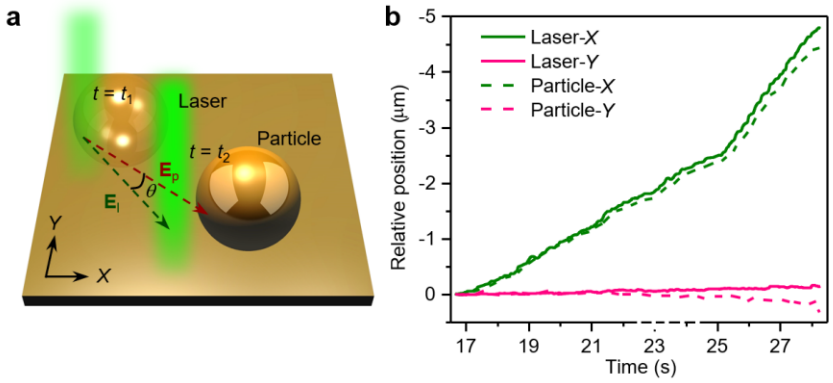

Figure 3.5: (a) Schematic of the comparison of the laser movement vector $\boldsymbol{E}_l$ and the particle movement vector $\boldsymbol{E}_p$ at two successive frames ($t = t_1, t_2$). θ is denoted as the angle between $\boldsymbol{E}_l$ and $\boldsymbol{E}_p$. (b) Examples of the recorded trajectories of the laser beam and the particle during the manipulation.

To assess OPN as a nanomanufacturing tool for arbitrary and precise construction of colloidal structures, we explored the patterning accuracy of OPN in both 1D and 2D cases. As a preliminary demonstration, we used OPN to assemble seven randomly dispersed SiNPs with a diameter of 500 nm into a straight line (Figure 3.6a,b). The dark-field image shows a well-arranged particle chain after the patterning procedure (Figure 3.6c). Furthermore, we took the SEM image of the particle assembly to precisely determine their positions and their deviations from the target line (Figure 3.6d). The position error, the distance between the particle center and the line (inset in Figure 3.6d), was analyzed for individual SiNPs and plotted in Figure 3.6e. A position accuracy of ~80 nm was achieved, as indicated by the shaded area.

In the second example, we manipulated nine SiNPs using OPN to assemble a 3×3 2D array (Figure 3.6f). The optical image and corresponding SEM image of the SiNP array are shown in Figure 3.6g,h. Similar to the 1D case, we evaluated the position error in both the *X* and *Y* directions from the SEM image (Figure 3.6i). As depicted in Figure 3.6j, all

manipulated particles are located close to their target positions with an average deviation of ~200 nm, which is less than half the diameter of the SiNPs. The ability to achieve colloidal patterning at nanoscale accuracy enables OPN to be used for the precise fabrication of nanostructures with colloidal particles. It should be noted that the current position accuracy is primarily limited by the diffraction barrier in optical microscopy. Additionally, during the manipulation experiments, we only relied on our naked eyes to estimate the positions of the nanoparticles in the optical images. Thus, we envision that the particle-patterning accuracy can be further improved with advanced imaging, analysis, and tracking of particles with higher precision. For instance, we have achieved an improved position accuracy of ~20 nm by using imaging software to define a target line along which the particles will be aligned.

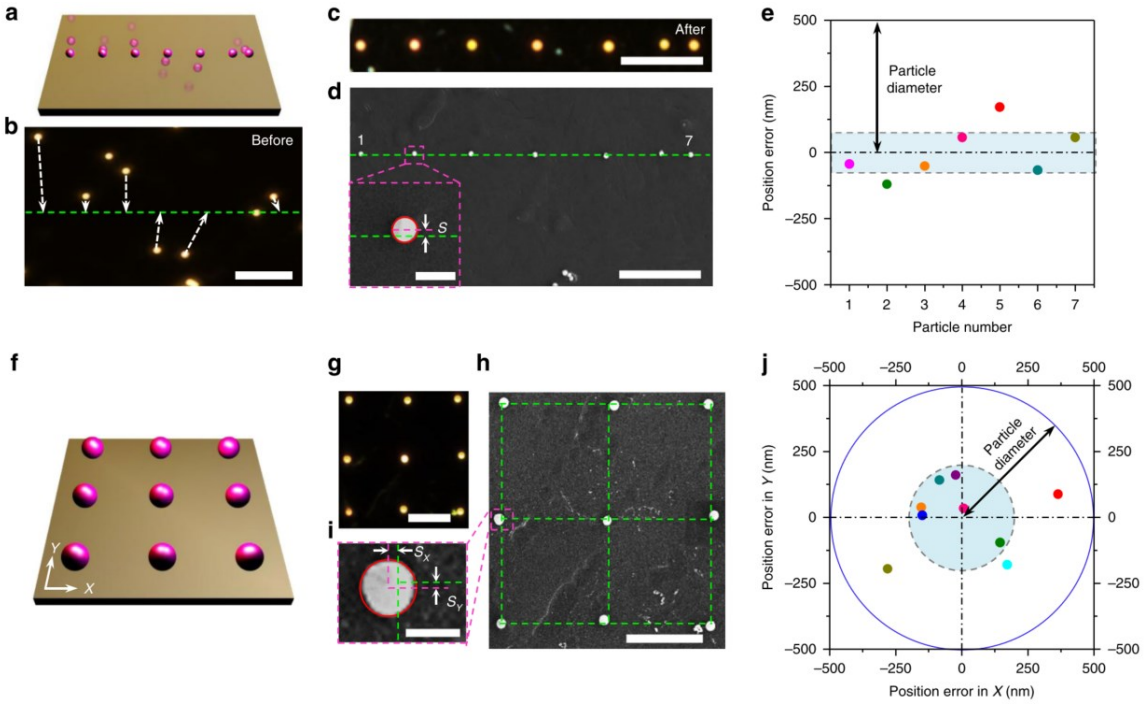

Figure 3.6: Patterning accuracy of OPN. (a) Schematic illustration of the 1D assembly of seven 500 nm SiNPs. (b) Dark-field image of SiNPs before patterning. The white dashed arrows indicate the target positions of each SiNPs. (c) Optical image of SiNPs after 1D assembly. (d) SEM image of SiNPs after 1D assembly. The inset defines the method to determine the position error *S* for individual SiNPs. (e) Position errors for each SiNPs in the line. The shaded area shows the average deviation from the target line, which is ~80 nm. (f) Schematic illustration and (g) dark-field image of a 2D assembly of nine 500 nm SiNPs into a 3 × 3 array. (h) SEM image of the 2D assembly. (i) The position error in *X* (S_X)and *Y* (S_Y) for individual SiNPs. (j) Position errors in *X* and *Y* for each SiNPs in the 2D array. The shaded area indicates the average deviation from the target positions, which is ~200 nm. Scale bars: (b-d) 10 μm; inset in (d)1 μm; (g, h) 5 μm; (i) 500 nm.

Since the nanomanipulation is performed on a solid substrate, OPN allows for the dynamic transportation of particles to new sites, enabling the active assembly of colloidal structures. Reconfigurable patterning of four 300 nm AuNPs is shown in Figure 3.7a. The randomly dispersed AuNPs were first assembled into an L-shaped structure. By moving

the particle on the top down to the right side, we transformed the L-shaped pattern into a square. Then, the particle at the upper left corner of the square was translated to the top right, forming a mirrored L-shaped pattern. Finally, four AuNPs were assembled into a straight line by delivering the particle on the left to the bottom.

Apart from colloidal particles, we also achieved dynamic manipulation of metallic nanowires through OPN. Gold nanowires (AuNWs) with a diameter of 160 nm and a length of 3 μm were used in this experiment. Since gold has high thermal conductivity, the CTAC optothermal gate can be triggered with the laser beam directed at any location along the AuNWs. By focusing the laser at one end of the nanowire while steadily moving the laser tangentially, the nanowire can be rotated about the opposite end, like a nano-hinge. A single AuNW can be rotated over ~180 degrees in a counterclockwise direction within 32 s (Figure 3.7b). AuNW translation is also possible by directing the laser at the center of the nanowire, which allows us to transport a AuNW with a fixed orientation. As a demonstration, we transported a AuNW translationally over a distance of ~5 μm within 23 s (Figure 3.7c).

Furthermore, we were able to achieve the reconfigurable patterning of hybrid nanostructures comprised of a metallic nanowire and dielectric nanoparticles. Two SiNPs and one AuNW were first patterned into a "Y"-shaped structure. By rotating the AuNW and by moving SiNPs to new sites, we deliberately transformed the structure into a "Z"-shaped pattern (Figure 3.7d). The ability to dynamically manipulate nanowires and metal-dielectric nanostructures shows the potential of OPN for the assembly of functional components and devices. It is worth noting that OPN can also be applied to manipulate other anisotropic nanoobjects, such as gold nanorods and gold nanotriangles.[133]

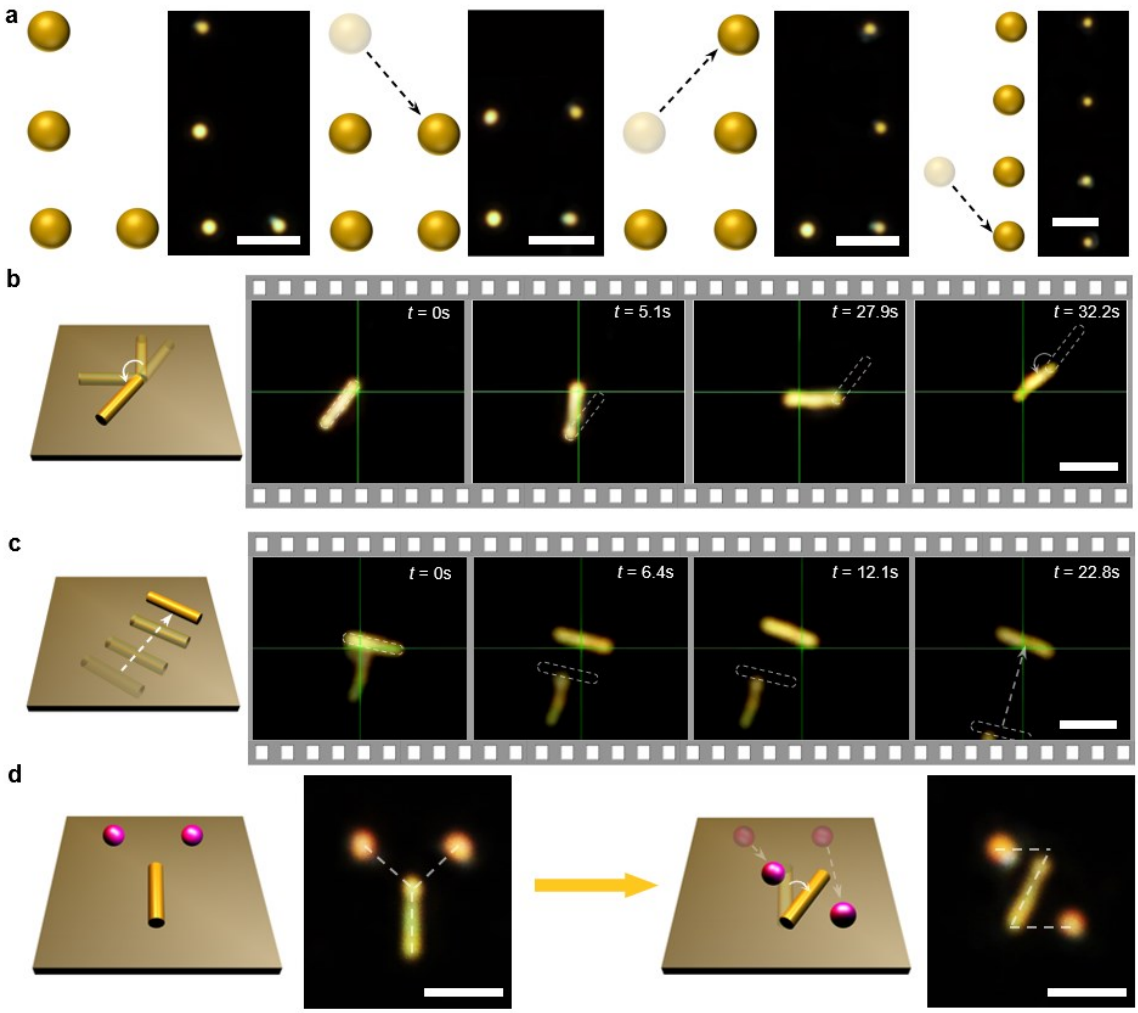

Figure 3.7: Reconfigurable patterning of particles and nanowires. (a) Reconfigurable patterning of four 300 nm AuNPs. Four particles were arranged into L-shape, a square, mirrored L-shape, and a straight line sequentially. The dashed arrows show the reconfigurable patterning sequence. (b, c) Schematic illustrations and successive optical images showing the real-time (b)rotation and (c) translation of AuNWs. The green crosshairs mark the positions of the laser beam. The dashed rectangular outline indicates the original positions of nanowires. (d) Schematic illustration and optical images showing reconfigurable patterning of metal-dielectric hybrid nanostructures. Two 500nm SiNPs and one AuNW were patterned into “Y” and “Z”, sequentially. Scale bars: (a) 5 μm; (b-d) 3 μm.

We further apply in situ spectroscopy to study the spectral response of colloidal nanostructures. The minimal backward scattering from the CTAC layer permits the detection of the intrinsic scattering spectra from the particles. The in situ optical spectroscopy is capable of distinguishing colloidal particles with different sizes by comparing their scattering peak positions during the manipulation process (Figure 3.8).

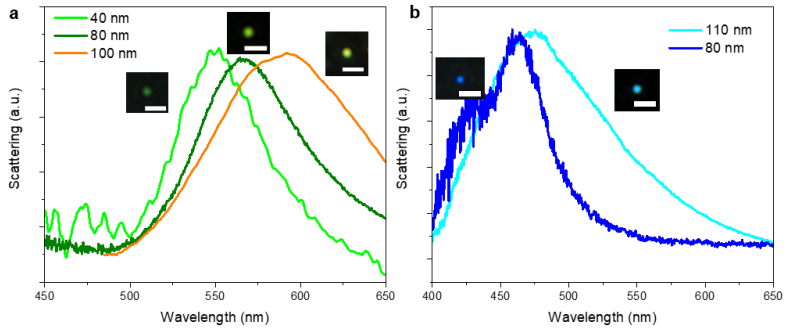

Figure 3.8: In situ Scattering spectra of AuNPs and AgNPs. (a) Scattering spectra of (green) 40 nm, (olive) 80 nm, and (orange) 100 nm AuNPs. (b) Scattering spectrum of (blue) 80 nm and (cyan)110 nm AgNPs. The insets show the corresponding dark-field images. All scale bars are 2 μm.

We first measured the scattering spectra of a 100 nm AuNP before and after the manipulation to confirm that OPN can manipulate nanoparticles without damaging their optical properties (Figure 3.9). This non-invasive operation is highly desired and advantageous in the fabrication of functional components and devices such as reconfigurable optical nanocircuits and active plasmonic waveguides

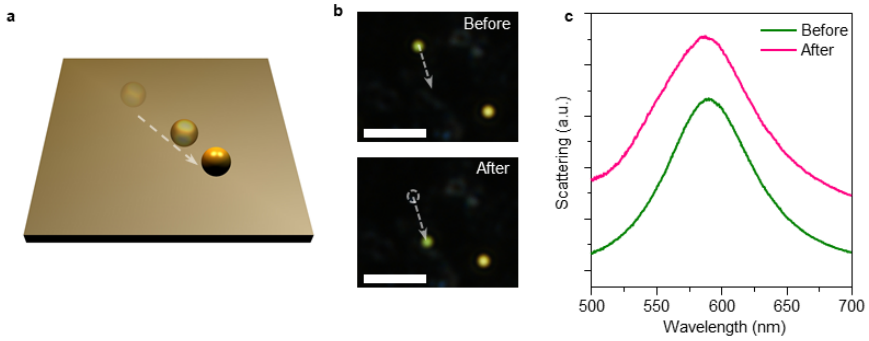

Figure 3.9: (a) Schematic illustration of the AuNP manipulation process. (b) Dark-field images and (c) scattering spectra of the AuNP before and after OPN manipulation. Scale bars: 5 μm. The scattering spectra showed no apparent differences after the OPN manipulation, which indicates OPN can manipulate nanoparticles without damaging their optical properties.

We further showed that the CTAC layer could be readily removed without destroying the existing particle patterns by simply soaking the sample in water or isopropyl alcohol (IPA) for ~2 minutes. As shown in Figure 3.10a,b, the positions of the colloidal particles remained the same after the removal of CTAC. Meanwhile, the measured scattering peak of 100 nm AuNPs showed an obvious blueshift from ~580 nm to ~545 nm (Figure 3.10c). This blueshift revealed a refractive index change in the particle surrounding, which confirmed the successful removal of CTAC (the refractive index of CTAC is 1.38). The ability to remove CTAC after OPN manipulation can avoid any undesirable effects of CTAC in some applications of the patterned particles, including chemical and biological sensing.

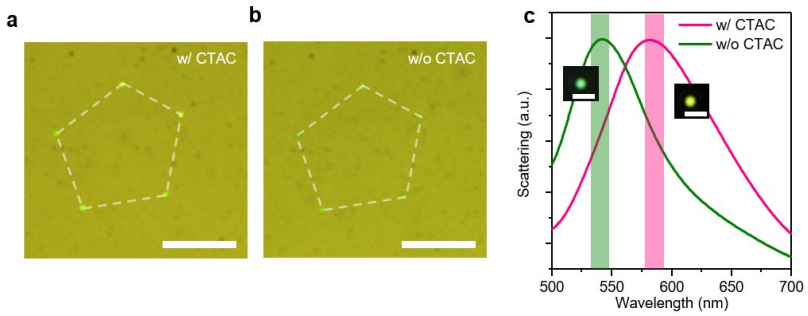

Figure 3.10: (a, b) Optical images of a pentagon pattern composed of five 100 nm AuNPs (a) before and (b) after the removal of CTAC. Two identical white dashed pentagons are added to help indicate the positions of AuNPs. (c) The scattering spectra of 100 nm AuNPs measured before and after the removal of CTAC. The shaded area indicates the standard deviation of the peak position. The insets show the corresponding dark-field images. Scale bars: (a, b) 10 μm; inset in (c) 2 μm.

Furthermore, we explored OPN's potential to assemble and characterize colloidal structures with near-field coupling. One 100 nm AuNP was delivered to the vicinity of the other 100 nm AuNP by OPN, as depicted in Figure 3.11a,b. The assembled structure was confirmed by the SEM image, from which a clear dimer with a gap of ~ 15 nm can be observed (Figure 3.11c). Before assembly, the single AuNPs showed a localized surface plasmon (LSP) peak at ~ 588 nm (Figure 3.11d). The small difference in the LSP peaks of these two AuNPs resulted from the slight variations in the particle sizes (Figure 3.11c). The single scattering peak split into two peaks at ~ 550 nm and ~ 614 nm (Figure 3.11f), which unequivocally revealed the near-field coupling between two AuNPs. We simulated the scattering spectra and electric field enhancement profiles of a single 100 nm AuNP and a 100 nm AuNP dimer with a gap of 15 nm (Figure 3.11e,g). The AuNP dimer exhibited a longitudinal mode at ~618 nm and a transverse mode at ~553 nm, which signify a redshift and a blueshift, respectively, contrasting from the original mode at ~590 nm for the single 100 nm AuNP.[134] The simulation results matched well with the experimental spectra.

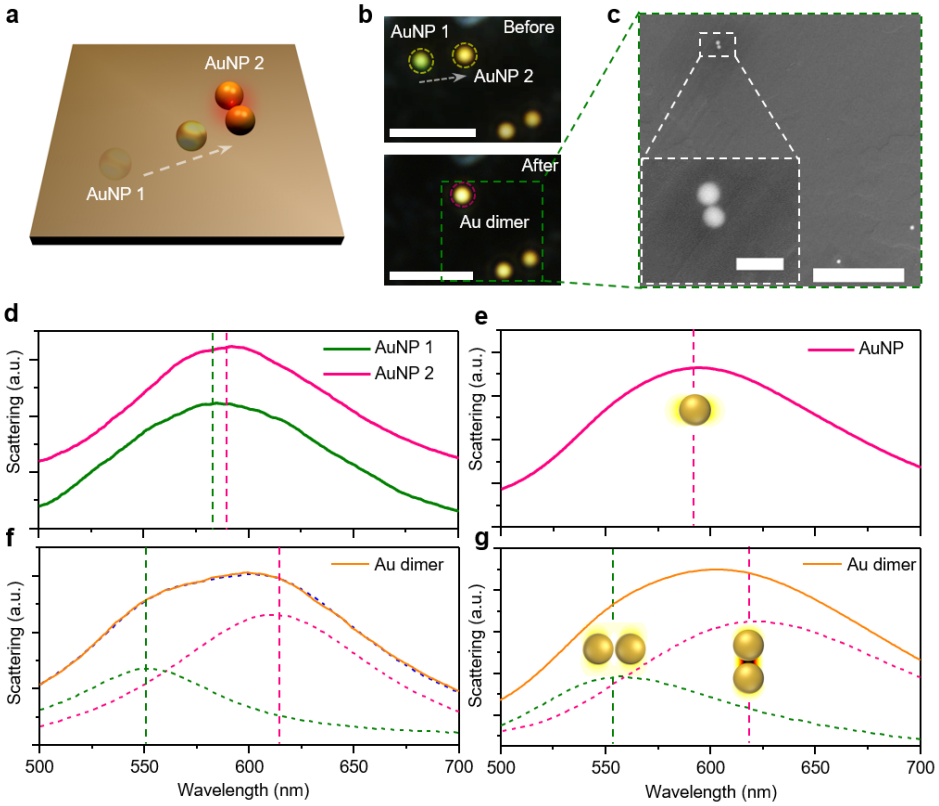

Figure 3.11: In situ optical spectroscopy. (a) Schematic illustration of the assembly of Au dimer with two 100 nm AuNPs. (b) Dark-field images of the AuNP before and after the dimer assembly. (c) SEM image of the Au dimer. (d) Scattering spectra of the two AuNPs before assembly. (e) The simulated scattering spectra of a 100 nm AuNP. (f) Scattering spectra of the Au dimer. The pink and olive dashed curves represent the longitudinal and transverse plasmon modes, respectively. (g) The simulated scattering spectrum of the AuNP dimer. The insets in (e, g) show the corresponding electric field enhancement profiles. Scale bars: (b) 5 μm; (c) 2 μm; inset in (f) 200 nm.

It is worth noting that, although the subwavelength interparticle gap cannot be distinguished in optical images due to the diffraction limit, OPN can reliably fabricate Au dimers with any desired gap by taking advantage of the in situ optical spectroscopy. For example, we assembled two 100 nm AuNPs into a Au dimer. Figure 3.12a,b show the dark-field optical images of the Au dimer composed of the same two 100 nm AuNPs with

different interparticle distances. It is challenging to distinguish the gap between these two AuNPs based on the optical images. However, taking advantage of our in situ optical spectroscopy, one can easily obtain the scattering spectra of the Au dimers. As shown in Figure 3.12e, the scattering spectrum of the dimer in Figure 3.12a shows a single peak at ~585 nm, which is consistent with that of single AuNPs (Figure 3.12d). The spectrum can also be well-fitted by a single-peak Lorentz function. The result reveals that there is no near-field coupling between two AuNPs, which indicates two AuNPs are separated by a large distance. In contrast, the dimer in Figure 3.12b shows two split peaks at ~575 nm and ~635 nm (Figure 3.12e), which demonstrate the near-field coupling behavior between these two AuNPs. The SEM image further confirmed a Au dimer with a gap of ~ 15 nm (Figure 3.12c).

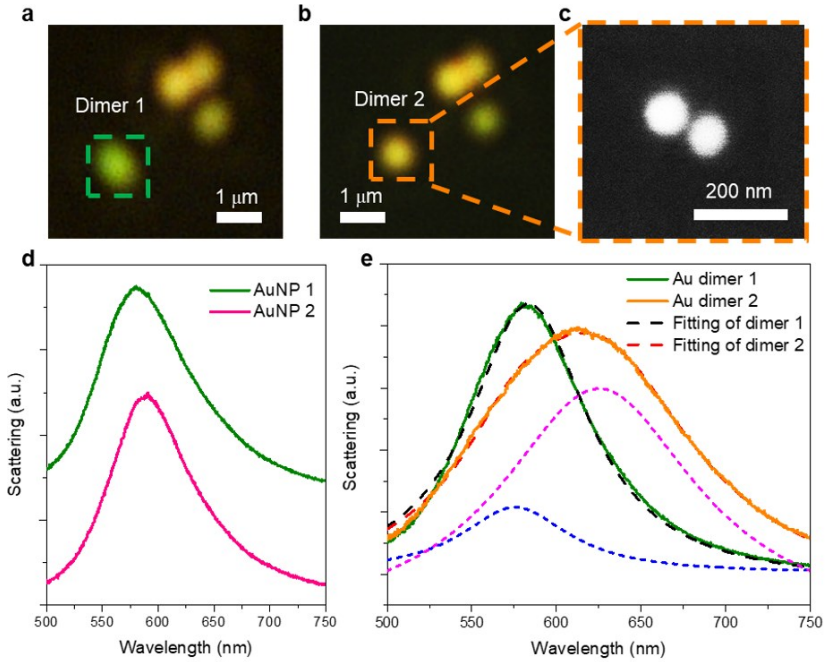

Figure 3.12: Reliable fabrication of Au dimer with a gap of ~15 nm. (a,b) Optical images of two Au dimers composed of the same 100 nm AuNPs with different interparticle distances. (c) The SEM images of the Au dimer in (b). (d) The scattering spectra of the two single AuNPs. (e) Scattering spectra and the fitting of the Au dimers in (a) and (b).

The ability to control the near-field coupling of nanoparticles allows us to fabricate functional colloidal devices for a variety of nanophotonic applications, such as chiral metamolecules.[135] With simultaneous reconfigurable nanofabrication on a solid substrate and in situ optical characterizations, OPN will provide a powerful platform to design active optical devices and study the coupling between colloidal structures. Furthermore, OPN can be applied in a vacuum or an inert gas environment to assemble water-soluble and air-unstable nanoparticles (e.g., halide perovskite nanoparticles[136, 137]) and explore the light-matter interactions in combination with other vacuum-based analytical tools, such as scanning transmission electron microscopy and cathodoluminescence spectroscopy.

In summary, through coordinating optical heating and radiation-pressure forces, we developed an OPN technique for nanomanipulation and patterning of colloidal particles and nanowires on a solid substrate. OPN represents a milestone in pushing the working conditions of optical tweezers from fluidic to solid phases. As a general solid-phase optical technique, OPN is applicable to a wide range of metal, semiconductor, metal oxide and dielectric nanoparticles with varying sizes and shapes. By improved heat management and proper choice of working wavelengths, OPN is readily extended to manipulate many other particles that exhibit strong ultraviolet or near-infrared responses, such as aluminum nanoparticles[127] and titanium nitride nanoparticles.[138]

Future efforts can be made to further enhance the strengths of the solid-phase optical manipulation technique. One can optimize the optics to achieve a more efficient operation. For instance, the oblique incidence of the laser can take advantage of photon momentum along the direction of beam propagation, which could enhance both amplitude and directional control of the driving forces. While OPN offers the opportunity to manipulate colloids at the single-particle resolution, it suffers from relatively low patterning throughput, which is primarily limited by its serial and manual control. The

implementation of a light spatial modulator with a digital feedback control will open up the possibilities for automatic and parallel manipulation to significantly boost the production output.

Along with the development of solid-phase optical manipulation, we have advanced the fundamental understanding and dynamic control of particle-substrate and light-particle interactions. With the in situ optical spectroscopy, OPN holds the potential to dynamically assemble colloidal matters and to explore the mechanical, electronic, and optical couplings between colloidal particles at the nanoscale. With its simple optics, non-invasive operation and versatile capabilities of colloidal assembly, OPN will find a wide range of applications in nanophotonics, nanoelectronics, materials science, and colloidal sciences.

3.2 SOLID-PHASE OPTO-THERMOCAPILLARY NANOMOTORS**

Motors that can convert different forms of energy into mechanical work are of profound importance to the development of human societies. The evolution of micromotors has stimulated remarkable advances in drug delivery and microrobotics, paving the way for futuristic applications in biomedical engineering and nanotechnology. However, further miniaturization of motors towards nanoscale is still challenging due to the strong Brownian motion of nanomotors in liquid environments. In this section, a new type of light-driven nanomotors is developed, termed solid-phase opto-thermocapillary nanomotors, to achieve solid-phase operation without the interference of Brownian motion.

** This chapter is reproduced from following manuscript:
J. Li, P. S. Kollipara, Y. Liu, K. Yao, Y. Liu, Y. Zheng. Solid-Phase Opto-Thermocapillary Nanomotors. *Submitted.*
J. Li is the first author of this manuscript.

Micromotors have attracted tremendous interest due to their promising applications in microrobotics,[139, 140] nanofabrication,[141, 142] and biomedical engineering.[143-146] Micromotors can be driven by chemical reactions [147, 148] and external stimuli, including electric,[149, 150] magnetic,[151, 152] light,[121, 153-155] and acoustic fields.[156, 157] Among them, light is regarded as an attractive stimulus for on-demand control of micromotors in a reversible and remote manner with excellent temporal and spatial resolution. For instance, photocatalytic reactions, which occur at the surface of a particle, can power asymmetric micromotors through self-diffusiophoresis,[158, 159] self-electrophoresis,[155, 160] and bubble propulsion.[161, 162] In addition, optical forces and torques are widely exploited to drive micromotors. The spin angular momentum or orbital angular momentum carried by circularly polarized light or structured light can induce an optical torque to drive rotary micromotors.[163-166] The optical torque can also stem from the asymmetric scattering of exotically shaped nanostructures with linearly polarized light.[167] In addition, Recently, optothermal micromotors have also been realized via laser-heating-induced thermophoresis,[168, 169] thermoelectricity,[170] and demixing of critical mixtures.[171]

Despite the tremendous progress in light-driven micromotors, the miniaturization of motors toward the nanoscale, especially with all dimensions below 100 nm, remains challenging. Molecular machines have been proposed to control mechanical forces and motions at the molecular scale.[172] However, the strong reliance on molecular chemistry, the extremely localized motion, and the difficulty of real-time monitoring and control limit the broader applications of molecular machines in solid-state devices. To overcome these limitations, nanomotors ranging from 10 nm to 100 nm are essential in bridging the gap between micromotors and molecular motors. However, at such a small scale, random Brownian motion becomes dominant in the liquid environments, hindering the precise control of the motion of nanomotors.[140, 173]

Herein, we develop a solid-phase opto-thermocapillary nanomotor (sOTNM) that is free from the interference of Brownian motion. sOTNM is operated on a solid substrate at ambient conditions, which is enabled by the rationally designed optical modulation of particle-substrate interactions. A thermally responsive layer of solid CTAC is sandwiched between the glass substrate and AuNPs as the nanomotors. When the laser is on, optical heating of the AuNP leads to a localized phase transition of CTAC from a crystalline structure to a quasi-liquid phase,[174] which generates the thermocapillary stress at the AuNP-CTAC interface to enable the rotary motion (Figure 3.13a). Figure 3.13b shows the real-time rotation of an 80 nm AuNP under a 660 nm laser excitation. The AuNP rotates stably in a circular orbit around the laser beam (Figure 3.13c), as further indicated by the sinusoidal curve fitting of the laser-particle displacement along the *X* and *Y* axes (Figure 3.13d).

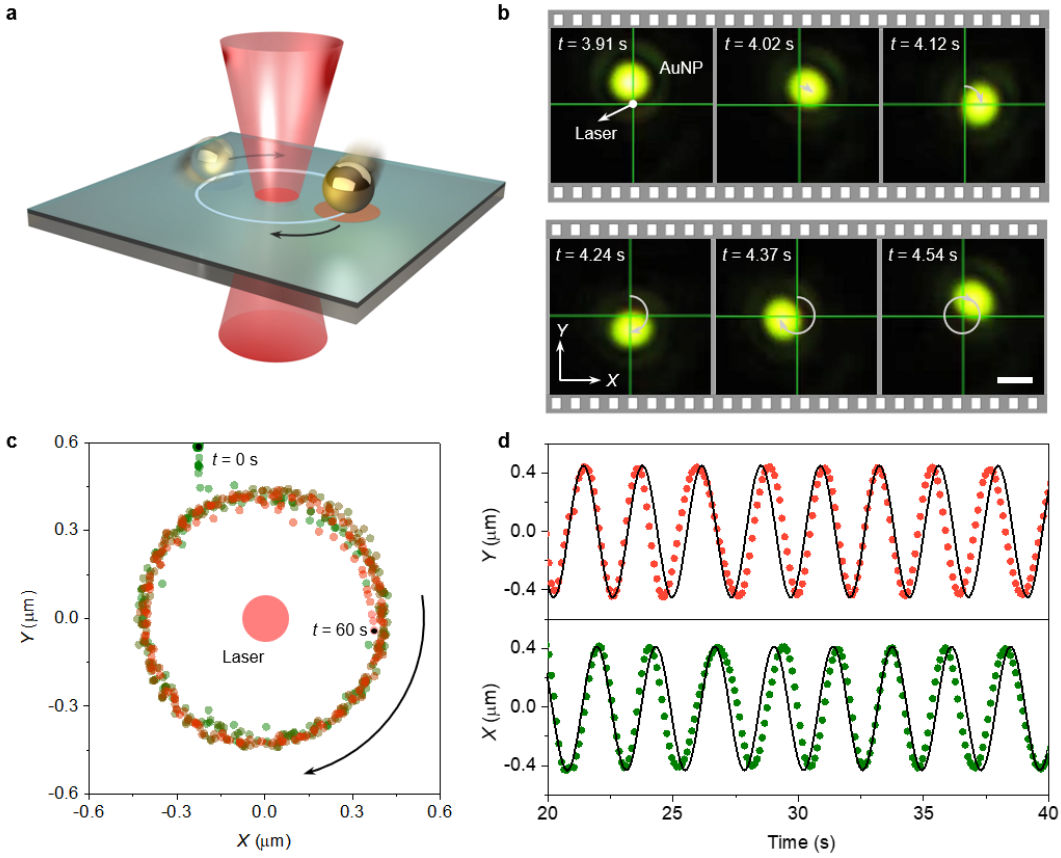

Figure 3.13: General concept of sOTNM. (a) Schematic of sOTNM on a solid substrate. (b) Time-resolved dark-field optical images showing the orbital rotation of an 80 nm AuNP. Laser power: 6 mW. Scale bar: 1 μm. (c, d) Centroid tracking (c) and displacement (d) of the rotating AuNP in (b). The origin of the coordinates is at the center of the laser beam. The curved arrows in (a-c) indicate the rotation direction of the nanomotor. The solid lines in (d) correspond to the sinusoidal fitting curves.

To understand the working mechanisms of sOTNM, we analyzed the in-plane forces in both radial and tangential directions. We first took the scanning transmission electron microscope (STEM) images of the 80 nm Au-nanomotors to gain the geometrical information (Figure 3.14). The AuNPs were not in a perfectly spherical shape, and multi-faceted asymmetry could be clearly observed. This asymmetry is essential in the origin of

driving forces for the nanomotors, which will be discussed in detail in the following contents.

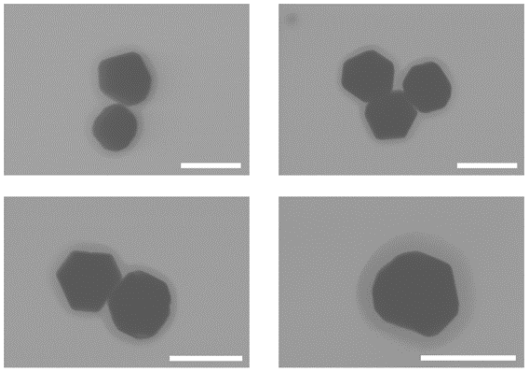

Figure 3.14: STEM images of 80 nm AuNPs. None of the AuNPs is in a perfect spherical shape, and multi-faceted asymmetry can be clearly observed. Scale bars: 100 nm.

To better understand the role of asymmetry, we developed a new 3D reconstruction method to build asymmetric AuNPs from STEM images and implemented the 3D asymmetric models in numerical simulations. Instead of retrieving the geometry of an individual nanoparticle, this approach enables the construction of multiple morphologies to resemble a batch of nanoparticles. Two random STEM images are selected from the pool of high-resolution STEM images to form the top-view and side-view of the nanoparticle to reconstruct a 3D AuNP (Figure 3.15a). Both images are converted into binary images. Several points on the image are chosen to define the boundary of the edges. During this process, a higher density of points on the boundary of particle corners are identified to avoid sharp edges in the 3D particle so that abrupt changes in optical forces or plasmonic hotspots in simulations are not visualized. Then, 2D images are converted into 3D coordinates by integrating the (x,y) coordinates (Cartesian coordinates) from top-view

Particle A and (r, z) coordinates (cylindrical coordinates) from side-view Particle B. Specifically, at $z_0 = 0$, the boundary of the 3D particle (x-y plane) is set as the coordinates of the edge of Particle A. At a certain height z (with a step of 2 nm), the boundary in the x-y plane is determined by scaling the edge of Particle A by a factor of r/r_0, where r is the coordinate from the edge of Particle B at z and r_0 is the radius of the fitted circle from the edge of Particle B (r_0 is close to 40 nm in our experiments). The final 3D AuNP is reconstructed based on these coordinates of the 3D edges (Figure 3.15b,c). The data points are converted into a smooth surface (an STL file) using Solidworks and imported into COMSOL and FDTD for simulations. To consider the statistical variations in particle geometry, we generated multiple 3D nanoparticles for the force simulation.

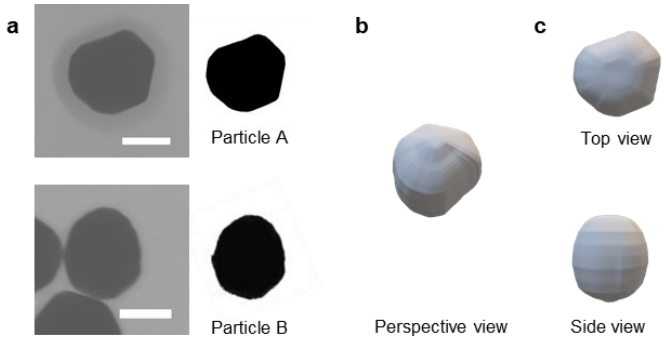

Figure 3.15: 3D reconstruction of an asymmetric AuNP based on two STEM images. (a) Two STEM images of two different particles form the top view (Particle A) and side view (Particle B) of the 3D asymmetric AuNP. Scale bars: 50 nm. (b) The perspective view of the 3D reconstructed AuNP. (c) Top and side view of the 3D reconstructed AuNP..

We then simulated the optical forces exerted on the AuNP using a FDTD method. The tangential component of the in-plane optical force arising from the geometric asymmetry is too small to drive the rotation. Here, we ascribe the driving force of sOTNM to the thermocapillary forces. In brief, under laser excitation, a temperature gradient along

the interface between the AuNP and localized quasi-liquid CTAC results in an interfacial surface tension gradient, which generates localized non-zero thermocapillary stress at the AuNP-CTAC interface and a net thermocapillary force on the AuNP.[175] For a perfectly spherical AuNP, this thermocapillary force vanishes due to the uniform temperature along the surface of the particle. In contrast, with an asymmetric geometry, the non-uniform temperature at the edges of the multi-faceted AuNP leads to localized non-zero temperature gradients tangential to the surface (Figure 3.16a). The direction of the temperature gradient depends strongly on the surface asymmetry of the AuNP. Therefore, the direction of the asymmetry-induced thermocapillary forces is mainly dependent on the orientation of the AuNP, whereas the magnitude depends on both the orientation of the particle and the laser-particle distance (Figure 3.16b, c).

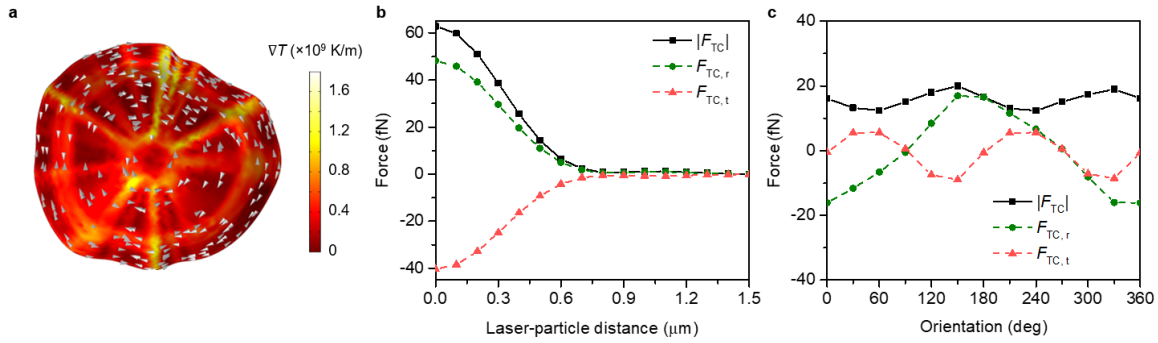

Figure 3.16: Calculated thermocapillary force on an 80 nm AuNP. (a) Simulated temperature gradient mapping (bottom view) on the surface of the AuNP under 660 nm laser irradiation (10 mW). The arrows indicate the in-plane temperature gradient parallel to the surface. (b, c) Radial thermocapillary force ($F_{TC,r}$), tangential thermocapillary force ($F_{TC,t}$), and the magnitude of total thermocapillary force ($|F_{TC}|$) as a function of (b) laser-particle distance and (c) orientation of the AuNP at a laser-particle distance of 400 nm. Laser power: 10 mW.

As shown in the force analysis (Figure 3.17a), sOTNM is enabled by the synergy of optical forces and thermocapillary forces. During the steady rotation, the radial components of optical and thermocapillary forces are balanced as the net centripetal force is orders of magnitude smaller due to the low inertia of AuNPs. The radial optical force on the AuNP is only determined by the radial position, while the radial thermocapillary force also varies with the particle orientation. Thus, the AuNP continuously orients itself with respect to the laser-particle line to maintain a stable orientation throughout the circular rotation. To understand this self-orientation behavior, we calculated the total in-plane torques acting on the AuNP that is responsible for the orientational change. As shown in Figure 3.17b, there are two equilibrium orientations (indicated by the red arrows) where the total torque is zero and restoring torques exist once the orientation changes. It should be noted that only one orientation angle could lead to the stable rotation of the AuNP while the other drives the AuNP away from the orbital track.

Next, we evaluated the total radial and tangential forces exerted on the AuNP at the equilibrium orientation (Figure 3.17c). In the radial direction, the repelling thermocapillary force and the attractive optical force are balanced, leading to an equilibrium laser-particle distance at ~ 420 nm, which is consistent with the experimental rotation radius (Figure 3.13c). The calculated energy potential (red curve) in the radial direction also indicates that the AuNP could be confined at the equilibrium position. It should be noted that although the width of the potential is large, the localized phase transition and high viscosity of quasi-liquid CTAC can effectively eliminate the Brownian motion to retain stable orbital rotation. In the tangential direction, a thermocapillary driving force of ~ 15 fN is obtained, which is consistent with the magnitude of resistant drag forces.

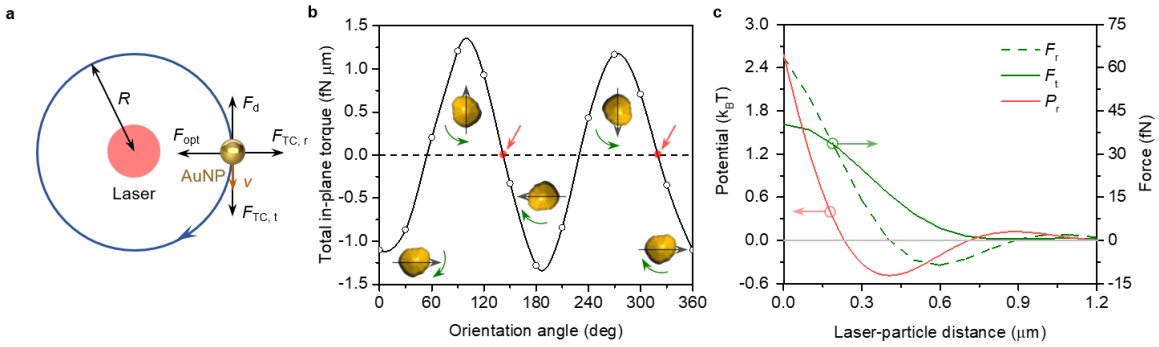

Figure 3.17: Working principle of sOTNM. (a) In-plane force analysis of sOTNM. $\boldsymbol{F}_{opt}$ is optical force, $\boldsymbol{F}_d$ refers to resistant drag force, $\boldsymbol{F}_{TC,\,t}$ and $\boldsymbol{F}_{TC,\,r}$ are the tangential and radial components of thermocapillary forces, respectively. (b) Calculated total in-plane torques as a function of the orientation angle of the AuNP. The red arrows show two equilibrium orientation angles where the torque equals zero. The black and green arrows indicate the orientation of the AuNP and the rotation direction at a certain orientation, respectively. (c) Calculated total forces in the radial direction ($\boldsymbol{F}_r$), total forces in the tangential direction ($\boldsymbol{F}_t$), and the potential in the radial direction (P_r) as a function of laser-particle distance.

To validate the proposed working mechanisms, we developed a physical model to numerically analyze the motion of the AuNP. We considered an asymmetric AuNP interacting with a 660 nm laser. The AuNP experienced thermocapillary forces, optical forces, resistant drag forces, and torques as a function of the position and orientation of the AuNP, which were obtained from numerical simulations and analytical methods. At the initial time, the AuNP was placed at a random position with random orientation (Figure 3.18a). Due to the large restoring torque acting on the particle, the AuNP reoriented itself toward the equilibrium orientation during the first couple of milliseconds. Then, within 0.3 seconds, the AuNP was dragged toward the circular orbital while simultaneously maintaining at the equilibrium in-plane orientation induced by the restoring torques (Figure 3.18b, c). Subsequently, the AuNP started to rotate along the laser beam in a circular orbit

stably (Figure 3.18d). The trajectory and velocity of the AuNP matched well with the experimental results in Figure 3.13c.

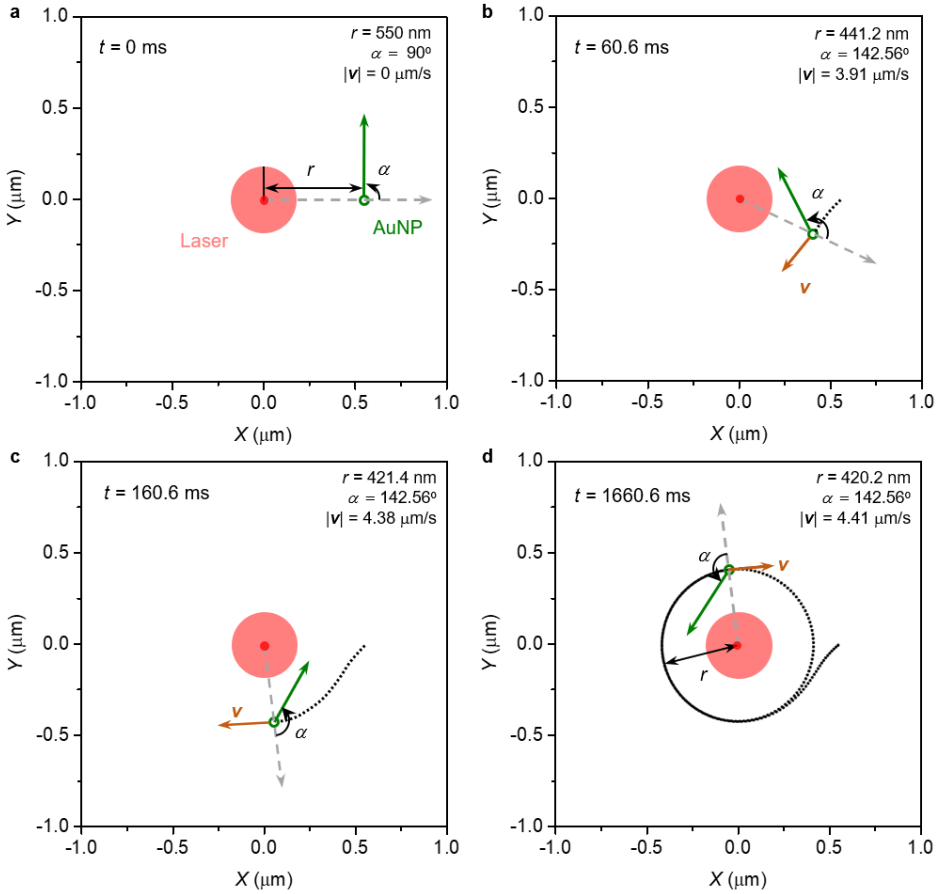

Figure 3.18: Modeling of the motion of sOTNM. (a) At the initial time, an asymmetric AuNP with a random orientation was placed at a laser-particle distance of 550 nm. All forces and torques based on numerical simulations were exerted on the AuNP. The green arrow indicates the orientation of the AuNP. r is the laser-particle distance and α defines the orientation angle of the AuNP with respect to radial direction (grey dashed arrow). (b, c) The AuNP approached the circular orbit with reorientation at (b) t = 60. 6 ms and (c) t = 160. 6 ms. $\boldsymbol{v}$ is the instant velocity of the AuNP, and the black dot line shows the trajectory of the AuNP. (d) Steady rotation state of the AuNP.

In the real case, there exist perturbations in the system caused by the fluctuation of laser power, non-uniformity in the CTAC layer, as well as the vibration of the stage. To better represent the actual experimental behavior, we added noise in the model to mimic the experimental fluctuations. In the presence of noise, the AuNP rotated in the circular orbit with some position fluctuations, which is similar to the experimental results (Figure 3.19). The replication of experimental rotation behaviors in our physical model indicates the reliability and effectiveness of our proposed mechanisms. In addition to AuNPs, we further demonstrated the orbital rotation of silver nanoparticles, showing the general applicability of sOTNM.

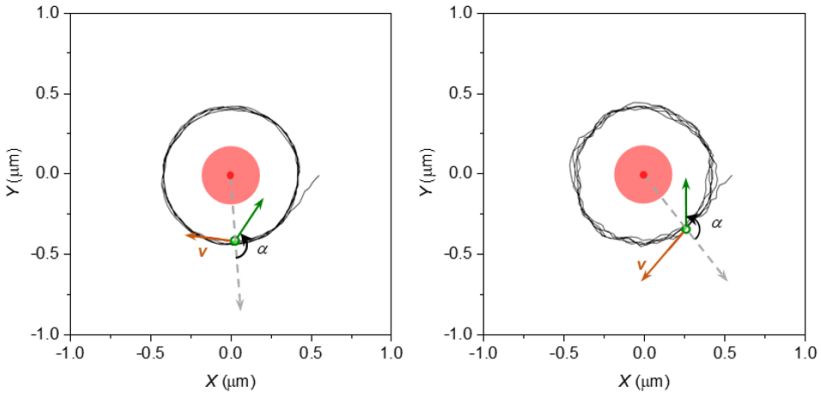

Figure 3.19: Modeling of the motion of sOTNM with (left) 10% noise and (right) 25% noise. In the presence of noise, the AuNP still rotates steadily in the circular orbit with some fluctuations, which is similar to the experimental scenario.

Last, we investigated the dependence of laser power on the rotation behaviors of sOTNM. As discussed previously, the rotation radius is the equilibrium position determined by the balance of optical force and thermocapillary force in the radial direction, which is independent of the laser power. Therefore, the experimental rotation radius of sOTNM was in the range of ~ 0.4-0.6 μm for a power range of ~1-10 mW (Figure 3.20a).

The angular velocity of sOTNM is dependent on the thermocapillary driving forces, which are related to the laser power, asymmetric geometry, and the equilibrium orientation of the AuNP. The experimental rotation rate was weakly correlated to the laser power with a slightly increasing trend (Figure 3.20b). To understand this correlation, we analyzed the theoretical rotation radius and angular velocity for different asymmetric AuNPs to account for the geometrical variations. The calculation results for all AuNPs are consistent with the experimental results, as indicated by the shaded areas in Figure 3.20.

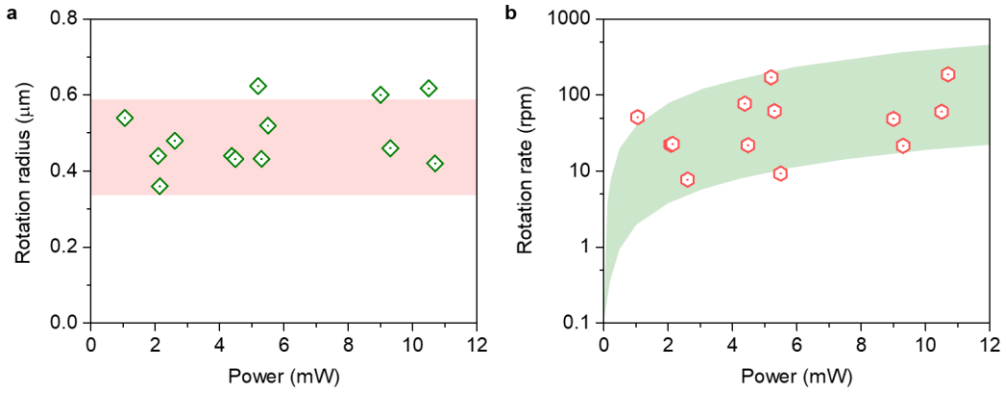

Figure 3.20: Power-dependent rotation behaviors of sOTNM. (a) Rotation radius and (b) rotation rate of sOTNM as a function of laser power. The shaded areas correspond to the ranges obtained via the calculated theoretical values from different asymmetric AuNPs.

In summary, we have developed sOTNM as a new type of light-driven nanomotors that are operated on a solid substrate without Brownian motion. sOTNM is driven by the synergy of optical forces and thermocapillary forces, in which the geometry of the nanoparticle plays an important role. We have further established a physical model to understand the origin of driving forces induced by the asymmetry of nanomotors, which may shed light on the future design and optimization of optical nanomotors.

This sOTNM provides many exciting possibilities in nanotechnological applications. It presents a new design of nanoscale motors to fill the scale gap between molecular machines and microengines. sOTNM can serve as fuel-free and gear-free rotary nanoengines for nano-electromechanical systems to produce mechanical energy and perform work. The light-to-energy conversion efficiency of sOTNM was estimated to be ~10^{-14} at a laser power of 5-10 mW, which is comparable with the state-of-the-art microscopic optical engines.[171] In comparison to other solid-phase motors based on liquid-crystal films,[176-178] sOTNM has no specific requirements for the materials or light sources, making it compatible with current complementary metal-oxide-semiconductor technologies. Operating on the solid substrate without being affected by Brownian motion, sOTNM can be integrated with solid-state nanoelectronics to bring new functions and opportunities in the development of on-chip active nanodevices for applications in photonics, optoelectronics, and optomechanics.

3.3 ASSEMBLY OF SOLID-PHASE RECONFIGURABLE CHIRAL NANOSTRUCTURES††

Subwavelength nanostructures with tunable compositions and geometries show favorable optical functionalities for the implementation of nanophotonic systems. Precise and versatile control of structural configurations on solid substrates is essential for their applications in on-chip devices such as beam steerers, polarization converters, and molecular sensors. In this section, all-optical assemble of reconfigurable dielectric chiral metamaterials on a solid surface is demonstrated using silicon nanoparticles and nanowires

†† This chapter is reproduced from following manuscript published:
J. Li[#], M. Wang[#], Z. Wu, H. Li, G. Hu, T. Jiang, J. Guo, Y. Liu, K. Yao, Z. Chen, J. Fang, D. L. Fan, B. A. Korgel, A. Alù, Y. Zheng. Tunable Chiral Optics in All-Solid-Phase Reconfigurable Dielectric Nanostructures. *Nano Lett.* **2021**, *21*, 973–979.
J. Li is the first author of this paper.

as the building blocks. The chiroptical response is tailorable on-demand by dynamic manipulation of the silicon nanoparticle.

Chiral structures with intriguing chiroptical properties have been burgeoned as promising candidates for a wide range of emerging applications, including chiral sensing,[179-181] enantioselective separation,[182, 183] and valleytronics.[184-186] Recently, a new trend has been emerging to evolve conventional static chiral nanostructures into dynamic systems for on-demand control of optical chirality to enable adaptable platforms for various applications.[187] DNA nanotechnologies permit the fabrication of plasmonic chiral nanostructures, in which the configurations can be further tuned by external stimuli such as strand displacement, light, and pH.[188] In another approach, individual colloidal particles in the solution can be reversibly arranged into opposite chiral geometries via applying a light-controlled opto-thermoelectric field.[135] However, these solution-based methods generally suffer from Brownian motion of nanoparticles and undesired capillary forces, which largely limits their applications for reliable and stable on-chip devices.

To overcome these limitations, we demonstrate all-solid-phase reconfigurable chiral nanostructures, where the geometry and chiroptical properties can be dynamically tailored on a solid substrate without liquid media.[189] Our chiral nanostructures are constructed by delivering a single SiNP to the vicinity of a silicon nanowire (SiNW) via our recently developed optothermally-gated photon nudging (Figure 3.21a).[174] Briefly, a thin solid layer of CTAC is introduced between colloids and the glass substrate to modulate the particle-substrate interactions. When the laser heats the SiNP to a temperature higher than 350 K, CTAC surrounding the SiNP undergoes an order-disorder transition from a crystalline phase to a quasi-liquid structure. Simultaneously, the SiNP is nudged away against the laser beam by optical scattering forces. It should be noted that optical forces

can push the SiNP under any polarizations, which enables the effective manipulation of SiNPs in all directions on the substrate.

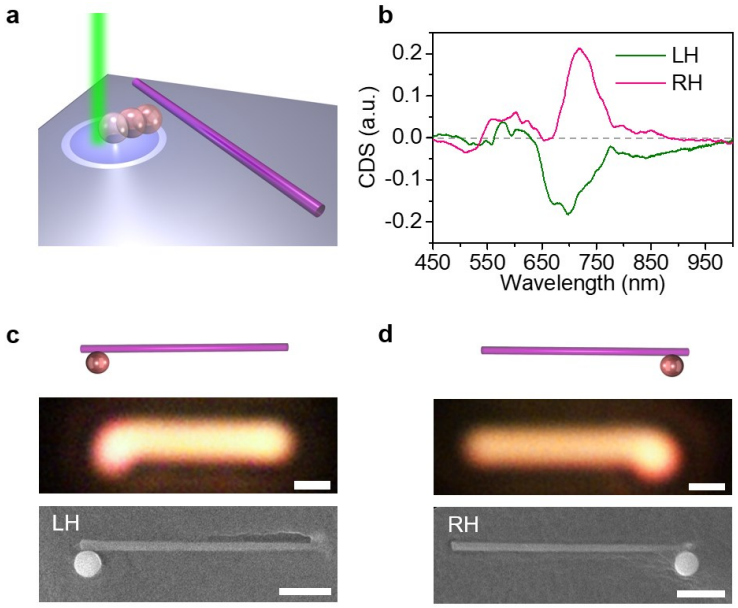

Figure 3.21: Assembly of solid-phase dielectric chiral nanostructures. (a) Schematic showing the assembly of LH chiral structure. (b) The measured CDS spectra of the assembled chiral nanostructures in panels c and d. (c,d) Schematic, optical, and SEM images of the assembled LH (c) and RH (d) chiral nanostructures. Scale bars: 1 μm.

By steering the laser beam, a SiNP can be dynamically transported to the target position near the SiNW to build chiral nanostructures (Figure 3.22). The geometry of the assembled structures can be further tuned by transporting the SiNP along the SiNW, rendering large and tunable chiroptical responses. Figure 3.21c,d shows dark-field optical micrographs and SEM images of the optically assembled chiral nanostructures, where left-handed (LH) and right-handed (RH) structures correspond to L-shaped and mirror-L-shaped patterns, respectively. The handedness of chiral structures is determined by the location of the SiNP against the SiNW. LH and RH nanostructures exhibit handedness-

dependent optical responses to circularly polarized light (Figure 3.21b), which will be discussed in detail in the following context.

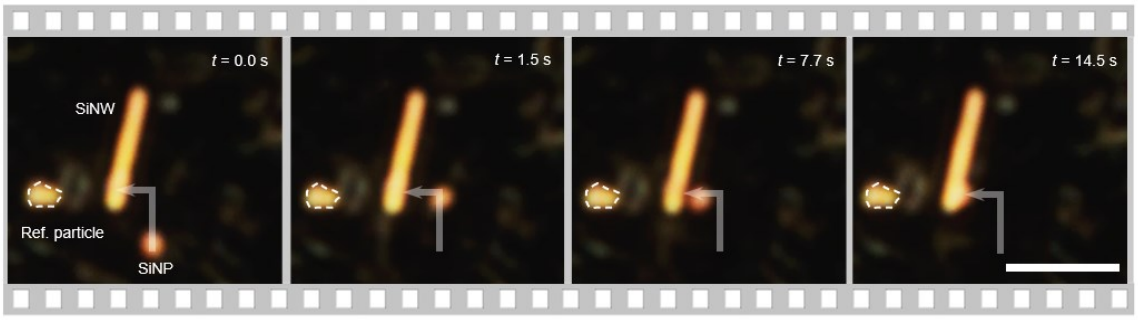

Figure 3.22: Sequential dark-field optical images showing real-time construction of chiral structures with a SiNP and a SiNW. The white arrows depict the path. Scale bar: 5 μm.

To account for the observed chiral optical response, we first examine each individual building block. Specifically, such chiral nanostructures are composed of a hydrogenated amorphous SiNP (~500 nm in diameter) and a single-crystalline SiNW (~170 nm in diameter and ~5 μm in length) with high refractive indexes (~ 4 at the visible wavelengths). In comparison to their plasmonic counterparts,[190, 191] dielectric silicon nanostructures feature low material loss, pronounced magnetic resonances in the visible and near-infrared ranges, and CMOS compatibility for the development of integrated photonic and electronic systems.[192-195] Figure 3.23a shows the measured scattering spectrum of a single SiNP. Two major peaks at 620 nm and 745 nm are mainly attributed to the magnetic octupole (MO) and magnetic quadrupole (MQ) resonances, respectively, which are consistent with the calculated results in Figure 3.23c by Mie theory.[196] The sharp MQ and MO scattering peaks confirm the low dissipative nature of hydrogenated amorphous SiNP in the visible and near-infrared range.[197] The scattering spectrum of a

single SiNW shows two peaks at 520 nm and 700 nm (Figure 3.23b), which also agrees well with the calculated result (Figure 3.23d). The peak at 700 nm corresponds to the magnetic dipole (MD) resonance of the SiNW (inset in Figure 3.23d).[198] The experimental and calculated spectra are also in good agreement with the FDTD simulation results. We note that the high-quality Mie resonance here is very important for enhanced light-matter interactions, which, after the assembly, could promise the large chiroptical response as further revealed numerically later.

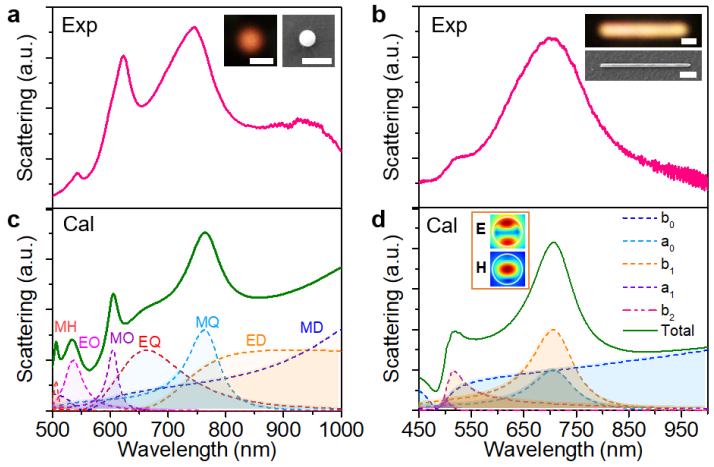

Figure 3.23: Building blocks of chiral structures. (a,b) Experimental scattering spectra of a SiNP (a) and a SiNW (b). The insets show the corresponding optical and SEM images. Scale bars: 1 μm. (c) Scattering spectra of a 500 nm SiNP along with multipole decomposition calculated with Mie theory. MD, magnetic dipole; ED, electric diploe; MQ, magnetic quadrupole; EQ, electric quadrupole; MO, magnetic octupole; EO, electric octupole; and MH, magnetic hexadecapole. (d) Calculated scattering spectra and multipole decomposition of a SiNW with a diameter of 165 nm. Inset shows the electric and magnetic field distribution in the cross-section of the SiNW at 700 nm.

Now, we discuss the tunable chiroptical responses of the assembled nanostructures. Figure 3.24a schematically shows the reconfigurable construction of chiral nanostructures with different handedness. Individual SiNPs and SiNWs were first dispersed on a glass substrate as achiral building blocks (Figure 3.24b). Chiral nanostructures were assembled by moving the SiNP to the vicinity of the SiNW to break the mirror symmetry. By transporting the SiNP along the SiNW from one end to the other end, LH, achiral, and RH structures were constructed sequentially (Figure 3.24c-e). We measured the far-field forward scattering spectra of the assembled nanostructures at the connection between the SiNP and SiNW under both left-handed circularly polarized (LCP) and right-handed circularly polarized (RCP) illumination and calculated the circular differential scattering (CDS) spectra. Firstly, we observed that, compared to RCP incidence, the LH structure has a stronger scattering peak at ~730 nm under LCP light (Figure 3.24g), leading to a negative CDS peak (Figure 3.24f). As a result of the simple argument of mirror geometry, the RH structure exhibits an anticipated handedness-flipped chiroptical response when illuminated by circularly polarized light (Figure 3.24f, i), further indicating the enantiomeric characteristic of the assembled structures. Not surprisingly, the achiral structure where the SiNP is located near the center of the nanowire shows no optical chirality as the mirror symmetry is restored (Figure 3.24h). Secondly, the most significant chiroptical response (near the wavelength 720 nm) happens at the maximal spectral overlap of the strong Mie resonance between the SiNW (MD resonance) and the SiNP (MQ resonance), indicating that the origins of the enhanced optical chirality from the Mie resonance coupling, which will be further supported in the following numerical simulations. In addition, compared to the single SiNW under circularly polarized lights, the scattering peak in all LH, RH, and achiral structures shows a blue shift (from ~745 nm to ~730 nm), which indicates the coupling between the SiNW and the SiNP at Mie magnetic resonances.[199, 200]

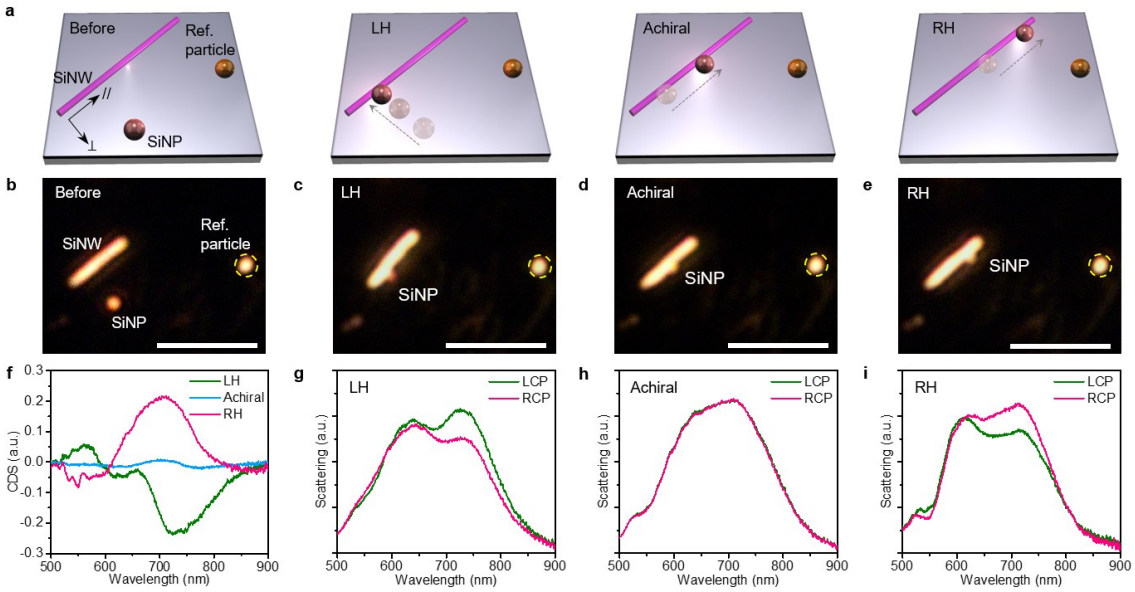

Figure 3.24: Reconfigurable construction on a solid substrate. (a) Schematic illustration of the on-demand assembly of the SiNP-SiNW nanostructure with LH, achiral, or RH configuration. (b-e) Optical images of dispersed building blocks (b), LH (c), achiral (d), and RH (e) structures. All scale bars are 5 μm. (f) CDS spectra of LH, achiral, and RH structures. (g-i), Optical scattering spectra of LH (g), achiral (h), and RH (i) structures under LCP and RCP illumination.

We last remark that the chiroptical response can also be modified by flipping the SiNP from one side to the other side of the SiNW, with similar results as described above (Figure 3.25). By controlling the location of the SiNP in the dielectric nanostructures on solid substrates, the optical chirality can be reversed and turned ON/OFF dynamically, which offers remarkable potential for developing active on-chip chiroptical devices.

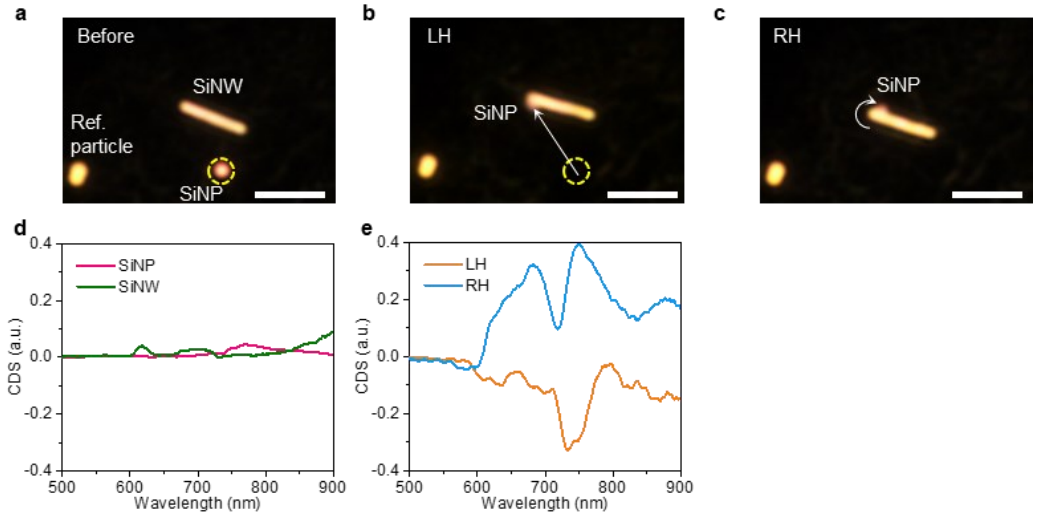

Figure 3.25: Another example of reconfigurable chiral nanostructures on a solid substrate. (a-c) Dark-field optical images of (a) a SiNP and a SiNW before assembly, (b) the assembled LH structure, and (c) the assembled RH structure. (d) Measured CDS spectra of the single SiNP and SiNW. The single dielectric components show negligible chiroptical response. (e) Measured CDS spectra of the assembled LH and RH structures. This result demonstrates that the handedness of the chiral nanostructures can be switched by simply moving the SiNP from one side to the other side of the SiNW. All scale bars are 5 μm.

To further interpret the chiroptical responses, we performed a full-wave numerical simulation using the FDTD method. The simulated scattering spectra of all the structures are in good agreement with the experimental data, with two major peaks at ~620 and ~740 nm. Taking the LH structure as an example, a polarization-sensitive behavior can be clearly identified, in which the LCP light can be scattered more effectively at peak positions (Figure 3.26a). The calculated CDS spectra based on the simulation also present handedness-flipped responses with two peaks for LH and RH assemblies (Figure 3.26b), which are well consistent with the experimental data in Figure 3.24f. Previous studies revealed that the coupling between magnetic resonances could lead to strong electric field

enhancement in the gap of the silicon dimer, which is strongly affected by the polarization of the incident beam.[199-201] In our case, this polarization-dependent modulation of scattering intensity can be attributed to the tailored chiral coupling between the SiNP and SiNW at magnetic resonances, as illustrated by the simulated electric field distributions (Figure 3.26c-f).[202] By comparing Figure 3.26c with Figure 3.26d, a more pronounced hotspot at the gap between the SiNP and the SiNW is distinctly observed for LCP incidence at 740 nm, which indicates the stronger electric field enhancement and chirality-selective optical scattering. In contrast, for the achiral structure, the electric field distributions under LCP and RCP irradiation are identical (Figure 3.26e, f), leading to the same optical scattering spectra under light with opposite circular polarizations. Similarly, stronger electric field enhancement is observed for the LH structure under LCP incidence at 620 nm.

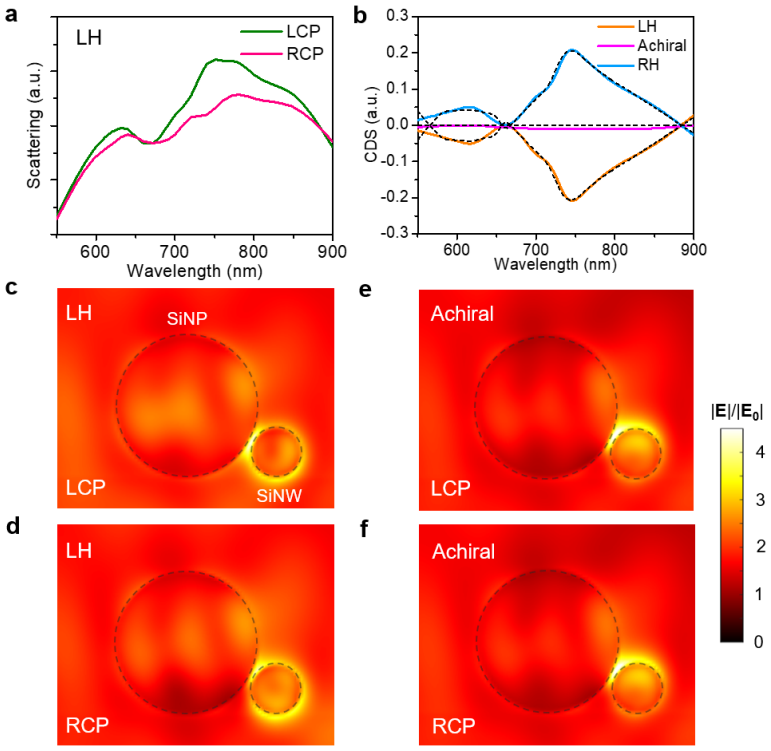

Figure 3.26: FDTD simulation and coupled-mode theory analysis. (a) Simulated scattering spectra of the LH structure under LCP and RCP illumination. (b) Simulated CDS spectra of LH, achiral, and RH structures. The black dashed lines are the fitting curves via the coupled-mode theory. (c,d) The electric field distributions in the LH structure at 740 nm induced by LCP (c) and RCP (d) incidence. (e,f) The electric field distributions in achiral structure at 740 nm induced by LCP (e) and RCP (f) incidence. All electric field distributions are cut at the cross-sectional plane of the SiNW passing through the center of the SiNP.

In addition, we simulated the electric field components along the SiNW ($\mathbf{E}_{//}$) and perpendicular to the SiNW ($\mathbf{E}_{\perp}$) to further unravel the chiral couplings in the assembled nanostructures. The results show that the $\mathbf{E}_{\perp}$ has a brighter hotspot in the SiNP-SiNW gap and exhibits a distinct chiroptical response (Figure 3.27a), while the $\mathbf{E}_{//}$ is weak in the gap and insensitive to the handedness of the incident beam (Figure 3.27b). This result is because the electric field across the gap between two dielectric nanoparticles is dominant

over other components.[201] The electric dipole moment in the SiNP can induce strong $\mathbf{E}_{\perp}$ in the gap, and the field enhancement is dependent on the handedness of the incident light. Finally, it should be mentioned that no remarkable asymmetric response in magnetic field distributions is observed at the gap. The reason is that the magnetic fields mainly localize inside the SiNW and SiNP, and thus the magnetic field enhancement in the gap brought by the coupling between SiNW and SiNP is weaker than the electric field.[199]

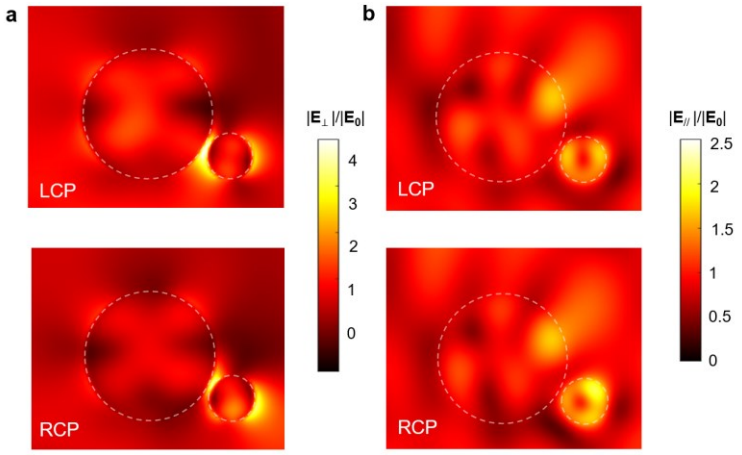

Figure 3.27: Simulated in-plane electric field components mapping in the LH structure at 740 nm. Electric field components (a) perpendicular to the SiNW ($E_{\perp}$) and (b) parallel to the SiNW ($E_{//}$) under LCP and RCP incidence.

Next, coupled-mode theory (CMT) is adopted to provide an intuitive understanding of the origins of the chiral response of the assembled nanostructures, as inspired by the Born-Kuhn model for the description of chiral media.[203, 204] In our theoretical model, the system consists of two optical resonators, i.e., the SiNP and the SiNW, which involve two dominant bare modes of energy-normalized amplitudes $a_n, n = 1,2$. For simplicity, we assume that they are of equal resonance (angular) frequency ω_0 and coupled with the strength ξ. For the scattering experiment, we consider that the system is coupled with three

channels, within which the first two support the light of two distinguished polarizations connected with the source and the third for the detector. Correspondingly, propagating through these channels, inputs and output are respectively represented by 3×1 complex vectors $|S_+\rangle$ and $|S_-\rangle$ consisting of flux-normalized wave amplitudes. Indeed, other propagating channels can be accounted for as additional radiation losses and incorporated in a Hermitian matrix Γ describing all the dissipation processes of the resonators. Under these considerations, the interaction between the incoming waves, the resonators, and the outgoing waves can be modeled as[205]

$$\frac{d\boldsymbol{a}}{dt} = (i\Omega - \Gamma)\boldsymbol{a} + D(\theta)^T|S_+\rangle \tag{11}$$

$$|S_-\rangle = K(\theta)|S_+\rangle + D(\theta)\boldsymbol{a} \tag{12}$$

where $\boldsymbol{a} = \begin{pmatrix} a_1 \\ a_2 \end{pmatrix}$, and $\Omega = \begin{pmatrix} \omega_0 & \xi \\ \xi & \omega_0 \end{pmatrix}$. The matrices $K(\theta)$ and $D(\theta)$ represent the direct non-resonance scattering and couplings between the modes and the channels, respectively. They depend on an effective phase difference θ due to wave interactions in the structure of finite sizes[206, 207] and can be controlled by the relative positions of the SiNP and the SiNW. The CMT fitting curves are well consistent with the numerical simulations (Figure 3.26b), indicating that the optical chirality results from the couplings between the optical resonances in the SiNP and the SiNW. In addition, the coupling between the resonance modes under LCP and RCP illumination is determined by the phase difference between the SiNP and the SiNW. For LH and RH structures with mirrored geometries, the opposite phase difference leads to a handedness-flipped optical response under circularly polarized light.[208] The CMT analysis further suggests that the maximal chiroptical response should happen at the largest degree of broken mirror symmetry with the largest phase difference, which, in our case, corresponds to the position of the SiNP near the end of the SiNW.

Last, as a case study, we show the practical applications of chiral sensing in our system with unique advantages brought by the all-solid-phase assembly. Dielectric nanostructures are well-known to support the strong enhancement of both electric and magnetic fields, which leads to a remarkable enhancement of near-field optical chirality. The optical chirality C is defined as[209]

$$C \equiv \frac{\varepsilon_0}{2}\mathbf{E}\cdot\nabla\times\mathbf{E} + \frac{1}{2\mu_0}\mathbf{B}\cdot\nabla\times\mathbf{B} \quad (13)$$

where ε_0 and μ_0 are the permittivity and permeability of free space, respectively; and **E** and **B** are the local electric and magnetic fields, respectively. The parameter C thus determines the degree of chiral asymmetry in the rate of excitation of a chiral molecule.[209] We simulated the electromagnetic field distributions at the plane normal to the light incident direction and calculated the corresponding optical chirality. Under the irradiation with different circular polarization states, the optical chirality fields in chiral structures show opposite signs, which can induce strong polarization-dependent interactions between chiral molecules and the chiral structures (Figure 3.28a). Consequently, the adsorption of chiral molecules on the chiral structures results in asymmetric modification of the local refractive index and thus asymmetric peak shifts upon LCP and RCP light illumination.[210]

We demonstrated the chiral sensing capability of the assembled chiral nanostructures using two enantiomers of Phenylalanine (2 mg mL^{-1}) as the sample analytes. Phenylalanine is an essential α-amino acid, and L-Phenylalanine is frequently used for the synthesis of pharmaceutically active chemicals and the diagnosis of phenylketonuria.[211] We measured the peak shifts of CDS spectra ($\Delta\lambda_{LH}$ and $\Delta\lambda_{RH}$ for LH and RH structures, respectively) induced by the chiral molecules and calculated the dissymmetric factor $\Delta\Delta\lambda = \Delta\lambda_{LH} - \Delta\lambda_{RH}$ (Figure 3.28b), which reflects the structural chirality of the adsorbed molecules.[212] The $\Delta\Delta\lambda$ has a positive value (1.16 ± 0.47 nm) for D-Phenylalanine, while it

is negative (-0.90 ± 0.44 nm) for L-Phenylalanine (Figure 3.28c). The detection concentration is comparable to plasmonic metamaterials and superior to the conventional chiroptical spectroscopy, reflecting the good figure of merit of all-dielectric chiral nanostructures. We also remark that our system is in all solid phases, which further brings new advantages of stabilities and reliability against the sensing systems fabricated by solution-based methods.

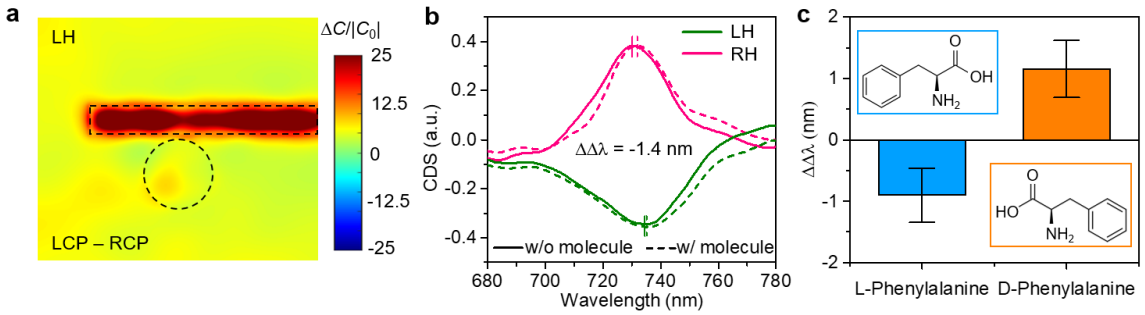

Figure 3.28: Enhanced chiral sensing. (a) Differential optical chirality mapping in the LH structure at 740 nm under LCP and RCP illumination. C_0 is the chirality for circularly polarized light without the nanostructure. (b) CDS spectra of the LH and RH structures before and after the adsorption of L-Phenylalanine. (c) ΔΔλ values for L-Phenylalanine and D-Phenylalanine. The opposite signs of ΔΔλ values reveal the opposite handedness of L-Phenylalanine and D-Phenylalanine. Insets show the chemical structures of the chiral molecules.

In summary, we have demonstrated handedness-dependent coupling in reconfigurable dielectric nanostructures on solid substrates without requiring liquid media. The configuration of the nanostructures can be largely tailored to tune their chiroptical properties. Using numerical simulation and coupled-mode theory analysis, we elucidated the coupling between Mie resonances of the SiNP and SiNW as the origin of chirality in our nanostructures. We envision that this study will bring new insights and possibilities in various chiroptical applications, such as enantiodiscrimination and polarization

conversion, for the development of safer drugs and advanced optical tools. In addition, as a general method to construct reconfigurable nanostructures on the solid substrate, our strategy will also enable the versatile fabrication of adaptive on-chip nanodevices for a wide range of photonic and electronic applications.

Chapter 4: Opto-Thermoplasmonic Nanolithography of 2D Materials‡‡

Since the first discovery of graphene, 2D materials have drawn tremendous attention due to their atomic thickness and super properties. Fabrication of high-quality micro-/nano-patterns of 2D materials is essential for their applications in both nanoelectronics and nanophotonics. In this Chapter, an all-optical lithographic technique, termed opto-thermoplasmonic nanolithography, is developed to achieve high-throughput, versatile, and maskless patterning of different atomic layers. Low-power (~5 $mW/\mu m^2$) and high-resolution patterning of both graphene and MoS_2 monolayers is demonstrated through exploiting thermal oxidation and sublimation at the highly localized thermoplasmonic hot spots. Density functional theory (DFT) simulations reveal that Au nanoparticles reduce the formation energy (~0.6 eV) of C monovacancy through bonding between under-coordinated C and Au, leading to significant Au-catalyzed graphene oxidation and a reduction of operation power. Programmable patterning of 2D materials into complex and large-scale nanostructures is further demonstrated.

Atomically-thin 2D materials exhibit many unique and extraordinary properties beyond their bulk parental materials, such as excellent mechanical flexibility, high thermal conductivity, as well as tunable electronic band-gap.[213-216] The increasing material diversity with emerging new electric and optical properties has led to the development of novel 2D electronic and photoelectronic devices, including field-effect transistors, photon detectors, light-emitting diodes, and solar cells.[217-220] The precise control of the size and shape of 2D materials is one critical fabrication step for device applications.[221] Specifically, the geometry control of 2D materials at wavelength and sub-wavelength scale can significantly

‡‡ This chapter is reproduced from following manuscript published:
L. Lin[#], **J. Li**[#], W. Li[#], M. N. Yogeesh, J. Shi, X. Peng, Y. Liu, B. B. Rajeeva, M. F. Becker, Y. Liu, D. Akinwande, Y. Zheng. Opto-Thermoplasmonic Nanolithography for On-Demand Patterning of 2D Materials. *Adv.anced Functional Materials* **2018**, 28, 1803990.
J. Li is the co-first author of this paper.

tune their optical responses.[222, 223] Traditional top-down patterning techniques, including photolithography,[224] electron beam lithography,[222, 225] and ion beam lithography,[226, 227] have been extensively employed to fabricate diverse 2D patterns. However, they typically require complex instruments with high cost and multiple-step processing.

Laser processing of low-dimensional materials is a remotely controlled, one-step, maskless, and low-cost fabrication technique that provides an alternative approach.[228] The direct or indirect light-matter interactions at the laser spots, e.g., laser-induced thermal effect,[229] radiation force,[230] or photon-assisted chemical reaction,[231] open new ways to control or modify the composition, structure, and geometry of materials.[232-234] In the past few years, laser processing of 2D materials using femtosecond laser has also been achieved.[21, 235-238] However, high optical power is usually required, and the fabrication of sub-micron patterns is still challenging.

Light-driven coherent oscillation of surface electrons on metal nanoparticles, i.e., the excitation of surface plasmons, can dramatically amplify optical signals.[239] Particularly, the plasmon-enhanced electric field at localized nanoscale regions improves the light-matter interaction and facilitates the development of novel optical techniques in material processing. For example, the confinement of light with a plasmonic mask significantly overcomes the diffraction limit and leads to the development of plasmonic nanolithography.[240, 241] Herein, taking advantage of the plasmon-enhanced light absorption in metal nanoparticles and the localized optical heating effect,[32, 61] we develop a new optical tool, opto-thermoplasmonic nanolithography (OTNL), for low-power, on-demand, and programmable patterning of 2D materials using a continuous-wave laser. Taking graphene and molybdenum disulfide monolayers as examples, we show that both thermal oxidation and sublimation in the light-directed temperature field can lead to direct etching of the atomic layers, which are further supported by our simulations. Through steering the

laser beam, we demonstrate arbitrary and complex 2D patterns with both high throughput and high resolution.

Figure 4.1a shows the whole process of OTNL. A porous Au film consisting of high-density and quasi-continuous AuNPs serves as a thermoplasmonic substrate (Figure 4.1b, c). Under radiation of a focused 532 nm laser beam, localized surface plasmon resonances are excited on the thermoplasmonic substrate, with both high-efficiency light absorption and light-to-heat conversion. The high-density gold nanoparticles lead to well-confined and localized thermal hot spots during optical heating. As shown in Figure 4.1d, we simulated the in-plane temperature distribution when the thermoplasmonic surface is heated by a laser beam of 6.4 $mW/\mu m^2$ in optical intensity, revealing a maximum temperature of 850 K. To achieve coupling between the 2D materials and the thermal hot spots, we transfer graphene or MoS_2 monolayers onto the thermoplasmonic substrate. Through steering the laser beam with a spatial light modulator or translating the substrate *via* a motorized stage, we achieve dynamic interaction between the 2D materials and the thermal hot spots for arbitrary optical patterning (Figure 4.1e). The patterning of 2D materials was further characterized by an atomic force microscope (Figure 4.1f, g). As shown in Figure 4.1g, a clear trench can be observed at the laser-scanned area, which indicates the graphene was removed after optical patterning.

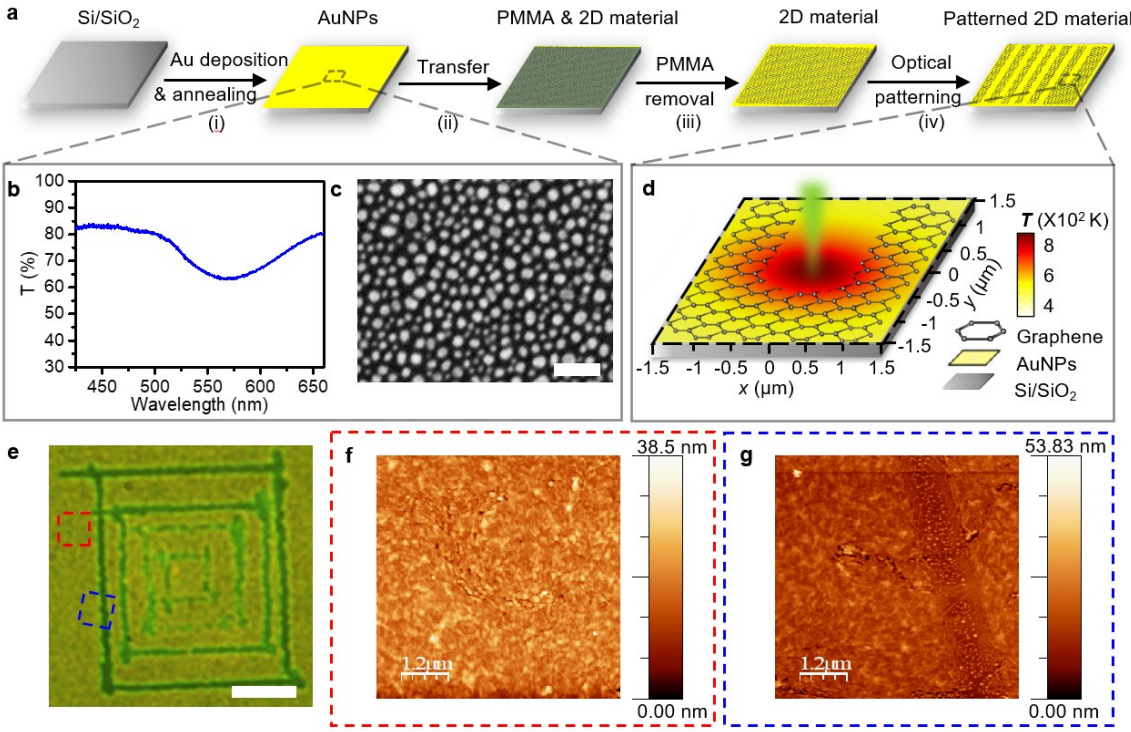

Figure 4.1: General concept of OTNL. (a) Schematic flowchart of OTNL process for 2D materials patterning, which includes i) fabrication of thermoplasmonic substrate; ii) transfer of 2D materials onto the thermoplasmonic substrate; iii) PMMA removal by acetone; and iv) optical patterning of 2D materials. (b) The absorption spectrum and (c) scanning electron micrograph of thermoplasmonic substrate. (d) Enlarged scheme showing the working area of OTNL. The embedded shows the simulated temperature distribution of the thermoplasmonic substrate around the laser spot. Laser beam size: 1 μm and incident power: 6.4 mW μm^{-2}. (e) Optical images of four squares patterned on graphene. The linewidth is ~1 μm. AFM images of (f) unpatterned area (red rectangle in e) and (g) patterned area (blue rectangle in e) of graphene. A clear trench can be observed in (g). Scale bars: (c) 100 nm and (e) 10 μm.

Figure 4.2a shows the Raman spectrum of graphene before patterning. Both high I_{2D}/I_G ratio of approximately 5 and narrow full-width at half-maximum (FWHM) of the 2D peak (~ 40 cm^{-1}) reveal the high-quality graphene monolayer.[242] For MoS_2, The distance between the E_{2g} band and the A_{1g} band is ~19 cm^{-1} (Figure 4.2b), which is consistent with

the value for MoS_2 monolayer in previous work.[238] The photoluminescence (PL) spectrum of MoS_2 shows an intensive PL peak at 675 nm, which further confirms the existence of MoS_2 monolayer (Figure 4.2c).[243] The Raman mapping images of I_{2D}/I_G ratio of graphene before and after transfer further verify the high crystalline quality after they are transferred onto the thermoplasmonic substrate (Figure 4.3a, b).

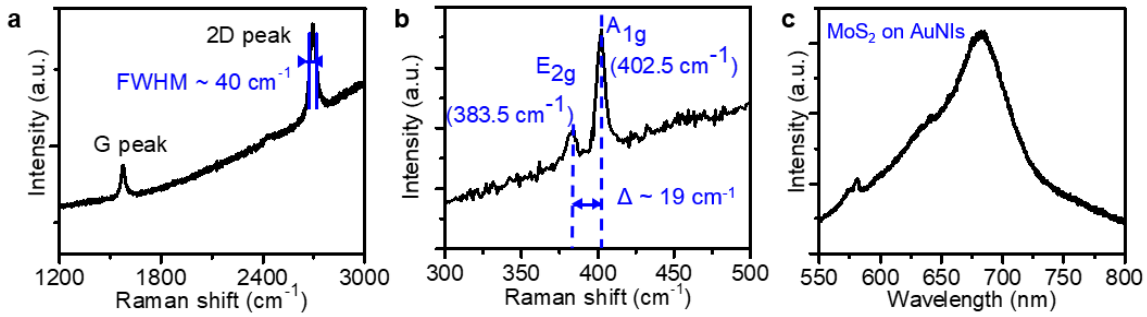

Figure 4.2: Characterizations of graphene and MoS_2. (a, b) Raman spectra of (a) graphene and (b) MoS_2 before patterning. (c) Photoluminescence spectra of MoS_2 on AuNIs.

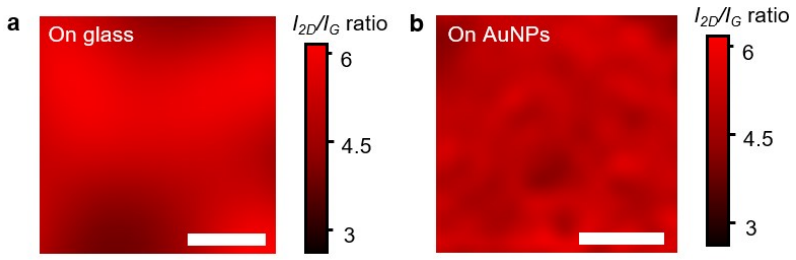

Figure 4.3: Raman mapping of graphene. (a, b) Raman mapping images of I_{2D}/I_G ratio of graphene (e) before and (f) after being transferred onto thermoplasmonic substrate. The large I_{2D}/I_G ratios (>4) represent the high quality of monolayer graphene. Scale bars: 2 μm.

To evaluate the patterning tunability of OTNL, we examined the feature size by monitoring the Raman patterns of the patterned 2D materials. We created a set of lines on MoS_2 under different incident power with the same scanning speed (Figure 4.4a). The linewidth increases linearly from 300 nm to 1.6 μm when the optical power increases from 4.8 mW/μm^2 to 12.2 mW/μm^2. A minimum linewidth of 300 nm was observed with an incident power intensity of 4.8 mW/μm^2. This optical intensity is about two orders of magnitude lower than that reported in previous works (0.14-2 mW/μm^2). It is worth noting that the linewidth of the remaining ribbon structure can be further reduced by engineering the laser beam shape. For example, by using phase-shifting plates or 2D vortex phase plates, the shaped laser beam profile can be shaped to significantly beat the diffraction limit.[21] Figure 4.4b shows a group of graphene nanoholes patterned with different scanning rates under the same optical power. The diameter of the nanoholes decreases with the increasing scanning rate. A minimum hole diameter of 420 nm is obtained when exposed for 0.067 s. The feature size can also be further reduced by increasing the numerical aperture.

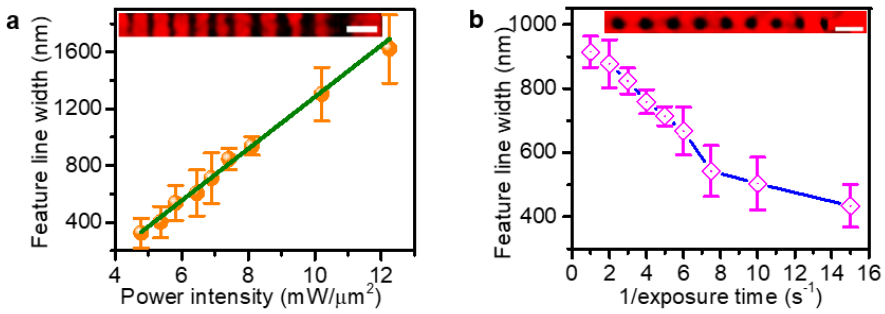

Figure 4.4: Tunable feature sizes in patterned MoS_2 and graphene via OTNL. (a) Power intensity-dependent feature linewidth on MoS_2. A linear relationship between feature linewidth and power intensity was obtained. (d) Exposure time-dependent feature size on graphene. The insets show the Raman mapping images of (c) MoS_2 nanoribbons (A1g peak) and (d) graphene nanohole array (2D peak) in corresponding patterned areas. Red stands for high Raman intensity, and black represents low Raman intensity. Scale bars in insets: 2 μm.

To understand the interaction between the 2D materials and the temperature field, we compare the Raman spectra of graphene and MoS_2 at different regions, as summarized in Figure 4.5a, b. The absence of any significant Raman signal at the ablated area suggests that the 2D materials were completely removed after laser exposure, while pristine Raman spectra can be obtained in the unexposed regions. However, at the interface between the exposed and unexposed regions in the graphene patterns, i.e., the cutting edge, we can see a distinct D band at ~1350 cm^{-1} (Figure 4.5a), which indicates the existence of defects.[244] In our case, the most probable explanation is graphene oxidation during laser ablation, which has also been reported previoulsy.[21, 236] A mapping of the D band in the graphene pattern shows a clear transition region at the etching edge (Figure 4.5c-e), where the radiation dose is insufficient to ablate the graphene due to the Gaussian distribution of the laser spot. For comparison, we also check the Raman spectra at the etching edge of the MoS_2 (Figure 4.5b). However, we did not observe any significant signal from molybdenum

oxide, indicating that the ablation of MoS_2 is caused by lattice sublimation instead of molybdenum oxidation.[237] Sublimation starts from the chemical bonds breaking in MoS_2 lattice and atoms evaporate, and the sublimation temperature for MoS_2 is 450 °C.[245]

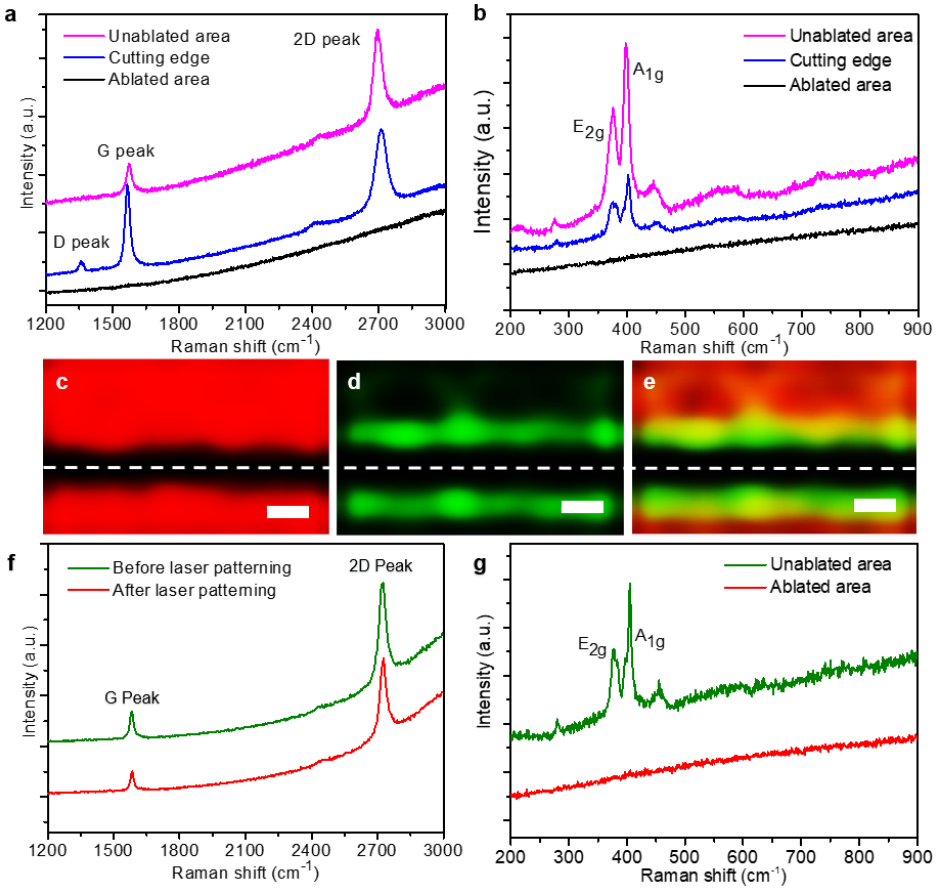

Figure 4.5: Raman measurements for mechanistic study of OTNL. Raman spectra recorded at different areas on (a) graphene and (b) MoS_2 patterned in air. The magenta, blue, and black lines correspond to the unpatterned area, cutting edge, and ablated area, respectively. A distinct D peak was observed at the cutting edge. Raman mapping image of (c) 2D peak, (d) D peak, and (e) a mix of 2D peak and D peak of graphene at the cutting edge. Red or green stands for high Raman intensity, and black represents low Raman intensity. The white dashed line corresponds to the laser-scanned trajectory. Scale bars: 1 μm. Raman spectra recorded at different areas on (f) graphene and (g) MoS_2 patterned with 25 nm Al_2O_3 on top as a protective layer against oxidation. After laser patterning, the Raman spectrum of graphene remained unchanged and the signals of MoS_2 disappeared.

To further verify our hypothesis, we coated 25 nm Al_2O_3 thin films on both graphene and MoS_2 using atomic layer deposition as a protective layer before optical patterning. Al_2O_3 is selected here due to its capability of resisting oxidation even under high temperatures.[246, 247] Based on the thermal conductivity: $\kappa_{silicon} > \kappa_{alumina} > \kappa_{glass} > \kappa_{air}$,[248] the coating of Al_2O_3 thin film will lead to heat dissipation and reduce the maximum temperature during optical heating.[249] Thus, we used silicon as the substrate in this control experiment to avoid a dramatic temperature drop after Al_2O_3 coating. Our COMSOL simulation shows that the coating of Al_2O_3 film has negligible change on the temperature distribution on a silicon substrate. However, it should also be noted that silicon is an effective heat sink, and the replacement of glass by silicon as the substrate gives rise to a much higher optical power to achieve patterning.[249] We compared the Raman spectra before and after optical patterning for both graphene and MoS_2 (Figure 4.5f,g). We can see that, after Al_2O_3 coating, the graphene monolayer cannot be ablated, while the optical patterning of MoS_2 remains achievable. These results reveal that graphene patterning is an oxygen-participated process and can be rationally controlled by tuning the oxygen diffusion into the graphene monolayer. However, the patterning of MoS_2 is independent on the surrounding oxygen concentration, which confirms the sublimation mechanism. Sublimation of graphene can be further excluded since the minimum oxidation temperature of graphene is 450 ^oC[250] and the sublimation temperature is over 2000 ^oC,[251, 252] which is much higher than the maximum temperature in our work.

We further carried out DFT simulations to understand the role of the thermoplasmonic substrate in graphene patterning beyond plasmon-enhanced optical heating. A graphene monolayer is placed on the top of the gold (111) surface with a gap of ~0.3 nm and two oxygen atoms are introduced to model the oxidization process. The oxidation process starts from O_2 dissociation on graphene, and two oxygen atoms take out

one carbon atom to form CO_2, leaving a monovacancy in graphene.[253] We calculated the formation energies of both oxygen adsorption (Figure 4.6a) and the carbon monovacancy (Figure 4.6b), and the results were compared with the formation energies calculated in freestanding graphene. We found that the presence of gold surface did not significantly change the formation energy of oxygen adsorption on graphene (with the formation energy difference < 50 meV), while it dramatically reduces the formation energy of carbon monovacancy by 0.6 eV. The stabilization of carbon monovacancy arises from the bonding between under-coordinated C and Au (Figure 4.6b), indicating that the AuNPs on the thermoplasmonic substrate can catalyze graphene oxidation beyond the improvement of optical heating.

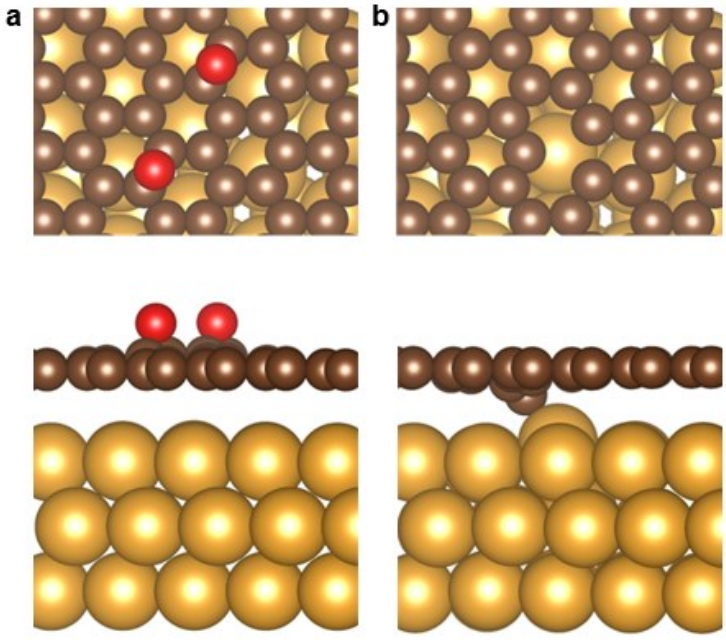

Figure 4.6: DFT modeling of graphene oxidation on the top of a gold surface. Top and side views of (a) two O atoms adsorbed on graphene supported on Au surface, and (b) graphene with one C vacancy supported on Au surface. The red, brown, and gold balls represent O, C, and Au atoms, respectively.

Besides the understanding of the working principle, we further demonstrate the versatility of OTNL for the fabrication of diverse 2D patterns. Figure 4.7a shows the real-time patterning of graphene nanoribbon structure. It takes less than 10 seconds to pattern a 40 μm×40 μm nanoribbon array, showing the high throughput of OTNL. As shown in Figure 4.7b-d, we created graphene nanoribbon arrays with different feature sizes. While tuning the laser scanning periodicity (1.6 μm, 1.35 μm, and 0.95 μm), we fabricated graphene nanoribbon with linewidths of 950 nm (Figure 4.7b), 650 nm (Figure 4.7c), and 500 nm (Figure 4.7d). Two-dimensional graphene nanodisk arrays can also be fabricated through optical etching of surrounding graphene and controlling the sizes and shapes of the remaining graphene, as shown in Figure 4.7e, f. Other periodic structures, including MoS_2 nanohole array (Figure 4.7g) and graphene nanorectangle array (Figure 4.7h), were also readily fabricated. The striking contrast in all Raman images verifies the excellent quality control of the 2D patterns. The precise control of the feature size and periodicity in graphene monolayer can facilitate the optical fabrication of graphene terahertz devices for optical sensing and photon detection.[222, 223] OTNL can also be used to create non-periodic nanostructures with complex patterns. Through programming the sample stage, we demonstrate the patterning of a UT-Austin logo on MoS_2 monolayer (Figure 4.7i), and "Graphene" text created on graphene monolayer (Figure 4.7j), respectively. The UT-Austin logo was patterned by a raster scanning of the stage with a 1 μm line space in conjunction with a shutter to determine an on/off state of the patterning. The acceleration of the stage was set to be 2.4 cm/s^2 and the highest speed was ~1 cm/s. The total time required to fabricate this large-area pattern (150 μm×120 μm) was less than 15 min.

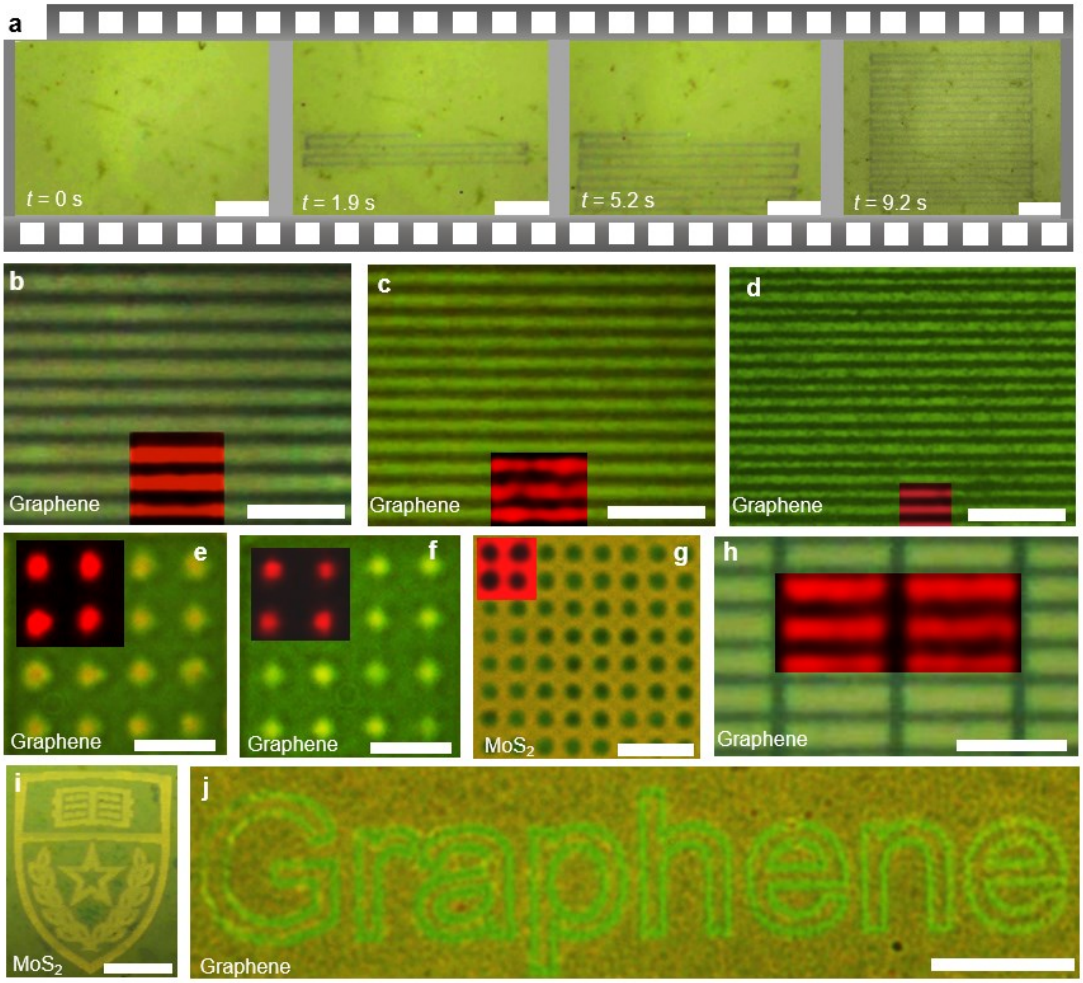

Figure 4.7: Versatile patterning capabilities of OTNL. (a) Sequential optical images of real-time patterning of 40 μm × 40 μm nanoribbon structures on graphene. The linewidth is 600 nm and the periodicity is 2 μm. (b-d) Graphene nanoribbon structures with a linewidth of (b) 950 nm, (c) 650 nm, and (d) 500 nm and a periodicity of (b) 1.6 μm, (c) 1.35 μm, and (d) 0.95 μm, respectively. (e, f) Graphene NDA with a diameter of (e) 1.8 μm, (f) 1.2 μm, (g) Nanohole array (NHA) with diameter in 1.1 μm patterned on MoS_2, and (h) graphene nanorectangle array with a geometry of 5 μm × 1 μm. (i) A UT Austin logo patterned on MoS_2. (j) "Graphene" text patterned on graphene. The linewidth is ~1.5 μm. The insets in (b-h) show the 2D Raman mapping images of (b-f) and (h) graphene (2D peak) and (g) MoS_2 (A_{1g}) in the corresponding areas. Red stands for high Raman intensity and black represents low Raman intensity. Scale bars: (a) 10 μm, (b-g) 5 μm, and (i, j) 50 μm.

It should be noted that the presence of AuNPs beneath the 2D materials can modify the intrinsic electrical and optical properties of the 2D materials, e.g., PL quenching.[254] However, this drawback can be significantly eliminated by the transfer of the patterned 2D materials to other non-plasmonic substrates (e.g., SiO_2/Si substrate, see Figure 4.8). Besides graphene and MoS2, OTNL can be applied to a variety of other 2D materials that can be ablated at the temperature generated by the thermoplasmonic substrate. As another demonstration, we have created a WSe2 grating structure at an optical power of 5 mW/μm^2 (Figure 4.9).

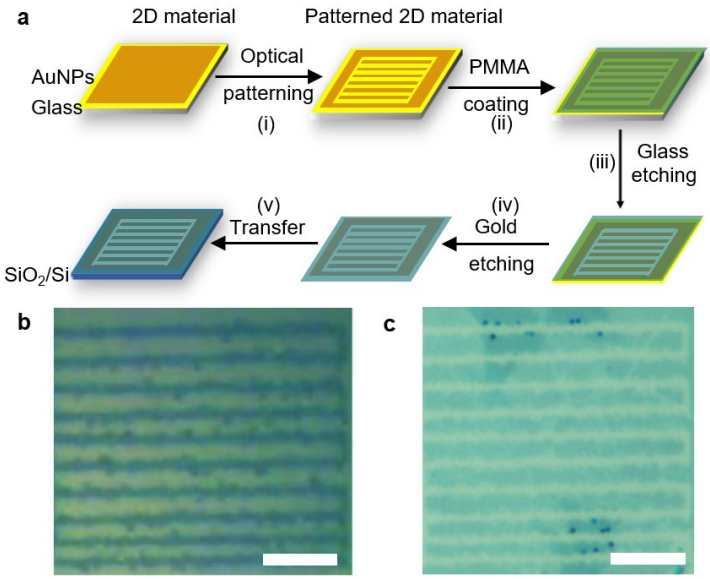

Figure 4.8: Transfer of the patterned 2D materials. (a) Schematic showing the transfer process of the patterned 2D materials from thermoplasmonic substrate to SiO_2/Si substrate. i) Optical patterning of 2D materials; ii) PMMA coating; iii) glass etching by HF solution; iv) gold etching by KI/I_2 solution; and v) transfer to SiO_2/Si substrate. Optical images of the same MoS_2 grating structure on (b) thermoplasmonic substrate and (c) SiO_2/Si substrate. Scale bars: 5 μm.

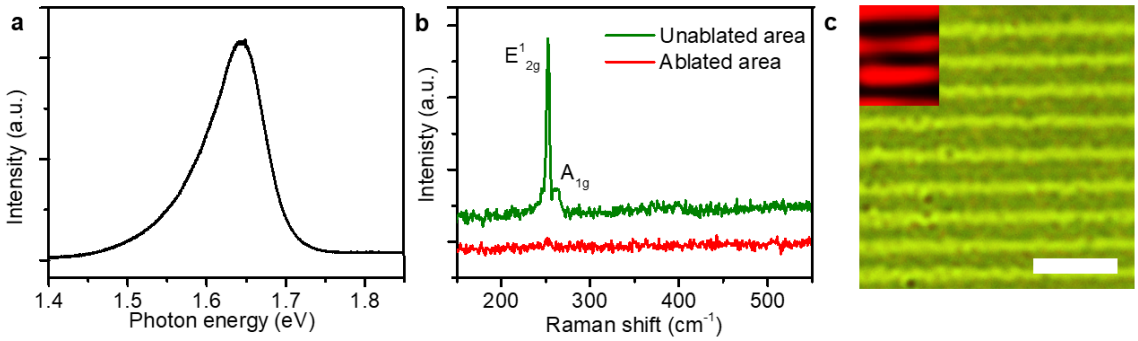

Figure 4.9: Patterning of WSe_2 via OTNL. (a) PL spectrum of WSe_2. (b) Raman spectra of WSe_2 recorded at different areas. (c) Optical image showing the patterned WSe_2 grating structure. The inset shows the Raman mapping of E_{2g} peak of WSe_2 in the corresponding area. Red stands for high Raman intensity and black represents low Raman intensity. Scale bar: 5 μm

We have developed OTNL for on-demand and high-throughput patterning of different 2D materials through coordinated management of both plasmon-enhanced optothermal response and the heat-matter interaction in the optically controlled temperature field. Our experiments and simulations reveal that thermal oxidation and gold catalysis are responsive for the low-power patterning of graphene, while MoS_2 patterning is an oxygenirrelevant process, i.e., lattice sublimation. Taking advantage of the localized thermal hotspots confined by the high-density AuNPs and the flexible management of light, we have demonstrated high-resolution patterning of arbitrary 2D patterns. Although the optical patterning requires a thermoplasmonic substrate, the patterned 2D materials can be easily transferred to alternative substrates by selective etching of the Au layer. Though our experiments demonstrated patterning of graphene, MoS_2, and WSe_2 monolayers, OTNL can be applied to various 2D materials for the fabrication of 2D nanostructures with precise control for diverse applications. For example, the optical patterning of graphene nanostructures will facilitate the development of terahertz photonic devices for applications

in biosensing and photon detection. In addition, the patterning of semiconductor 2D materials will find applications in 2D electronic devices such as field-effect transistors.

Chapter 5: Outlook[§§]

As an entropically favorable process, optothermal conversion provides a convenient and efficient way to regulate the temperature field and opto-thermo-matter interactions for on-demand control of nanomaterials. Optothermal approaches are developed to assemble nanoparticles into functional colloidal nanostructures on the substrate and to lithographically pattern atomic 2D materials with high-resolution nanopatterns. The precise engineering of functional colloidal nanoparticles and 2D materials will have the potential to advance many fields in materials science, microelectronics, and photonics. Nevertheless, there remain several challenges and opportunities for the future development of this field.[255]

First, as bottom-up techniques, optothermal assembly of colloidal matter has the advantage of constructing architectural nanostructures at single-particle resolution. However, this feature also results in one of the most significant limitations of this method: low throughput. In comparison to top-down lithographic techniques that can define a large-scale pattern within seconds, optothermal assembly relies on the manipulation of single building blocks to build the superstructures, which is a relatively time-consuming process. To enhance the throughput of optothermal assembly, one could improve the efficiency in manipulating single colloidal particles by better understanding the manipulation mechanism and further optimizing the manipulation system. For instance, one can further optimize the laser wavelength, optics, and substrate quality in the OPN technique to achieve a more effective manipulation of colloidal particles on the solid substrate. An alternative way is to integrate a programmable spatial light modulator or digital

[§§] This chapter is reproduced from following review manuscript published:
J. Li, Y. Zheng. Optothermally Assembled Nanostructures. *Acc. Mater. Res.* **2021**, *2*, 352-363.
P. S. Kollipara[#], **J. Li**[#], Y. Zheng. Optical Patterning of Two-Dimensional Materials. *Research* **2020**, *2020*, 6581250.
J. Li is the first author or the co-first author of these papers.

micromirror device to achieve parallel control of multiple particles. Additionally, the incorporation of microfluidics into the optothermal assembly platform will provide an efficient approach to the continuous and automated assembly of colloidal structures in the liquid media.

Second, optothermal assembly has mainly been applied to assemble 2D structures. Although OTA has demonstrated the capability of 3D assembly with simple configurations, the versatile assembly of complex 3D structures remains elusive. This limitation comes from the challenge of realizing a stable trapping potential along the out-of-plane direction. Two approaches are proposed to achieve 3D optothermal manipulation of colloidal particles in the solution to overcome this limitation. One method is to integrate the optothermal substrate into an optical fiber to achieve a 3D manipulation of particles via on-demand control over the laser focus along the *z*-axis. The other approach uses the target particle as a self-heating source to achieve the manipulation along with all directions without the need for an optothermal substrate. Both methods can be extended to assemble more complex 3D structures. Other approaches to achieving a 3D optothermal assembly can involve the 3D engineering of the substrate and the integration of other forces, including optical forces and electric forces.

Third, for the fabrication and patterning of 2D materials, several opportunities and challenges remain in improving optical patterning in terms of precision, resolution, surface roughness, versatility, diversification, and execution.[256] For instance, to improve the resolution of optical patterning, plasmonic substrates can be engineered to focus optothermal nano-hotspots into prescribed geometry at sub-100nm resolution. Apart from visible and infrared radiation, UV rays can be used to pattern 2D materials with higher resolutions due to the much shorter wavelengths. In addition, single-step optical patterning techniques provide the flexibility and higher throughput that are unavailable in these

conventional patterning methods. The use of spatial light modulators or digital micromirror devices could split a single laser beam into multiple independent beams to further increase the scalability. Moreover, optical patterning technologies have mainly been focused on homogeneous 2D materials. The advanced optical patterning of 2D heterostructures will potentially be a new promising direction.

Finally, the versatile capability of the optothermal approaches is expected to stimulate more advances in a broad range of fields. For example, optothermal assembly can turn colloidal particles into nanostructures with tunable bonding strength and reconfigurable geometry. The easy integration of optical spectroscopy into the assembly system provides an effective tool for characterizing the optical properties and interparticle interactions in the assembled structures in situ. In addition, during the further development and optimization of optothermal assembly techniques, one will have tremendous opportunities to advance the fundamental understanding of colloidal sciences, surface chemistry, thermal science, photonics, and fluidics. Optothermal assembly techniques are also suitable for the fabrication of functional nanodevices with new functions and ultimate miniaturization. Similarly, the capability of producing high-quality 2D material nanostructures with well-defined geometries at high resolution is a critical requirement for fostering 2D material-based applications. For instance, the optical patterning of atomically thin 2D materials into finite structures with nanometer-scale confinement is important for tuning their electronic transport properties. Scaling of electronic devices to smaller dimensions also increases the device density and reduces power consumption for the development of new-generation microelectronic devices. With their advantages of wide applicability, site-specific control, and low damage to nanomaterials, optothermal approaches are promising for prototyping novel optical gratings, optical waveguides, optical circuits, topological nanostructures, and other photonic and electronic nanodevices.

References

(1) Mostafalu, P.; Sonkusale, S. Flexible and Transparent Gastric Battery: Energy Harvesting from Gastric Acid for Endoscopy Application. *Biosens. Bioelectron.* **2014,** *54*, 292-296.

(2) Wu, Z.-S.; Parvez, K.; Feng, X.; Mullen, K. Photolithographic Fabrication of High-Performance All-Solid-State Graphene-Based Planar Micro-Supercapacitors with Different Interdigital Fingers. *J. Mater. Chem. A* **2014,** *2*, 8288-8293.

(3) Han, K.-S.; Shin, J.-H.; Yoon, W.-Y.; Lee, H. Enhanced Performance of Solar Cells with Anti-Reflection Layer Fabricated by Nano-Imprint Lithography. *Sol. Energy Mater. Sol. Cells* **2011,** *95*, 288-291.

(4) Hoff, J. D.; Cheng, L.-J.; Meyhöfer, E.; Guo, L. J.; Hunt, A. J. Nanoscale Protein Patterning by Imprint Lithography. *Nano Lett.* **2004,** *4*, 853-857.

(5) Gonzalez-Macia, L.; Morrin, A.; Smyth, M. R.; Killard, A. J. Advanced Printing and Deposition Methodologies for the Fabrication of Biosensors and Biodevices. *Analyst* **2010,** *135*, 845-867.

(6) Lu, Y.; Chen, S. C. Micro and Nano-Fabrication of Biodegradable Polymers for Drug Delivery. *Adv. Drug Deliver. Rev.* **2004,** *56*, 1621-1633.

(7) Williams, B. S. Terahertz Quantum-Cascade Lasers. *Nat. Photonics* **2007,** *1*, 517-525.

(8) Makarenko, K. S.; Liu, Z.; Jong, M. P. d.; Zwanenburg, F. A.; Huskens, J.; van der Wiel, W. G. Bottom-up Single-Electron Transistors. *Adv. Mater.* **2017,** *29*, 1702920.

(9) Boto, A. N.; Kok, P.; Abrams, D. S.; Braunstein, S. L.; Williams, C. P.; Dowling, J. P. Quantum Interferometric Optical Lithography: Exploiting Entanglement to Beat the Diffraction Limit. *Phys. Rev. Lett.* **2000,** *85*, 2733-2736.

(10) Saavedra, H. M.; Mullen, T. J.; Zhang, P.; Dewey, D. C.; Claridge, S. A.; Weiss, P. S. Hybrid Strategies in Nanolithography. *Rep. Prog. Phys.* **2010,** *73*, 036501.

(11) Vieu, C.; Carcenac, F.; Pepin, A.; Chen, Y.; Mejias, M.; Lebib, A.; Manin-Ferlazzo, L.; Couraud, L.; Launois, H. Electron Beam Lithography: Resolution Limits and Applications. *Appl. Surf. Sci.* **2000,** *164*, 111-117.

(12) Xia, Y. W.; M., G. Soft Lithography. *Annu. Rev. Mater. Sci.* **1998,** *28*, 153-184.

(13) Guo, L. J. Nanoimprint Lithography: Methods and Material Requirements. *Adv. Mater.* **2007,** *19*, 495-513.

(14) Whitesides, G. M.; Grzybowski, B. Self-Assembly at All Scales. *Science* **2002,** *295*, 2418-2421.

(15) Vogel, N.; Retsch, M.; Fustin, C.-A.; del Campo, A.; Jonas, U. Advances in Colloidal Assembly: The Design of Structure and Hierarchy in Two and Three Dimensions. *Chem. Rev.***2015,** *115*, 6265-6311.

(16) Zhang, M.; Magagnosc, D. J.; Liberal, I.; Yu, Y.; Yun, H.; Yang, H.; Wu, Y.; Guo, J.; Chen, W.; Shin, Y. J.; Stein, A.; Kikkawa, J. M.; Engheta, N.; Gianola, D. S.; Murray, C. B.; Kagan, C. R. High-Strength Magnetically Switchable Plasmonic Nanorods Assembled from a Binary Nanocrystal Mixture. *Nat. Nanotechnol.* **2017,** *12*, 228-232.

(17) Greybush, N. J.; Saboktakin, M.; Ye, X.; Della Giovampaola, C.; Oh, S. J.; Berry, N. E.; Engheta, N.; Murray, C. B.; Kagan, C. R. Plasmon-Enhanced Upconversion Luminescence in Single Nanophosphor–Nanorod Heterodimers Formed through Template-Assisted Self-Assembly. *ACS Nano* **2014,** *8*, 9482-9491.

(18) Calvert, P. Inkjet Printing for Materials and Devices. *Chem. Mater.* **2001,** *13*, 3299-3305.

(19) Piner, R. D.; Zhu, J.; Xu, F.; Hong, S.; Mirkin, C. A. "Dip-Pen" Nanolithography. *Science* **1999,** *283*, 661-663.

(20) Urban, A. S.; Lutich, A. A.; Stefani, F. D.; Feldmann, J. Laser Printing Single Gold Nanoparticles. *Nano Lett.* **2010,** *10*, 4794-4798.

(21) Stohr, R. J.; Kolesov, R.; Xia, K.; Wrachtrup, J. All-Optical High-Resolution Nanopatterning and 3d Suspending of Graphene. *ACS Nano* **2011,** *5*, 5141-5150.

(22) Lin, L.; Hill, E. H.; Peng, X.; Zheng, Y. Optothermal Manipulations of Colloidal Particles and Living Cells. *Acc. Chem. Res.* **2018,** *51*, 1465-1474.

(23) Shen, X.; Asenjo-Garcia, A.; Liu, Q.; Jiang, Q.; Garcia de Abajo, F. J.; Liu, N.; Ding, B. Three-Dimensional Plasmonic Chiral Tetramers Assembled by DNA Origami. *Nano Lett.* **2013,** *13*, 2128-2133.

(24) Cecconello, A.; Besteiro, L. V.; Govorov, A. O.; Willner, I. Chiroplasmonic DNA-Based Nanostructures. *Nat. Rev. Mater.* **2017,** *2*, 17039.

(25) Maier, S. A.; Brongersma, M. L.; Kik, P. G.; Meltzer, S.; Requicha, A. A. G.; Atwater, H. A. Plasmonics—a Route to Nanoscale Optical Devices. *Adv. Mater.* **2001,** *13*, 1501-1505.

(26) Shi, J.; Monticone, F.; Elias, S.; Wu, Y.; Ratchford, D.; Li, X.; Alu, A. Modular Assembly of Optical Nanocircuits. *Nat. Commun.* **2014,** *5*, 3896.

(27) Xu, B. B.; Zhang, R.; Wang, H.; Liu, X. Q.; Wang, L.; Ma, Z. C.; Chen, Q. D.; Xiao, X. Z.; Han, B.; Sun, H. B. Laser Patterning of Conductive Gold Micronanostructures from Nanodots. *Nanoscale* **2012,** *4*, 6955-6958.

(28) Xu, B.-B.; Zhang, Y.-L.; Zhang, R.; Wang, L.; Xiao, X.-Z.; Xia, H.; Chen, Q.-D.; Sun, H.-B. Programmable Assembly of CdTe Quantum Dots into

Microstructures by Femtosecond Laser Direct Writing. *J. Mater. Chem. C* **2013,** *1*, 4699-4704.

(29) Jamshidi, A.; Neale, S. L.; Yu, K.; Pauzauskie, P. J.; Schuck, P. J.; Valley, J. K.; Hsu, H. Y.; Ohta, A. T.; Wu, M. C. Nanopen: Dynamic, Low-Power, and Light-Actuated Patterning of Nanoparticles. *Nano Lett.* **2009,** *9*, 2921-2925.

(30) Zywietz, U.; Evlyukhin, A. B.; Reinhardt, C.; Chichkov, B. N. Laser Printing of Silicon Nanoparticles with Resonant Optical Electric and Magnetic Responses. *Nat. Commun.* **2014,** *5*, 3402.

(31) Alam, M. S.; Zhan, Q.; Zhao, C. Additive Opto-Thermomechanical Nanoprinting and Nanorepairing under Ambient Conditions. *Nano Lett.* **2020,** *20*, 5057-5064.

(32) Lin, L.; Peng, X.; Mao, Z.; Li, W.; Yogeesh, M. N.; Rajeeva, B. B.; Perillo, E. P.; Dunn, A. K.; Akinwande, D.; Zheng, Y. Bubble-Pen Lithography. *Nano Lett.* **2016,** *16*, 701-708.

(33) Walker, D.; Singh, D. P.; Fischer, P. Capture of 2D Microparticle Arrays Via a Uv-Triggered Thiol-yne "Click" Reaction. *Adv. Mater.* **2016,** *28*, 9846-9850.

(34) Piazza, R.; Guarino, A. Soret Effect in Interacting Micellar Solutions. *Phys. Rev. Lett.* **2002,** *88*, 208302.

(35) Piazza, R.; Parola, A. Thermophoresis in Colloidal Suspensions. *J. Phys.: Condens. Matter* **2008,** *20*, 153102.

(36) Li, J.; Lin, L.; Inoue, Y.; Zheng, Y. Opto-Thermophoretic Tweezers and Assembly. *J. Micro Nano-Manuf.* **2018,** *6*, 040801.

(37) Parola, A.; Piazza, R. Particle Thermophoresis in Liquids. *Eur. Phys. J. E* **2004,** *15*, 255-263.

(38) Würger, A. Transport in Charged Colloids Driven by Thermoelectricity. *Phys. Rev. Lett.* **2008,** *101*, 108302.

(39) Würger, A. Thermal Non-Equilibrium Transport in Colloids. *Rep. Prog. Phys.* **2010,** *73*, 126601.

(40) Pughazhendi, A.; Chen, Z.; Wu, Z.; Li, J.; Zheng, Y. Opto-Thermoelectric Tweezers: Principles and Applications. *Front. Phys.* **2020,** *8*, 580014.

(41) Guthrie Jr, G.; Wilson, J. N.; Schomaker, V. Theory of the Thermal Diffusion of Electrolytes in a Clusius Column. *J. Chem. Phys.* **1949,** *17*, 310-313.

(42) Reichl, M.; Herzog, M.; Götz, A.; Braun, D. Why Charged Molecules Move across a Temperature Gradient: The Role of Electric Fields. *Phys. Rev. Lett.* **2014,** *112*, 198101.

(43) Anderson, J. L. Colloid Transport by Interfacial Forces. *Annu. Rev. Fluid Mech.* **1989,** *21*, 61-99.

(44) Jovanovic, O. Photophoresis-Light Induced Motion of Particles Suspended in Gas. *J. Quant. Spectrosc. Radiat. Transf.* **2009,** *110*, 889-901.

(45) Gong, Z.; Pan, Y.-L.; Videen, G.; Wang, C. Optical Trapping and Manipulation of Single Particles in Air: Principles, Technical Details, and Applications. *J. Quant. Spectrosc. Radiat. Transf.* **2018,** *214*, 94-119.

(46) Donner, J. S.; Baffou, G.; McCloskey, D.; Quidant, R. Plasmon-Assisted Optofluidics. *ACS Nano* **2011,** *5*, 5457-5462.

(47) Scriven, L.; Sternling, C. The Marangoni Effects. *Nature* **1960,** *187*, 186-188.

(48) Ndukaife, J. C.; Kildishev, A. V.; Nnanna, A. G. A.; Shalaev, V. M.; Wereley, S. T.; Boltasseva, A. Long-Range and Rapid Transport of Individual Nano-Objects by a Hybrid Electrothermoplasmonic Nanotweezer. *Nature Nanotechnology* **2016,** *11*, 53-59.

(49) Kotnala, A.; Kollipara, P. S.; Li, J.; Zheng, Y. Overcoming Diffusion-Limited Trapping in Nanoaperture Tweezers Using Opto-Thermal-Induced Flow. *Nano Lett.* **2020,** *20*, 768-779.

(50) Han, B.; Zhang, Y. L.; Chen, Q. D.; Sun, H. B. Carbon‐Based Photothermal Actuators. *Adv. Funct. Mater.* **2018,** *28*, 1802235.

(51) Li, J.; Zhou, X.; Liu, Z. Recent Advances in Photoactuators and Their Applications in Intelligent Bionic Movements. *Adv. Opt. Mater.* **2020,** *8*, 2000886.

(52) Linghu, S.; Gu, Z.; Lu, J.; Fang, W.; Yang, Z.; Yu, H.; Li, Z.; Zhu, R.; Peng, J.; Zhan, Q.; Zhuang, S.; Gu, M.; Gu, F. Plasmon-Driven Nanowire Actuators for on-Chip Manipulation. *Nat. Commun.* **2021,** *12*, 385.

(53) Duhr, S.; Braun, D. Why Molecules Move Along a Temperature Gradient. *Proc. Natl. Acad. Sci. U. S. A.* **2006,** *103*, 19678-19682.

(54) Braun, M.; Cichos, F. Optically Controlled Thermophoretic Trapping of Single Nano-Objects. *ACS Nano* **2013,** *7*, 11200-11208.

(55) Braun, M.; Bregulla, A. P.; Günther, K.; Mertig, M.; Cichos, F. Single Molecules Trapped by Dynamic Inhomogeneous Temperature Fields. *Nano Lett.* **2015,** *15*, 5499-5505.

(56) Lin, L.; Peng, X.; Mao, Z.; Wei, X.; Xie, C.; Zheng, Y. Interfacial-Entropy-Driven Thermophoretic Tweezers. *Lab Chip* **2017,** *17*, 3061-3070.

(57) Kang, Z.; Chen, J.; Wu, S.-Y.; Chen, K.; Kong, S.-K.; Yong, K.-T.; Ho, H.-P. Trapping and Assembling of Particles and Live Cells on Large-Scale Random Gold Nano-Island Substrates. *Sci. Rep.* **2015,** *5*, 9978.

(58) Chen, J.; Cong, H.; Loo, F.-C.; Kang, Z.; Tang, M.; Zhang, H.; Wu, S.-Y.; Kong, S.-K.; Ho, H.-P. Thermal Gradient Induced Tweezers for the Manipulation of Particles and Cells. *Sci. Rep.***2016,** *6*, 35814.

(59) Lin, L.; Peng, X.; Wei, X.; Mao, Z.; Xie, C.; Zheng, Y. Thermophoretic Tweezers for Low-Power and Versatile Manipulation of Biological Cells. *ACS Nano* **2017,** *11*, 3147-3154.

(60) Hill, E. H.; Li, J.; Lin, L.; Liu, Y.; Zheng, Y. Opto-Thermophoretic Attraction, Trapping, and Dynamic Manipulation of Lipid Vesicles. *Langmuir* **2018,** *34*, 13252-13262.

(61) Lin, L.; Wang, M.; Peng, X.; Lissek, E. N.; Mao, Z.; Scarabelli, L.; Adkins, E.; Coskun, S.; Unalan, H. E.; Korgel, B. A.; Liz-Marzan, L. M.; Florin, E. L.; Zheng, Y. Opto-Thermoelectric Nanotweezers. *Nat. Photonics* **2018,** *12*, 195-201.

(62) Lin, L.; Zhang, J.; Peng, X.; Wu, Z.; Coughlan, A. C. H.; Mao, Z.; Bevan, M. A.; Zheng, Y. Opto-Thermophoretic Assembly of Colloidal Matter. *Sci. Adv.* **2017,** *3*, e1700458.

(63) Peng, X. L.; Li, J. G.; Lin, L. H.; Liu, Y. R.; Zheng, Y. B. Opto-Thermophoretic Manipulation and Construction of Colloidal Superstructures in Photocurable Hydrogels. *ACS Appl. Nano Mater.* **2018,** *1*, 3998-4004.

(64) Grier, D. G. A Revolution in Optical Manipulation. *Nature* **2003,** *424*, 810-816.

(65) Ashkin, A. Acceleration and Trapping of Particles by Radiation Pressure. *Phys. Rev. Lett.* **1970,** *24*, 156-159.

(66) Ashkin, A.; Dziedzic, J. M.; Yamane, T. Optical Trapping and Manipulation of Single Cells Using Infrared Laser Beams. *Nature* **1987,** *330*, 769-771.

(67) Maragò, O. M.; Jones, P. H.; Gucciardi, P. G.; Volpe, G.; Ferrari, A. C. Optical Trapping and Manipulation of Nanostructures. *Nat. Nanotechnol.* **2013,** *8*, 807.

(68) McLeod, E.; Arnold, C. B. Subwavelength Direct-Write Nanopatterning Using Optically Trapped Microspheres. *Nat. Nanotechnol.* **2008,** *3*, 413-417.

(69) Chu, S.; Bjorkholm, J. E.; Ashkin, A.; Cable, A. Experimental Observation of Optically Trapped Atoms. *Phys. Rev. Lett.* **1986,** *57*, 314-317.

(70) Gustavson, T. L.; Chikkatur, A. P.; Leanhardt, A. E.; Görlitz, A.; Gupta, S.; Pritchard, D. E.; Ketterle, W. Transport of Bose-Einstein Condensates with Optical Tweezers. *Phys. Rev. Lett.* **2001,** *88*, 020401.

(71) Han, F.; Parker, J. A.; Yifat, Y.; Peterson, C.; Gray, S. K.; Scherer, N. F.; Yan, Z. Crossover from Positive to Negative Optical Torque in Mesoscale Optical Matter. *Nat. Commun.* **2018,** *9*, 4897.

(72) Yan, Z.; Sajjan, M.; Scherer, N. F. Fabrication of a Material Assembly of Silver Nanoparticles Using the Phase Gradients of Optical Tweezers. *Phys. Rev. Lett.* **2015,** *114*, 143901.

(73) Ashkin, A.; Dziedzic, J. M. Optical Trapping and Manipulation of Viruses and Bacteria. *Science* **1987,** *235*, 1517-1520.

(74) Moffitt, J. R.; Chemla, Y. R.; Smith, S. B.; Bustamante, C. Recent Advances in Optical Tweezers. *Annu. Rev. Biochem.* **2008,** *77*, 205-228.

(75) Grigorenko, A. N.; Roberts, N. W.; Dickinson, M. R.; Zhang, Y. Nanometric Optical Tweezers Based on Nanostructured Substrates. *Nat. Photonics* **2008,** *2*, 365.

(76) Blázquez-Castro, A. Optical Tweezers: Phototoxicity and Thermal Stress in Cells and Biomolecules. *Micromachines* **2019,** *10*, 507.

(77) Babynina, A.; Fedoruk, M.; Kühler, P.; Meledin, A.; Döblinger, M.; Lohmüller, T. Bending Gold Nanorods with Light. *Nano Lett.* **2016,** *16*, 6485-6490.

(78) Rasmussen, M. B.; Oddershede, L. B.; Siegumfeldt, H. Optical Tweezers Cause Physiological Damage to Escherichia Coli and Listeria Bacteria. *Appl. Environ. Microbiol.* **2008,** *74*, 2441-2446.

(79) Juan, M. L.; Righini, M.; Quidant, R. Plasmon Nano-Optical Tweezers. *Nat. Photonics* **2011,** *5*, 349-356.

(80) Kotnala, A.; Gordon, R. Quantification of High-Efficiency Trapping of Nanoparticles in a Double Nanohole Optical Tweezer. *Nano Lett.* **2014,** *14*, 853-856.

(81) Pang, Y.; Gordon, R. Optical Trapping of a Single Protein. *Nano Lett.* **2012,** *12*, 402-406.

(82) Chiou, P. Y.; Ohta, A. T.; Wu, M. C. Massively Parallel Manipulation of Single Cells and Microparticles Using Optical Images. *Nature* **2005,** *436*, 370-372.

(83) Wu, M. C. Optoelectronic Tweezers. *Nat. Photonics* **2011,** *5*, 322-324.

(84) Liu, Y.; Lin, L.; Bangalore Rajeeva, B.; Jarrett, J. W.; Li, X.; Peng, X.; Kollipara, P.; Yao, K.; Akinwande, D.; Dunn, A. K.; Zheng, Y. Nanoradiator-Mediated Deterministic Opto-Thermoelectric Manipulation. *ACS Nano* **2018,** *12*, 10383-10392.

(85) Hong, C.; Yang, S.; Ndukaife, J. C. Stand-Off Trapping and Manipulation of Sub-10 Nm Objects and Biomolecules Using Opto-Thermo-Electrohydrodynamic Tweezers. *Nat. Nanotechnol.* **2020,** *15*, 908-913.

(86) Li, J.; Chen, Z.; Liu, Y.; Kollipara, P. S.; Feng, Y.; Zhang, Z.; Zheng, Y. Opto-Refrigerative Tweezers. *Sci. Adv.* **2021,** *7*, eabh1101.

(87) Roder, P. B.; Smith, B. E.; Zhou, X.; Crane, M. J.; Pauzauskie, P. J. Laser Refrigeration of Hydrothermal Nanocrystals in Physiological Media. *Proc. Natl. Acad. Sci. U. S. A.* **2015,** *112*, 15024-15029.

(88) Zhou, X.; Smith, B. E.; Roder, P. B.; Pauzauskie, P. J. Laser Refrigeration of Ytterbium-Doped Sodium-Yttrium-Fluoride Nanowires. *Adv. Mater.* **2016,** *28*, 8658-8662.

(89) Seletskiy, D. V.; Melgaard, S. D.; Bigotta, S.; Di Lieto, A.; Tonelli, M.; Sheik-Bahae, M. Laser Cooling of Solids to Cryogenic Temperatures. *Nat. Photonics* **2010**.

(90) Rahman, A. T. M. A.; Barker, P. F. Laser Refrigeration, Alignment and Rotation of Levitated Yb^{3+}:YLF Nanocrystals. *Nat. Photonics* **2017,** *11*, 634-638.

(91) Zhang, J.; Li, D.; Chen, R.; Xiong, Q. Laser Cooling of a Semiconductor by 40 Kelvin. *Nature* **2013,** *493*, 504-508.

(92) Vetrone, F.; Naccache, R.; Zamarrón, A.; Juarranz de la Fuente, A.; Sanz-Rodríguez, F.; Martinez Maestro, L.; Martín Rodriguez, E.; Jaque, D.; García Solé, J.; Capobianco, J. A. Temperature Sensing Using Fluorescent Nanothermometers. *ACS Nano* **2010,** *4*, 3254-3258.

(93) Burelbach, J.; Zupkauskas, M.; Lamboll, R.; Lan, Y.; Eiser, E. Colloidal Motion under the Action of a Thermophoretic Force. *J. Chem. Phys.* **2017,** *147*, 094906.

(94) Maeda, Y. T.; Buguin, A.; Libchaber, A. Thermal Separation: Interplay between the Soret Effect and Entropic Force Gradient. *Phys. Rev. Lett.* **2011,** *107*, 038301.

(95) Florin, E. L.; Pralle, A.; Stelzer, E. H. K.; Hörber, J. K. H. Photonic Force Microscope Calibration by Thermal Noise Analysis. *Appl. Phys. A* **1998,** *66*, S75-S78.

(96) Chirico, G.; Cannone, F.; Baldini, G.; Diaspro, A. Two-Photon Thermal Bleaching of Single Fluorescent Molecules. *Biophysical Journal* **2003,** *84*, 588-598.

(97) Matthews, B. W.; Nicholson, H.; Becktel, W. J. Enhanced Protein Thermostability from Site-Directed Mutations That Decrease the Entropy of Unfolding. *Proc. Natl. Acad. Sci. U. S. A.* **1987,** *84*, 6663-6667.

(98) Lee, G.; Bratkowski, M. A.; Ding, F.; Ke, A.; Ha, T. Elastic Coupling between Rna Degradation and Unwinding by an Exoribonuclease. *Science* **2012,** *336*, 1726-1729.

(99) Liu, C.; Zhao, J.; Tian, F.; Cai, L.; Zhang, W.; Feng, Q.; Chang, J.; Wan, F.; Yang, Y.; Dai, B.; Cong, Y.; Ding, B.; Sun, J.; Tan, W. Low-Cost Thermophoretic Profiling of Extracellular-Vesicle Surface Proteins for the Early Detection and Classification of Cancers. *Nat. Biomed. Eng.* **2019,** *3*, 183-193.

(100) Wienken, C. J.; Baaske, P.; Rothbauer, U.; Braun, D.; Duhr, S. Protein-Binding Assays in Biological Liquids Using Microscale Thermophoresis. *Nat. Commun.* **2010,** *1*, 100.

(101) Jiang, Q.; Rogez, B.; Claude, J.-B.; Baffou, G.; Wenger, J. Quantifying the Role of the Surfactant and the Thermophoretic Force in Plasmonic Nano-Optical Trapping. *Nano Lett.* **2020,** *20*, 8811-8817.

(102) Yang, H.; Jiang, P. Large-Scale Colloidal Self-Assembly by Doctor Blade Coating. *Langmuir* **2010,** *26*, 13173-13182.

(103) Talapin, D. V.; Lee, J. S.; Kovalenko, M. V.; Shevchenko, E. V. Prospects of Colloidal Nanocrystals for Electronic and Optoelectronic Applications. *Chem. Rev.* **2010,** *110*, 389-458.

(104) Kim, J. W.; Larsen, R. J.; Weitz, D. A. Synthesis of Nonspherical Colloidal Particles with Anisotropic Properties. *J. Am. Chem. Soc.* **2006,** *128*, 14374-14377.

(105) Gonzalez-Rubio, G.; Guerrero-Martinez, A.; Liz-Marzan, L. M. Reshaping, Fragmentation, and Assembly of Gold Nanoparticles Assisted by Pulse Lasers. *Acc. Chem. Res.* **2016,** *49*, 678-686.

(106) Matijevic, E. Production of Monodispersed Colloidal Particles. *Annu. Rev. Mater. Sci.* **1985,** *15*, 483-516.

(107) Ye, X.; Jin, L.; Caglayan, H.; Chen, J.; Xing, G.; Zheng, C.; Doan-Nguyen, V.; Kang, Y.; Engheta, N.; Kagan, C. R.; Murray, C. B. Improved Size-Tunable Synthesis of Monodisperse Gold Nanorods through the Use of Aromatic Additives. *ACS Nano* **2012,** *6*, 2804-2817.

(108) Wilson, B. K.; Mentele, T.; Bachar, S.; Knouf, E.; Bendoraite, A.; Tewari, M.; Pun, S. H.; Lin, L. Y. Nanostructure-Enhanced Laser Tweezers for Efficient Trapping and Alignment of Particles. *Opt. Express* **2010,** *18*, 16005-16013.

(109) Li, J.; Hill, E. H.; Lin, L.; Zheng, Y. Optical Nanoprinting of Colloidal Particles and Functional Structures. *ACS Nano* **2019,** *13*, 3783-3795.

(110) Ni, S.; Leemann, J.; Buttinoni, I.; Isa, L.; Wolf, H. Programmable Colloidal Molecules from Sequential Capillarity-Assisted Particle Assembly. *Sci. Adv.* **2016,** *2*, e1501779.

(111) Chini, S. F.; Amirfazli, A. Understanding Pattern Collapse in Photolithography Process Due to Capillary Forces. *Langmuir* **2010,** *26*, 13707-13714.

(112) Jones, S.; Andren, D.; Karpinski, P.; Kall, M. Photothermal Heating of Plasmonic Nanoantennas: Influence on Trapped Particle Dynamics and Colloid Distribution. *ACS Photonics* **2018,** *5*, 2878-2887.

(113) Do, J.; Fedoruk, M.; Jackel, F.; Feldmann, J. Two-Color Laser Printing of Individual Gold Nanorods. *Nano Lett.* **2013,** *13*, 4164-4168.

(114) Requicha, A. A. G. Nanorobots, Nems, and Nanoassembly. *Proc. IEEE* **2003,** *91*, 1922-1933.

(115) Schaefer, D. M.; Reifenberger, R.; Patil, A.; Andres, R. P. Fabrication of Two-Dimensional Arrays of Nanometer-Size Clusters with the Atomic Force Microscope. *Appl. Phys. Lett.* **1995,** *66*, 1012-1014.

(116) Junno, T.; Deppert, K.; Montelius, L.; Samuelson, L. Controlled Manipulation of Nanoparticles with an Atomic-Force Microscope. *Appl. Phys. Lett.* **1995,** *66*, 3627-3629.

(117) Wang, Y. R.; Zheng, R. Q.; Ding, Y. F.; Fan, W. J.; Liu, D. H.; Zhou, J.; Shi, J. W. Resolving the Bond Angle of a Plasmonic Metamolecule. *Optica* **2017,** *4*, 1092-1097.

(118) Nosonovsky, M. Model for Solid-Liquid and Solid-Solid Friction of Rough Surfaces with Adhesion Hysteresis. *J. Chem. Phys.* **2007,** *126*, 224701.

(119) Sitti, M. Atomic Force Microscope Probe Based Controlled Pushing for Nanotribological Characterization. *IEEE/ASME Trans. Mechatronics* **2004,** *9*, 343-349.

(120) Selmke, M.; Khadka, U.; Bregulla, A. P.; Cichos, F.; Yang, H. Theory for Controlling Individual Self-Propelled Micro-Swimmers by Photon Nudging I: Directed Transport. *Phys. Chem. Chem. Phys.* **2018,** *20*, 10502-10520.

(121) Qian, B.; Montiel, D.; Bregulla, A.; Cichos, F.; Yang, H. Harnessing Thermal Fluctuations for Purposeful Activities: The Manipulation of Single Micro-Swimmers by Adaptive Photon Nudging. *Chem. Sci.* **2013,** *4*, 1420-1429.

(122) Tian, Y. C.; Yu, J.; Gu, M.; Lian, Y. D.; Ai, X. Q.; Tang, T. B. Impedance Spectroscopic Study on Rotator and Disordered Phases in Trimethylammonium Chlorides. *J. Phys. Chem. C* **2016,** *120*, 23905-23909.

(123) Bezrodna, T.; Puchkoyska, G.; Styopkin, V.; Baran, J.; Drozd, M.; Danchuk, V.; Kraychuk, A. Ir-Study of Thermotropic Phase Transitions in Cetyltrimethylammonium Bromide Powder and Film. *J. Mol. Struct.* **2010,** *973*, 47-55.

(124) Lin, L. H.; Li, J. G.; Li, W.; Yogeesh, M. N.; Shi, J. J.; Peng, X. L.; Liu, Y. R.; Rajeeva, B. B.; Becker, M. F.; Liu, Y. Y.; Akinwande, D.; Zheng, Y. B. Optothermoplasmonic Nanolithography for on-Demand Patterning of 2D Materials. *Adv. Funct. Mater.* **2018,** *28*, 1803990.

(125) Zhao, Y.; Li, C. Z.; Liu, X. H.; Gu, F.; Jiang, H. B.; Shao, W.; Zhang, L.; He, Y. Synthesis and Optical Properties of TiO_2 Nanoparticles. *Mater. Lett.* **2007,** *61*, 79-83.

(126) Li, T.; Zhou, C. L.; Jiang, M. Uv Absorption-Spectra of Polystyrene. *Polym. Bull.* **1991,** *25*, 211-216.

(127) Knight, M. W.; King, N. S.; Liu, L.; Everitt, H. O.; Nordlander, P.; Halas, N. J. Aluminum for Plasmonics. *ACS Nano* **2014,** *8*, 834-840.

(128) Zhigunov, D. M.; Evlyukhin, A. B.; Shalin, A. S.; Zywietz, U.; Chichkov, B. N. Femtosecond Laser Printing of Single Ge and SiGe Nanoparticles with Electric and Magnetic Optical Resonances. *ACS Photonics* **2018,** *5*, 977-983.

(129) Person, S.; Jain, M.; Lapin, Z.; Saenz, J. J.; Wicks, G.; Novotny, L. Demonstration of Zero Optical Backscattering from Single Nanoparticles. *Nano Lett.* **2013,** *13*, 1806-1809.

(130) Renaut, C.; Lang, L.; Frizyuk, K.; Timofeeva, M.; Komissarenko, F. E.; Mukhin, I. S.; Smirnova, D.; Timpu, F.; Petrov, M.; Kivshar, Y.; Grange, R. Reshaping the Second-Order Polar Response of Hybrid Metal-Dielectric Nanodimers. *Nano Lett.* **2019,** *19*, 877-884.

(131) Kralchevsky, P. A.; Nagayama, K. Capillary Interactions between Particles Bound to Interfaces, Liquid Films and Biomembranes. *Adv. Colloid. Interfaces* **2000,** *85*, 145-192.

(132) Petkov, J. T.; Danov, K. D.; Denkov, N. D.; Aust, R.; Durst, F. Precise Method for Measuring the Shear Surface Viscosity of Surfactant Monolayers. *Langmuir* **1996,** *12*, 2650-2653.

(133) Scarabelli, L.; Coronado-Puchau, M.; Giner-Casares, J. J.; Langer, J.; Liz-Marzan, L. M. Monodisperse Gold Nanotriangles: Size Control, Large-Scale Self-Assembly, and Performance in Surface-Enhanced Raman Scattering. *ACS Nano* **2014,** *8*, 5833-5842.

(134) Huang, F.; Baumberg, J. J. Actively Tuned Plasmons on Elastomerically Driven Au Nanoparticle Dimers. *Nano Lett.* **2010,** *10*, 1787-1792.

(135) Lin, L. H.; Lepeshov, S.; Krasnok, A.; Jiang, T. Z.; Peng, X. L.; Korgel, B. A.; Alu, A.; Zheng, Y. B. All-Optical Reconfigurable Chiral Meta-Molecules. *Mater. Today* **2019,** *25*, 10-20.

(136) Tiguntseva, E. Y.; Baranov, D. G.; Pushkarev, A. P.; Munkhbat, B.; Komissarenko, F.; Franckevicius, M.; Zakhidov, A. A.; Shegai, T.; Kivshar, Y. S.; Makarov, S. V. Tunable Hybrid Fano Resonances in Halide Perovskite Nanoparticles. *Nano Lett.* **2018,** *18*, 5522-5529.

(137) Tiguntseva, E. Y.; Zograf, G. P.; Komissarenko, F. E.; Zuev, D. A.; Zakhidov, A. A.; Makarov, S. V.; Kivshar, Y. S. Light-Emitting Halide Perovskite Nanoantennas. *Nano Lett.* **2018,** *18*, 1185-1190.

(138) Guler, U.; Suslov, S.; Kildishev Alexander, V.; Boltasseva, A.; Shalaev Vladimir, M. Colloidal Plasmonic Titanium Nitride Nanoparticles: Properties and Applications. *Nanophotonics* **2015,** *4*, 269.

(139) Hu, C.; Pané, S.; Nelson, B. J. Soft Micro- and Nanorobotics. *Annu. rev. control robot. auton. syst.* **2018,** *1*, 53-75.

(140) Novotný, F.; Wang, H.; Pumera, M. Nanorobots: Machines Squeezed between Molecular Motors and Micromotors. *Chem* **2020,** *6*, 867-884.

(141) Li, J.; Gao, W.; Dong, R.; Pei, A.; Sattayasamitsathit, S.; Wang, J. Nanomotor Lithography. *Nat. Commun.* **2014,** *5*, 5026.

(142) Manesh, K. M.; Balasubramanian, S.; Wang, J. Nanomotor-Based 'Writing' of Surface Microstructures. *Chem. Commun.* **2010,** *46*, 5704-5706.

(143) Wang, J.; Gao, W. Nano/Microscale Motors: Biomedical Opportunities and Challenges. *ACS Nano* **2012,** *6*, 5745-5751.

(144) Li, J.; Esteban-Fernández de Ávila, B.; Gao, W.; Zhang, L.; Wang, J. Micro/Nanorobots for Biomedicine: Delivery, Surgery, Sensing, and Detoxification. *Sci. Robot.* **2017,** *2*, eaam6431.

(145) Wang, J.; Xiong, Z.; Zheng, J.; Zhan, X.; Tang, J. Light-Driven Micro/Nanomotor for Promising Biomedical Tools: Principle, Challenge, and Prospect. *Acc. Chem. Res.* **2018,** *51*, 1957-1965.

(146) Wu, T.; Nieminen, T. A.; Mohanty, S.; Miotke, J.; Meyer, R. L.; Rubinsztein-Dunlop, H.; Berns, M. W. A Photon-Driven Micromotor Can Direct Nerve Fibre Growth. *Nat. Photonics* **2012,** *6*, 62-67.

(147) Ma, X.; Jannasch, A.; Albrecht, U.-R.; Hahn, K.; Miguel-López, A.; Schäffer, E.; Sánchez, S. Enzyme-Powered Hollow Mesoporous Janus Nanomotors. *Nano Lett.* **2015,** *15*, 7043-7050.

(148) Uygun, M.; Singh, V. V.; Kaufmann, K.; Uygun, D. A.; de Oliveira, S. D. S.; Wang, J. Micromotor-Based Biomimetic Carbon Dioxide Sequestration: Towards Mobile Microscrubbers. *Angew. Chem. Int. Ed.* **2015,** *54*, 12900-12904.

(149) Zhang, L.; Xiao, Z.; Chen, X.; Chen, J.; Wang, W. Confined 1d Propulsion of Metallodielectric Janus Micromotors on Microelectrodes under Alternating Current Electric Fields. *ACS Nano* **2019,** *13*, 8842-8853.

(150) Jákli, A.; Senyuk, B.; Liao, G.; Lavrentovich, O. D. Colloidal Micromotor in Smectic a Liquid Crystal Driven by Dc Electric Field. *Soft Matter* **2008,** *4*, 2471-2474.

(151) Li, J.; Li, T.; Xu, T.; Kiristi, M.; Liu, W.; Wu, Z.; Wang, J. Magneto–Acoustic Hybrid Nanomotor. *Nano Lett.* **2015,** *15*, 4814-4821.

(152) Xu, H.; Medina-Sánchez, M.; Schmidt, O. G. Magnetic Micromotors for Multiple Motile Sperm Cells Capture, Transport, and Enzymatic Release. *Angew. Chem. Int. Ed.* **2020,** *59*, 15029-15037.

(153) Xu, L.; Mou, F.; Gong, H.; Luo, M.; Guan, J. Light-Driven Micro/Nanomotors: From Fundamentals to Applications. *Chem. Soc. Rev.* **2017,** *46*, 6905-6926.

(154) Sipova-Jungova, H.; Andren, D.; Jones, S.; Kall, M. Nanoscale Inorganic Motors Driven by Light: Principles, Realizations, and Opportunities. *Chem. Rev.* **2020,** *120*, 269-287.

(155) Dong, R.; Zhang, Q.; Gao, W.; Pei, A.; Ren, B. Highly Efficient Light-Driven TiO_2-Au Janus Micromotors. *ACS Nano* **2016,** *10*, 839-844.

(156) Xu, T.; Soto, F.; Gao, W.; Garcia-Gradilla, V.; Li, J.; Zhang, X.; Wang, J. Ultrasound-Modulated Bubble Propulsion of Chemically Powered Microengines. *J. Am. Chem. Soc.* **2014,** *136*, 8552-8555.

(157) Wang, W.; Li, S.; Mair, L.; Ahmed, S.; Huang, T. J.; Mallouk, T. E. Acoustic Propulsion of Nanorod Motors inside Living Cells. *Angew. Chem. Int. Ed.* **2014,** *53*, 3201-3204.

(158) Chen, C.; Mou, F.; Xu, L.; Wang, S.; Guan, J.; Feng, Z.; Wang, Q.; Kong, L.; Li, W.; Wang, J.; Zhang, Q. Light-Steered Isotropic Semiconductor Micromotors. *Adv. Mater.* **2017,** *29*, 1603374.

(159) Palacci, J.; Sacanna, S.; Vatchinsky, A.; Chaikin, P. M.; Pine, D. J. Photoactivated Colloidal Dockers for Cargo Transportation. *J. Am. Chem. Soc.* **2013,** *135*, 15978-15981.

(160) Wang, J.; Xiong, Z.; Zhan, X.; Dai, B.; Zheng, J.; Liu, J.; Tang, J. A Silicon Nanowire as a Spectrally Tunable Light-Driven Nanomotor. *Adv. Mater.* **2017,** *29*, 1701451.

(161) Wang, H.; Zhao, G.; Pumera, M. Beyond Platinum: Bubble-Propelled Micromotors Based on Ag and MnO_2 Catalysts. *J. Am. Chem. Soc.* **2014,** *136*, 2719-2722.

(162) Moo, J. G. S.; Presolski, S.; Pumera, M. Photochromic Spatiotemporal Control of Bubble-Propelled Micromotors by a Spiropyran Molecular Switch. *ACS Nano* **2016,** *10*, 3543-3552.

(163) Lehmuskero, A.; Ogier, R.; Gschneidtner, T.; Johansson, P.; Käll, M. Ultrafast Spinning of Gold Nanoparticles in Water Using Circularly Polarized Light. *Nano Letters* **2013,** *13*, 3129-3134.

(164) Shao, L.; Yang, Z.-J.; Andrén, D.; Johansson, P.; Käll, M. Gold Nanorod Rotary Motors Driven by Resonant Light Scattering. *ACS Nano* **2015,** *9*, 12542-12551.

(165) Yan, Z.; Scherer, N. F. Optical Vortex Induced Rotation of Silver Nanowires. *J. Phys. Chem. Lett.* **2013,** *4*, 2937-2942.

(166) Figliozzi, P.; Sule, N.; Yan, Z.; Bao, Y.; Burov, S.; Gray, S. K.; Rice, S. A.; Vaikuntanathan, S.; Scherer, N. F. Driven Optical Matter: Dynamics of Electrodynamically Coupled Nanoparticles in an Optical Ring Vortex. *Phys. Rev. E* **2017,** *95*, 022604.

(167) Liu, M.; Zentgraf, T.; Liu, Y.; Bartal, G.; Zhang, X. Light-Driven Nanoscale Plasmonic Motors. *Nat. Nanotechnol.* **2010,** *5*, 570.

(168) Bregulla, A. P.; Yang, H.; Cichos, F. Stochastic Localization of Microswimmers by Photon Nudging. *ACS Nano* **2014,** *8*, 6542-6550.

(169) Fränzl, M.; Muiños-Landin, S.; Holubec, V.; Cichos, F. Fully Steerable Symmetric Thermoplasmonic Microswimmers. *ACS Nano* **2021,** *15*, 3434-3440.

(170) Peng, X.; Chen, Z.; Kollipara, P. S.; Liu, Y.; Fang, J.; Lin, L.; Zheng, Y. Opto-Thermoelectric Microswimmers. *Light: Sci. Appl.* **2020,** *9*, 141.

(171) Schmidt, F.; Magazzù, A.; Callegari, A.; Biancofiore, L.; Cichos, F.; Volpe, G. Microscopic Engine Powered by Critical Demixing. *Phys. Rev. Lett.* **2018,** *120*, 068004.

(172) Erbas-Cakmak, S.; Leigh, D. A.; McTernan, C. T.; Nussbaumer, A. L. Artificial Molecular Machines. *Chem. Rev.* **2015,** *115*, 10081-10206.

(173) Lee, T.-C.; Alarcón-Correa, M.; Miksch, C.; Hahn, K.; Gibbs, J. G.; Fischer, P. Self-Propelling Nanomotors in the Presence of Strong Brownian Forces. *Nano Lett.* **2014,** *14*, 2407-2412.

(174) Li, J.; Liu, Y.; Lin, L.; Wang, M.; Jiang, T.; Guo, J.; Ding, H.; Kollipara, P. S.; Inoue, Y.; Fan, D.; Korgel, B. A.; Zheng, Y. Optical Nanomanipulation on Solid Substrates Via Optothermally-Gated Photon Nudging. *Nat. Commun.* **2019,** *10*, 5672.

(175) Girot, A.; Danné, N.; Würger, A.; Bickel, T.; Ren, F.; Loudet, J. C.; Pouligny, B. Motion of Optically Heated Spheres at the Water–Air Interface. *Langmuir* **2016,** *32*, 2687-2697.

(176) Eelkema, R.; Pollard, M. M.; Vicario, J.; Katsonis, N.; Ramon, B. S.; Bastiaansen, C. W. M.; Broer, D. J.; Feringa, B. L. Nanomotor Rotates Microscale Objects. *Nature* **2006,** *440*, 163-163.

(177) Uchida, E.; Azumi, R.; Norikane, Y. Light-Induced Crawling of Crystals on a Glass Surface. *Nat. Commun.* **2015,** *6*, 7310.

(178) Kausar, A.; Nagano, H.; Ogata, T.; Nonaka, T.; Kurihara, S. Photocontrolled Translational Motion of a Microscale Solid Object on Azobenzene-Doped Liquid-Crystalline Films. *Angew. Chem. Int. Ed.* **2009,** *48*, 2144-2147.

(179) Funck, T.; Nicoli, F.; Kuzyk, A.; Liedl, T. Sensing Picomolar Concentrations of Rna Using Switchable Plasmonic Chirality. *Angew. Chem. Int. Ed.* **2018,** *57*, 13495-13498.

(180) Hentschel, M.; Schäferling, M.; Duan, X.; Giessen, H.; Liu, N. Chiral Plasmonics. *Sci. Adv.* **2017,** *3*, e1602735.

(181) Kong, X. T.; Besteiro, L. V.; Wang, Z.; Govorov, A. O. Plasmonic Chirality and Circular Dichroism in Bioassembled and Nonbiological Systems: Theoretical Background and Recent Progress. *Adv. Mater.* **2018,** *0*, e1801790.

(182) Zhao, Y.; Saleh, A. A. E.; Dionne, J. A. Enantioselective Optical Trapping of Chiral Nanoparticles with Plasmonic Tweezers. *ACS Photonics* **2016,** *3*, 304-309.

(183) Liu, X.; Yuk, H.; Lin, S.; Parada, G. A.; Tang, T. C.; Tham, E.; de la Fuente-Nunez, C.; Lu, T. K.; Zhao, X. 3d Printing of Living Responsive Materials and Devices. *Adv. Mater.* **2017**.

(184) Sun, L.; Wang, C.-Y.; Krasnok, A.; Choi, J.; Shi, J.; Gomez-Diaz, J. S.; Zepeda, A.; Gwo, S.; Shih, C.-K.; Alù, A.; Li, X. Separation of Valley Excitons in a Mos2 Monolayer Using a Subwavelength Asymmetric Groove Array. *Nat. Photonics* **2019,** *13*, 180-184.

(185) Wu, Z.; Li, J.; Zhang, X.; Redwing, J. M.; Zheng, Y. Room-Temperature Active Modulation of Valley Dynamics in a Monolayer Semiconductor through Chiral Purcell Effects. *Adv. Mater.* **2019,** *31*, e1904132.

(186) Hu, G.; Hong, X.; Wang, K.; Wu, J.; Xu, H.-X.; Zhao, W.; Liu, W.; Zhang, S.; Garcia-Vidal, F.; Wang, B.; Lu, P.; Qiu, C.-W. Coherent Steering of Nonlinear Chiral Valley Photons with a Synthetic Au-WS_2 Metasurface. *Nat. Photonics* **2019,** *13*, 467-472.

(187) Neubrech, F.; Hentschel, M.; Liu, N. Reconfigurable Plasmonic Chirality: Fundamentals and Applications. *Adv. Mater.* **2020,** *32*, e1905640.

(188) Zhou, C.; Duan, X.; Liu, N. DNA-Nanotechnology-Enabled Chiral Plasmonics: From Static to Dynamic. *Acc. Chem. Res.* **2017,** *50*, 2906-2914.

(189) Li, J.; Wang, M.; Wu, Z.; Li, H.; Hu, G.; Jiang, T.; Guo, J.; Liu, Y.; Yao, K.; Chen, Z.; Fang, J.; Fan, D.; Korgel, B. A.; Alù, A.; Zheng, Y. Tunable Chiral Optics in All-Solid-Phase Reconfigurable Dielectric Nanostructures. *Nano Lett.* **2020,** *21*, 973-979.

(190) Wang, Z.; Jing, L.; Yao, K.; Yang, Y.; Zheng, B.; Soukoulis, C. M.; Chen, H.; Liu, Y. Origami-Based Reconfigurable Metamaterials for Tunable Chirality. *Adv. Mater.* **2017,** *29*, 1700412.

(191) Schäferling, M.; Dregely, D.; Hentschel, M.; Giessen, H. Tailoring Enhanced Optical Chirality: Design Principles for Chiral Plasmonic Nanostructures. *Phys. Rev. X* **2012,** *2*, 031010.

(192) Jahani, S.; Jacob, Z. All-Dielectric Metamaterials. *Nat. Nanotechnol.* **2016,** *11*, 23.

(193) Staude, I.; Schilling, J. Metamaterial-Inspired Silicon Nanophotonics. *Nat. Photonics* **2017,** *11*, 274.

(194) Kuznetsov, A. I.; Miroshnichenko, A. E.; Brongersma, M. L.; Kivshar, Y. S.; Luk'yanchuk, B. Optically Resonant Dielectric Nanostructures. *Science* **2016,** *354*.

(195) Priolo, F.; Gregorkiewicz, T.; Galli, M.; Krauss, T. F. Silicon Nanostructures for Photonics and Photovoltaics. *Nat. Nanotechnol.* **2014,** *9*, 19-32.

(196) Tribelsky, M. I.; Luk'yanchuk, B. S. Anomalous Light Scattering by Small Particles. *Phys. Rev. Lett.* **2006,** *97*, 263902.

(197) Wang, M.; Krasnok, A.; Lepeshov, S.; Hu, G.; Jiang, T.; Fang, J.; Korgel, B. A.; Alù, A.; Zheng, Y. Suppressing Material Loss for Functional Nanophotonics Using Bandgap Engineering. *Nat. Commun.* **2020**, *11*, 5055.

(198) Holsteen, A. L.; Raza, S.; Fan, P.; Kik, P. G.; Brongersma, M. L. Purcell Effect for Active Tuning of Light Scattering from Semiconductor Optical Antennas. *Science* **2017,** *358*, 1407-1410.

(199) Albella, P.; Poyli, M. A.; Schmidt, M. K.; Maier, S. A.; Moreno, F.; Sáenz, J. J.; Aizpurua, J. Low-Loss Electric and Magnetic Field-Enhanced Spectroscopy with Subwavelength Silicon Dimers. *J. Phys. Chem. C* **2013,** *117*, 13573-13584.

(200) Zywietz, U.; Schmidt, M. K.; Evlyukhin, A. B.; Reinhardt, C.; Aizpurua, J.; Chichkov, B. N. Electromagnetic Resonances of Silicon Nanoparticle Dimers in the Visible. *ACS Photonics* **2015,** *2*, 913-920.

(201) Bakker, R. M.; Permyakov, D.; Yu, Y. F.; Markovich, D.; Paniagua-Domínguez, R.; Gonzaga, L.; Samusev, A.; Kivshar, Y.; Luk'yanchuk, B.; Kuznetsov, A. I. Magnetic and Electric Hotspots with Silicon Nanodimers. *Nano Lett.* **2015,** *15*, 2137-2142.

(202) K., V. V.; J., B. J.; Concita, S.; Thierry, V. Chirality and Chiroptical Effects in Plasmonic Nanostructures: Fundamentals, Recent Progress, and Outlook. *Adv. Mater.* **2013,** *25*, 2517-2534.

(203) Born, M. The Natural Optical Activity of Liquids and Gases. *Phys. Z* **1915,** *16*, 251.

(204) Kuhn, W. Quantitative Relationships for Natural Optical Activity. *Phys. Chem. B* **1929,** *4*, 14-36.

(205) Wonjoo, S.; Zheng, W.; Shanhui, F. Temporal Coupled-Mode Theory and the Presence of Non-Orthogonal Modes in Lossless Multimode Cavities. *IEEE J. Quantum Electron.* **2004,** *40*, 1511-1518.

(206) Yin, X.; Schäferling, M.; Metzger, B.; Giessen, H. Interpreting Chiral Nanophotonic Spectra: The Plasmonic Born–Kuhn Model. *Nano Lett.* **2013,** *13*, 6238-6243.

(207) Svirko, Y. P.; Zheludev, N. I., *Polarization of Light in Nonlinear Optics*. John Wiley & Sons: New York, 2000.

(208) Hendry, E.; Mikhaylovskiy, R. V.; Barron, L. D.; Kadodwala, M.; Davis, T. J. Chiral Electromagnetic Fields Generated by Arrays of Nanoslits. *Nano Lett.* **2012,** *12*, 3640-3644.

(209) Tang, Y.; Cohen, A. E. Optical Chirality and Its Interaction with Matter. *Phys. Rev. Lett.* **2010,** *104*, 163901.

(210) Tang, Y.; Cohen, A. E. Enhanced Enantioselectivity in Excitation of Chiral Molecules by Superchiral Light. *Science* **2011,** *332*, 333-336.

(211) Singh, V.; Rai, R. K.; Arora, A.; Sinha, N.; Thakur, A. K. Therapeutic Implication of L-Phenylalanine Aggregation Mechanism and Its Modulation by D-Phenylalanine in Phenylketonuria. *Sci. Rep.* **2014,** *4*, 3875.

(212) Hendry, E.; Carpy, T.; Johnston, J.; Popland, M.; Mikhaylovskiy, R. V.; Lapthorn, A. J.; Kelly, S. M.; Barron, L. D.; Gadegaard, N.; Kadodwala, M.

Ultrasensitive Detection and Characterization of Biomolecules Using Superchiral Fields. *Nat. Nanotechnol.* **2010,** *5*, 783-787.

(213) Kim, S. J.; Choi, K.; Lee, B.; Kim, Y.; Hong, B. H. Materials for Flexible, Stretchable Electronics: Graphene and 2d Materials. *Annu. Rev. Mater. Res.* **2015,** *45*, 63-84.

(214) Lee, C.; Wei, X.; Kysar, J. W.; Hone, J. Measurement of the Elastic Properties and Intrinsic Strength of Monolayer Graphene. *Science* **2008,** *321*, 385-388.

(215) Balandin, A. A. Thermal Properties of Graphene and Nanostructured Carbon Materials. *Nat. Mater.* **2011,** *10*, 569.

(216) Das, S.; Gulotty, R.; Sumant, A. V.; Roelofs, A. All Two-Dimensional, Flexible, Transparent, and Thinnest Thin Film Transistor. *Nano Lett.* **2014,** *14*, 2861-2866.

(217) Fang, H.; Chuang, S.; Chang, T. C.; Takei, K.; Takahashi, T.; Javey, A. High-Performance Single Layered Wse2 P-Fets with Chemically Doped Contacts. *Nano Lett.* **2012,** *12*, 3788-3792.

(218) Koppens, F. H. L.; Mueller, T.; Avouris, P.; Ferrari, A. C.; Vitiello, M. S.; Polini, M. Photodetectors Based on Graphene, Other Two-Dimensional Materials and Hybrid Systems. *Nat. Nanotechnol.* **2014,** *9*, 780.

(219) Withers, F.; Del Pozo-Zamudio, O.; Mishchenko, A.; Rooney, A. P.; Gholinia, A.; Watanabe, K.; Taniguchi, T.; Haigh, S. J.; Geim, A. K.; Tartakovskii, A. I.; Novoselov, K. S. Light-Emitting Diodes by Band-Structure Engineering in Van Der Waals Heterostructures. *Nat. Mater.* **2015,** *14*, 301.

(220) Tsai, M.-L.; Su, S.-H.; Chang, J.-K.; Tsai, D.-S.; Chen, C.-H.; Wu, C.-I.; Li, L.-J.; Chen, L.-J.; He, J.-H. Monolayer Mos2 Heterojunction Solar Cells. *ACS Nano* **2014,** *8*, 8317-8322.

(221) Feng, J.; Li, W.; Qian, X.; Qi, J.; Qi, L.; Li, J. Patterning of Graphene. *Nanoscale* **2012,** *4*, 4883-4899.

(222) Ju, L.; Geng, B.; Horng, J.; Girit, C.; Martin, M.; Hao, Z.; Bechtel, H. A.; Liang, X.; Zettl, A.; Shen, Y. R.; Wang, F. Graphene Plasmonics for Tunable Terahertz Metamaterials. *Nat. Nanotechnol.* **2011,** *6*, 630.

(223) Rodrigo, D.; Limaj, O.; Janner, D.; Etezadi, D.; García de Abajo, F. J.; Pruneri, V.; Altug, H. Mid-Infrared Plasmonic Biosensing with Graphene. *Science* **2015,** *349*, 165-168.

(224) Shi, R.; Xu, H.; Chen, B.; Zhang, Z.; Peng, L.-M. Scalable Fabrication of Graphene Devices through Photolithography. *Appl. Phys. Lett.* **2013,** *102*, 113102.

(225) Katagiri, Y.; Nakamura, T.; Ishii, A.; Ohata, C.; Hasegawa, M.; Katsumoto, S.; Cusati, T.; Fortunelli, A.; Iannaccone, G.; Fiori, G.; Roche, S.;

Haruyama, J. Gate-Tunable Atomically Thin Lateral MoS_2 Schottky Junction Patterned by Electron Beam. *Nano Lett.* **2016,** *16*, 3788-3794.

(226) Lemme, M. C.; Bell, D. C.; Williams, J. R.; Stern, L. A.; Baugher, B. W. H.; Jarillo-Herrero, P.; Marcus, C. M. Etching of Graphene Devices with a Helium Ion Beam. *ACS Nano* **2009,** *3*, 2674-2676.

(227) Fox, D. S.; Zhou, Y.; Maguire, P.; O'Neill, A.; Ó'Coileáin, C.; Gatensby, R.; Glushenkov, A. M.; Tao, T.; Duesberg, G. S.; Shvets, I. V.; Abid, M.; Abid, M.; Wu, H.-C.; Chen, Y.; Coleman, J. N.; Donegan, J. F.; Zhang, H. Nanopatterning and Electrical Tuning of MoS_2 Layers with a Subnanometer Helium Ion Beam. *Nano Lett.* **2015,** *15*, 5307-5313.

(228) Booth, H. J. Recent Applications of Pulsed Lasers in Advanced Materials Processing. *Thin Solid Films* **2004,** *453-454*, 450-457.

(229) Plech, A.; Kotaidis, V.; Grésillon, S.; Dahmen, C.; von Plessen, G. Laser-Induced Heating and Melting of Gold Nanoparticles Studied by Time-Resolved X-Ray Scattering. *Phys. Rev. B* **2004,** *70*, 195423.

(230) Ashkin, A. Applications of Laser Radiation Pressure. *Science* **1980,** *210*, 1081-1088.

(231) Tsuchiya, M.; Sankaranarayanan, S. K. R. S.; Ramanathan, S. Photon-Assisted Oxidation and Oxide Thin Film Synthesis: A Review. *Prog. Mater. Sci.* **2009,** *54*, 981-1057.

(232) He, X.; DebRoy, T.; Fuerschbach, P. W. Composition Change of Stainless Steel During Microjoining with Short Laser Pulse. *J. Appl. Phys.* **2004,** *96*, 4547-4555.

(233) Mezour, M. A.; Morin, M.; Mauzeroll, J. Fabrication and Characterization of Laser Pulled Platinum Microelectrodes with Controlled Geometry. *Anal. Chem.* **2011,** *83*, 2378-2382.

(234) Collet, E.; Lemée-Cailleau, M.-H.; Buron-Le Cointe, M.; Cailleau, H.; Wulff, M.; Luty, T.; Koshihara, S.-Y.; Meyer, M.; Toupet, L.; Rabiller, P.; Techert, S. Laser-Induced Ferroelectric Structural Order in an Organic Charge-Transfer Crystal. *Science* **2003,** *300*, 612-615.

(235) Yoo, J.-H.; Kim, E.; Hwang, D. J. Femtosecond Laser Patterning, Synthesis, Defect Formation, and Structural Modification of Atomic Layered Materials. *MRS Bull.* **2016,** *41*, 1002-1008.

(236) Sahin, R.; Simsek, E.; Akturk, S. Nanoscale Patterning of Graphene through Femtosecond Laser Ablation. *Appl. Phys. Lett.* **2014,** *104*, 053118.

(237) Paradisanos, I.; Kymakis, E.; Fotakis, C.; Kioseoglou, G.; Stratakis, E. Intense Femtosecond Photoexcitation of Bulk and Monolayer MoS_2. *Appl. Phys. Lett.* **2014,** *105*, 041108.

(238) Castellanos-Gomez, A.; Barkelid, M.; Goossens, A. M.; Calado, V. E.; van der Zant, H. S. J.; Steele, G. A. Laser-Thinning of MoS_2: On Demand Generation of a Single-Layer Semiconductor. *Nano Lett.* **2012,** *12*, 3187-3192.

(239) Zayats, A. V.; Smolyaninov, I. I.; Maradudin, A. A. Nano-Optics of Surface Plasmon Polaritons. *Phys. Rep.* **2005,** *408*, 131-314.

(240) Srituravanich, W.; Fang, N.; Sun, C.; Luo, Q.; Zhang, X. Plasmonic Nanolithography. *Nano Lett.* **2004,** *4*, 1085-1088.

(241) Pan, L.; Park, Y.; Xiong, Y.; Ulin-Avila, E.; Wang, Y.; Zeng, L.; Xiong, S.; Rho, J.; Sun, C.; Bogy, D. B.; Zhang, X. Maskless Plasmonic Lithography at 22 nm Resolution. *Sci. Rep.* **2011,** *1*, 175.

(242) Sun, Z.; Yan, Z.; Yao, J.; Beitler, E.; Zhu, Y.; Tour, J. M. Growth of Graphene from Solid Carbon Sources. *Nature* **2010,** *468*, 549.

(243) Splendiani, A.; Sun, L.; Zhang, Y.; Li, T.; Kim, J.; Chim, C.-Y.; Galli, G.; Wang, F. Emerging Photoluminescence in Monolayer MoS_2. *Nano Lett.* **2010,** *10*, 1271-1275.

(244) Ferrari, A. C.; Meyer, J. C.; Scardaci, V.; Casiraghi, C.; Lazzeri, M.; Mauri, F.; Piscanec, S.; Jiang, D.; Novoselov, K. S.; Roth, S.; Geim, A. K. Raman Spectrum of Graphene and Graphene Layers. *Phys. Rev. Lett.* **2006,** *97*, 187401.

(245) Pan, Y.; Yang, M.; Li, Y.; Wang, Z.; Zhang, C.; Zhao, Y.; Yao, J.; Wu, Q.; Xu, J. Threshold Dependence of Deep- and near-Subwavelength Ripples Formation on Natural MoS_2 Induced by Femtosecond Laser. *Sci. Rep.* **2016,** *6*, 19571.

(246) Taniguchi, S.; Shibata, T.; Takeuchi, K. Protectiveness of a CVD-Al_2O_3 Film on TiAl Intermetallic Compound against High-Temperature Oxidation. *Mater. Trans. JIM* **1991,** *32*, 299-301.

(247) Cooper, R.; Upadhyaya, H. P.; Minton, T. K.; Berman, M. R.; Du, X.; George, S. M. Protection of Polymer from Atomic-Oxygen Erosion Using Al_2O_3 Atomic Layer Deposition Coatings. *Thin Solid Films* **2008,** *516*, 4036-4039.

(248) Haynes, W. M. *CRC Handbook of Chemistry and Physics* **2014**.

(249) Han, G. H.; Chae, S. J.; Kim, E. S.; Güneş, F.; Lee, I. H.; Lee, S. W.; Lee, S. Y.; Lim, S. C.; Jeong, H. K.; Jeong, M. S.; Lee, Y. H. Laser Thinning for Monolayer Graphene Formation: Heat Sink and Interference Effect. *ACS Nano* **2011,** *5*, 263-268.

(250) Liu, L.; Ryu, S.; Tomasik, M. R.; Stolyarova, E.; Jung, N.; Hybertsen, M. S.; Steigerwald, M. L.; Brus, L. E.; Flynn, G. W. Graphene Oxidation: Thickness-Dependent Etching and Strong Chemical Doping. *Nano Lett.* **2008,** *8*, 1965-1970.

(251) Huang, J. Y.; Qi, L.; Li, J. In Situ Imaging of Layer-by-Layer Sublimation of Suspended Graphene. *Nano Res.* **2010,** *3*, 43-50.

(252) Huang, J. Y.; Ding, F.; Yakobson, B. I.; Lu, P.; Qi, L.; Li, J. In Situ Observation of Graphene Sublimation and Multi-Layer Edge Reconstructions. *Proc. Natl. Acad. Sci. U. S. A.* **2009,** *106*, 10103-10108.

(253) Yan, H. J.; Xu, B.; Shi, S. Q.; Ouyang, C. Y. First-Principles Study of the Oxygen Adsorption and Dissociation on Graphene and Nitrogen Doped Graphene for Li-Air Batteries. *J. Appl. Phys.* **2012,** *112*, 104316.

(254) Bhanu, U.; Islam, M. R.; Tetard, L.; Khondaker, S. I. Photoluminescence Quenching in Gold - MoS_2 Hybrid Nanoflakes. *Sci. Rep.* **2014,** *4*, 5575.

(255) Li, J.; Zheng, Y. Optothermally Assembled Nanostructures. *Acc. Mater. Res.* **2021**.

(256) Kollipara, P. S.; Li, J.; Zheng, Y. Optical Patterning of Two-Dimensional Materials. *Research* **2020,** *2020*, 6581250.